

THE UNIVERSITY OF OKLAHOMA
GRADUATE COLLEGE

AN INTEGRATED SEISMIC, GEOLOGIC AND PETROPHYSICAL APPROACH
TO CHARACTERIZE THE RED FORK INCISED VALLEY FILL SYSTEM IN THE
ANADARKO BASIN, OKLAHOMA.

A THESIS
SUBMITTED TO THE GRADUATE FACULTY
in partial fulfillment of the requirements for the
Degree of
MASTER OF SCIENCE

By
YORYENYS DEL MORO
Norman, Oklahoma
2012

AN INTEGRATED-SEISMIC, GEOLOGIC AND PETROPHYSICAL- APPROACH
TO CHARACTERIZE THE RED FORK INCISED VALLEY FILL SYSTEM IN THE
ANADARKO BASIN, OKLAHOMA.

A THESIS APPROVED FOR THE
CONOCOPHILLIPS SCHOOL OF GEOLOGY AND GEOPHYSICS

BY

Dr. Kurt Marfurt, Chair

Dr. John D. Pigott

Mr. John Hooper

To my family, my little and loud shadow Piccola and

my dear friend Alfredo Fernandez.

ACKNOWLEDGEMENTS

I would like to thank Dr. Kurt Marfurt for all his help, guidance, encouragement, support and most important keeping the faith throughout my school years at The University of Oklahoma. Special thanks to the thesis committee members Dr. John Pigott and Mr. John Hooper for their advice, discussions, and exceptional input to this thesis work. I thank Chesapeake Energy and CGG-Veritas for providing the seismic survey and well data used in this project. I also would like to thank Dr. J. Tim Kwiatkowski for sharing his knowledge and expertise in many aspects during my school years. Thanks to Bob Davis for his support and help. To Schlumberger, Hampson-Russell, TameCat LLC, and dGB thanks for providing licenses for the software that were used in this work.

For my friends in Norman, Diana Paola Hernandez, Atish Roy, Ben Dowdell, Roderick Perez, Lennon Infante, Bagdat Toleubay, Yuqi Zhou, Melia Da Silva, Araceli Romero, and all my colleagues that made this small town my second home. To all faculty and staff, especially Dr. Roger Slatt, Donna Mullins, Nancy Leonard, Teresa Hackney and Adrienne Fox, who were like angels at all times.

To my family, who is my firm ground, thanks for always believing and helping to become true all my dreams. Lastly, many thanks for Sumit Verma and Alfredo Fernandez, who were my motivators and most important provided guidance throughout this work.

TABLE OF CONTENTS

Acknowledgements	iv
List of Figures.....	viii
Abstract.....	xv
CHAPTER I.....	1
INTRODUCTION	1
Problem Statement.....	1
Hypothesis	2
Workflow	3
CHAPTER II	5
GEOLOGICAL BACKGROUND	5
Location area	5
Depositional history.....	6
Petroleum system elements	16
CHAPTER III.....	19
ATTRIBUTE EVALUATION OF MERGED AND REPROCESSED LEGACY	
SEISMIC SURVEYS.	19
Introduction	19
Impact of reprocessing merged surveys on poststack seismic interpretation.....	19
Attribute sensitivity to reprocessing.	29
Conclusions	57
CHAPTER IV	58
PETROPHYSICAL ANALYSIS	58

Well control	58
Facies, V_{sh} and porosity calculation	60
Lithology discrimination using cross-plots	65
CHAPTER V	67
SEISMIC INVERSION	67
Introduction	67
Data conditioning	67
Simultaneous pre-stack seismic inversion.....	72
CHAPTER VI.....	86
GEOLOGICAL INTERPRETATION	86
CHAPTER VII	97
CONCLUSIONS	97
References	98
Appendix A: AVO SLOPE AND INTERCEPT	102
AVO analysis in the “mega-merged” survey and wells	107
Appendix B: Previous work	110
Appendix C: Neural network analysis.....	115
Appendix D: Generative topographic maps	119

LIST OF TABLES

Table 1. Acquisition geometry of the mega merged and Watonga surveys.	20
Table 2. Processing parameters used to merge all seismic surveys.	21
Table 3. Wave extraction parameters to generate far, middle and near offset wavelet..	73
Table 4. Training and Validation error using 7-sample convolution operator.....	116

LIST OF FIGURES

Figure 1. Location Map of Anadarko Basin and principal geologic provinces in Oklahoma	5
Figure 2. Location map of the study area.	6
Figure 3. Geological features that contributed to the formation of the Anadarko Basin .	6
Figure 4. Cross-section of the Anadarko Basin showing the asymmetrical syncline and different faults	7
Figure 5. Paleogeographic reconstruction, early Pennsylvanian (315 Ma).....	8
Figure 6. Paleogeographic reconstruction Late Pennsylvanian (300 Ma).....	8
Figure 7. Columnar section showing in a magenta box the Red Fork Formation and some of the geologic formations that appear as strong reflectors on seismic	10
Figure 8. Spectral decomposition at 36Hz of the Red Fork seismic horizon	12
Figure 9. Stratigraphic cross-section showing stages of valley fill in the Red Fork Formation	12
Figure 10. Seismic line highlighting interpreted seismic horizons.	13
Figure 11. Time structural map of the top Oswego. N.....	14
Figure 12. Time structural map of the top Pink Lime.	14
Figure 13. Time structural map of the top Red Fork.....	15
Figure 14. Time structural map of the top Novi.....	15
Figure 15. Base map of the mega merged survey and Watonga survey area.	20
Figure 16. Amplitude spectrum of the Watonga and mega merged surveys.....	22
Figure 17. Representative gathers and base map indicating their location	23

Figure 18. Horizon slice along the Oswego surface through offset-limited stacked amplitude volumes.....	24
Figure 19. North-South vertical section through the Watonga survey.	25
Figure 20. North-South vertical section through the “mega merged” survey	26
Figure 21. East-West vertical section across the Watonga survey	27
Figure 22. East-West vertical section across the “mega merged” survey	28
Figure 23. Phantom horizon slice 12 ms below the Pink Lime through the energy ratio similarity (coherence) volume computed from the 1993-1996 vintage Watonga survey.	30
Figure 24. Phantom horizon slice 12 ms below the Pink Lime through the energy ratio similarity (coherence) volume computed from the mega merged survey	31
Figure 25. Phantom horizon slice 12 ms below the Pink Lime through the Sobel filter similarity volume computed from the 1993-1996 vintage Watonga survey	33
Figure 26. Phantom horizon slice 12 ms below the Pink Lime through the Sobel filter similarity volume computed from the mega merged survey.	34
Figure 27. 2D curvature (K) of a two-dimensional line defined	35
Figure 28. Curvature response of the Red Fork Formation channels under the Pink Lime Formation	36
Figure 29. Phantom horizon slice 12 ms below the Pink Lime through the most positive principal curvature volume on the 1993-1996 vintage Watonga survey.....	38
Figure 30. Phantom horizon slice 12 ms below the Pink Lime through the most positive principal curvature volume on the mega merged survey.....	39

Figure 31. Phantom horizon slice 12 ms below the Pink Lime through the most negative principal curvature volume on the 1993-1996 vintage Watonga survey.....	40
Figure 32. Phantom horizon slice 12 ms below the Pink Lime through the most negative principal curvature volume on the mega merged survey.....	41
Figure 33. Phantom horizon slice 12 ms below the Pink Lime through the most positive principal curvature co-rendered with the Sobel filter similarity volume on the 1993-1996 vintage Watonga survey	42
Figure 34. Phantom horizon slice 12 ms below the Pink Lime through the most positive principal curvature co-rendered with the Sobel filter similarity volume on the mega merged survey.	43
Figure 35. Phantom horizon slice 12 ms below the Pink Lime through most negative principal curvature co-rendered with the Sobel filter similarity volume on the 1993-1996 vintage Watonga survey	44
Figure 36. Phantom horizon slice 12 ms below the Pink Lime through the most negative principal curvature co-rendered with the Sobel filter similarity volume on the mega merged survey	45
Figure 37. Schematic diagram showing the effect of thin bed tuning analyzed using different frequencies.....	46
Figure 38. Phantom horizon slice 12 ms below the Pink Lime displaying channel features highlighted by three spectral frequencies at 14 Hz, 34 Hz, and 54 Hz on the 1993-1996 vintage Watonga survey	47

Figure 39. Phantom horizon slice 12 ms below the Pink Lime displaying channel features highlighted by three spectral frequencies at 14 Hz, 34 Hz, and 54 Hz on the mega merged survey.....	48
Figure 40. Phantom horizon slice 12 ms below the Pink Lime through the coherent energy co-rendered with Sobel filter similarity volumes on the 1993-1996 vintage Watonga survey	50
Figure 41. Phantom horizon slice 12 ms below the Pink Lime horizon through coherent energy co-rendered with Sobel filter similarity volumes on the mega merged survey. .	51
Figure 42. Phantom horizon slice at 12 ms below the Pink Lime on the Watonga survey through the inline coherent energy and crossline coherent energy	53
Figure 43. Phantom horizon slice at 12 ms below the Pink Lime on the Watonga survey through the inline coherent energy co-rendered with crossline coherent energy and coherent energy volumes	54
Figure 44. Phantom horizon slice at 12 ms below the Pink Lime on the mega merged survey through the inline coherent energy and crossline coherent energy.....	55
Figure 45. Phantom horizon slice at 12 ms below the Pink Lime on the mega merged survey through the inline coherent energy co-rendered with crossline coherent energy and coherent energy volumes	56
Figure 46. Seismic base map showing the distribution of wells with both density and sonic logs	58
Figure 47. Quality control on the two wells that had S-wave logs.....	59
Figure 48. Workflow for S-wave log estimation from more common sonic (DT), gamma ray (GR), density (RHOB), and neutron porosity (NPHI) logs.....	60

Figure 49. Apparent limestone neutron porosity correction chart used to obtain neutron porosity values of a sandstone matrix	62
Figure 50. A representative suite of logs from well 5	63
Figure 51. Cross-section showing facies distribution along the main incised valley fill system	64
Figure 52. Cross-section showing facies distribution along the main incised valley fill system	65
Figure 53. Petrophysical parameters cross-plots using GR log as lithology discriminator	66
Figure 54. Data conditioning workflow	68
Figure 55. Amplitude spectrum of the prestack mega merged survey from 1750-2000 ms original, after Trimmed statics, and after SOF	69
Figure 56. Representative CRP gathers of the original seismic data. Removed noise from the applied SOF.	71
Figure 57. Wavelet extraction for angle gathers of 5-27 degrees of offset: Time domain wavelets and their corresponding frequency spectrum.	73
Figure 58. Wavelet extraction for angle gathers of 4-20 degrees of offset: Time domain wavelets and their corresponding frequency spectrum.	74
Figure 59. Normalized error between the inverted and the well-calculated P-wave and S-wave impedances.	76
Figure 60. Validation analysis of P- and S- impedance, density and the comparison of the original seismic and the inverted result using a wavelet from the 4°-20° seismic inversion for well 5 and well 21.	77

Figure 61. Seismic inversion correlation base map for offset range 4-20 degrees (top) and 5-27 degrees.....	78
Figure 62. Crossplot of seismic inverted impedance against the estimated impedance from logs.....	79
Figure 63. P- impedance low frequency model used in the simultaneous seismic inversion	81
Figure 64. S-impedance low frequency model used in the seismic inversion.....	82
Figure 65. P-impedance arbitrary seismic vertical line.	83
Figure 66. S-impedance arbitrary seismic vertical line	84
Figure 67. Phantom horizon slice 80ms below Oswego through the P-impedance volume	85
Figure 68. Phantom horizon slice 80ms below Oswego through the S-impedance volume.	85
Figure 69. Block diagram illustrating the evolution of the Red Fork valley system by stages. Stage I, II and III.....	87
Figure 70. Seismic vertical line illustrating the distribution of the Red Fork main incised valley fill stages	88
Figure 71. Schematic cross sections illustrating variations in channel fill in an erosionally confined area.....	90
Figure 72. Phantom horizon slice 80ms below Oswego through the P-impedance volume on the mega merged survey. Interpretation of distribution of Stage I and Stage II. Interpretation of Stage III.	92
Figure 73. Response of seismic attributes to a channel feature.....	95

Figure 74. Phantom horizon slice 66 ms below Oswego through the most-positive curvature co-rendered with the most-negative curvature volume on the mega merged survey.	96
---	----

ABSTRACT

The Red Fork Formation of the Anadarko Basin has been extensively explored and produced, and was a target for early 3D seismic acquisition programs in the 1990s. Significant resources remain, such that many of these legacy surveys have been reprocessed and merged by commercial seismic processing companies to provide more regional coverage. I show that in addition to providing a more complete image of a Red Fork incised valley system, that a reprocessed “mega-merge” survey covering the study area reduces footprint contamination and improves both vertical and lateral resolution.

Most-positive and most-negative curvature, coherence, Sobel filter similarity, and spectral decomposition within the context of seismic geomorphology delineates architectural elements within the Red Fork incised valleys not readily apparent on the seismic amplitude data. In addition to improved illumination of the five previously identified stages, the mega-merge data illuminates a previously unreported sixth stage.

AVO is not routinely applied to the well consolidated Red Fork Formation. While seismic modeling confirms that AVO will have little sensitivity to fluids, simultaneous prestack seismic impedance inversion calibrated to well log data differentiates porous from non-porous sand and shale channel fill in the Red Fork Formation. Although such predictions are encouraging, the accuracy of these estimates are poor in areas covered by low-fold, short offset legacy survey components of the mega merge. For this reason, improved accuracy of lithology prediction including estimates of density from surface seismic would require more modern higher fold, longer offset seismic data acquisition.

CHAPTER I

INTRODUCTION

Problem Statement

Acoustic Impedance, Z_p , is the product of the P-wave velocity, V_p , and density ρ of a media and has been used to estimate lithology, porosity, and in favorable conditions, the type of fluid (Schlumberger Oil Field Glossary, 2012).

Seismic data reflectivity is directly correlated to changes in acoustic impedance. Impedance “inversion” transforms the seismic reflectivity at geological boundaries back to impedance which is calibrated against well log information to extend the well measurements to estimate properties in the 3D seismic volume (Foster et al., 2010)..

Originally, seismic inversion was limited to poststack seismic data (Swisi 2009). Ostrander (1984) noted variations of amplitude with offset (AVO) on prestack data. Since the pre-stack inversion provides not only P-wave impedance, $Z_p=\rho V_p$, but also S-wave impedance, $Z_s=\rho V_s$ (or alternatively Lamé parameters, $\lambda\rho-\mu\rho$). This latter parameterization has proven to be very useful in estimating the mechanical properties of Paleozoic rocks (Foster et al., 2010).

AVO and simultaneous pre-stack impedance inversion are dependent upon the seismic acquisition and processing parameters (Young et al 2005). AVO has proven to be an effective hydrocarbon indicator technique for Miocene and Pliocene gas exploration, especially in the Gulf of Mexico (Castagna et al., 1998). Careful processing and calibration of prestack seismic data with petrophysical properties along with detailed petrophysical modeling have made AVO and seismic impedance inversion

important tools for lowering drilling risk and increasing the drilling success rate. In spite of this value, little or no research has been published on the implementation of these techniques for the well-consolidated Paleozoic rocks in the Anadarko Basin, Oklahoma.

Many workers will state that “AVO doesn’t work for such rocks”. However, Barber’s (2010) AVO analysis indicated a significant impedance contrast between producing and nonproducing sands within the Red Fork Formation in the Anadarko Basin. Foster et al. (2010) also used AVO analysis to discriminate lithologies and found class II AVO anomalies to be associated with lower porosity sands and class III AVO to be associated with higher porosity sands.

In this thesis, I show that simultaneous prestack elastic impedance inversion merged with the 3D seismic attributes, successfully discriminates lithologies in the Red Fork Formation.

Hypothesis

While the Red Fork Formation has been extensively explored and produced, there still remains a significant number of undiscovered resources. Red Fork plays in Kansas and Colorado show low thermal maturity levels and have poorer reservoir quality and overall fewer sands than corresponding plays in Oklahoma and Texas. Historical data on major discoveries, individual well completions, and thermal maturity are used extensively in assessing this play.

I hypothesize that petrophysically-calibrated AVO, prestack seismic impedance inversion and seismic attribute analysis can differentiate between porous and non-

porous sand and shale channels in the Red Fork Formation in the Anadarko Basin. Such differentiation can then be used to define a workflow that can be used in unexplored areas. I did not focus on predicting fluid content because the rocks are so well-consolidated that fluid prediction will be very difficult.

Workflow

The study area contains 1933 wells, which I classify by the logs available in the target zone (with a minimum requirement of density and sonic log between the Oswego and the Novi Limestones) and by location, only using those inside the seismic survey. After defining the wells used for this project, I model the AVO response to identify petrophysical “breakouts” and/or embedded lithology distributions of interest.

Prestack seismic data are angle-limited and stacked to serve as input to simultaneous impedance inversion to estimate Z_p and Z_s (or alternatively $\lambda\rho$ and $\mu\rho$). I estimate effective porosity using Neural network analysis, of seismic impedance and seismic attribute volumes.

Shear wave sonic logs (DTSM) were available in a few wells. In order to better calibrate elastic impedance inversion results, pseudo DTSM logs are estimated using principal component analysis and neural networks to create a relationship from the wells that had shear and compressional sonic, density, neutron porosity and resistivity logs.

3D seismic attributes such as edge-sensitive most positive and most negative curvature, coherence and Sobel filter similarity, combined with facies sensitive spectral

decomposition are used to delineate the edges of incised channels, fans, and other architectural elements of the Red Fork Formation

CHAPTER II

GEOLOGICAL BACKGROUND

Location area

The study area is located in the Anadarko Basin in west central Oklahoma. The formation of interest is the Middle Pennsylvanian age Red Fork Formation. Figure 1 shows the location of the Anadarko Basin in relation to the major geologic provinces of Oklahoma (Northcutt and Campbell, 1988). Figure 2 shows the location map of the specific study area used in this project.

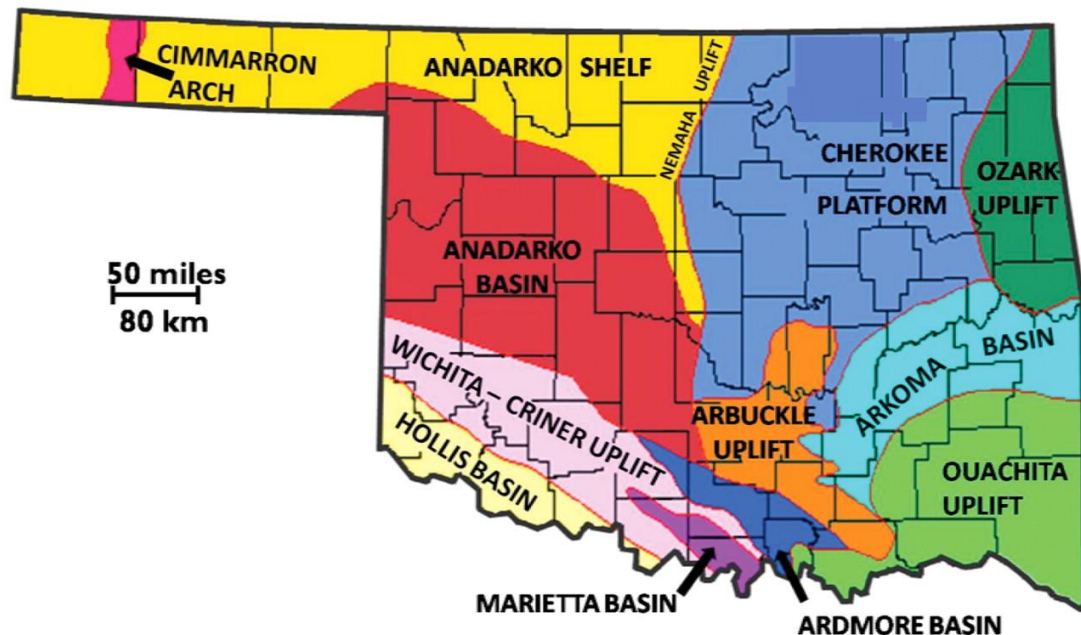


Figure 1. Location Map of Anadarko Basin and principal geologic provinces in Oklahoma (After Northcutt and Campbell, 1988).

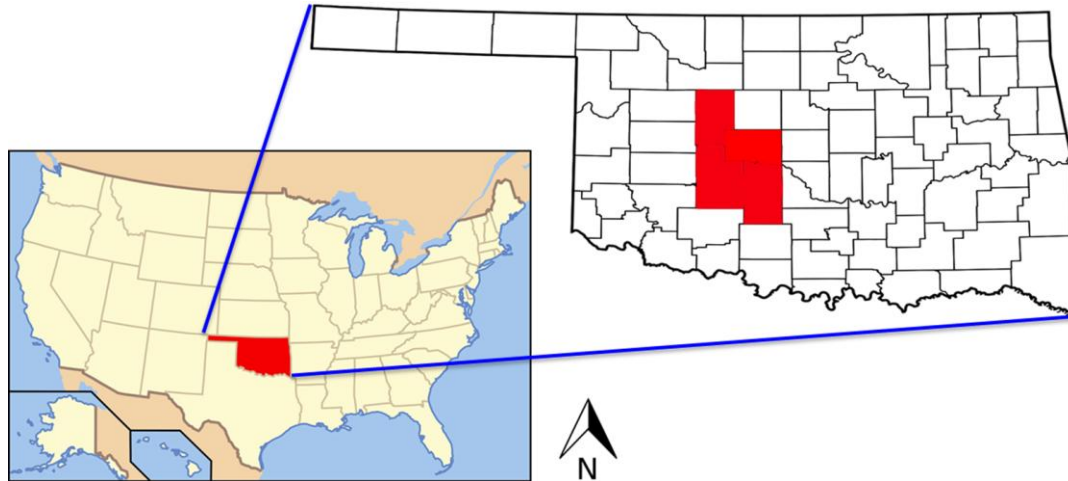


Figure 2. Location map of the study area.

Depositional history

The Anadarko Basin structurally took the form of an asymmetrical geosyncline (a regional-scale down-fold), with the deepest part near the southern edge, about 300 million years ago with the uplift of the Wichita Mountains and other surrounding positive features in earliest Pennsylvanian time (Clement 1991) (Figures 3 and 4).

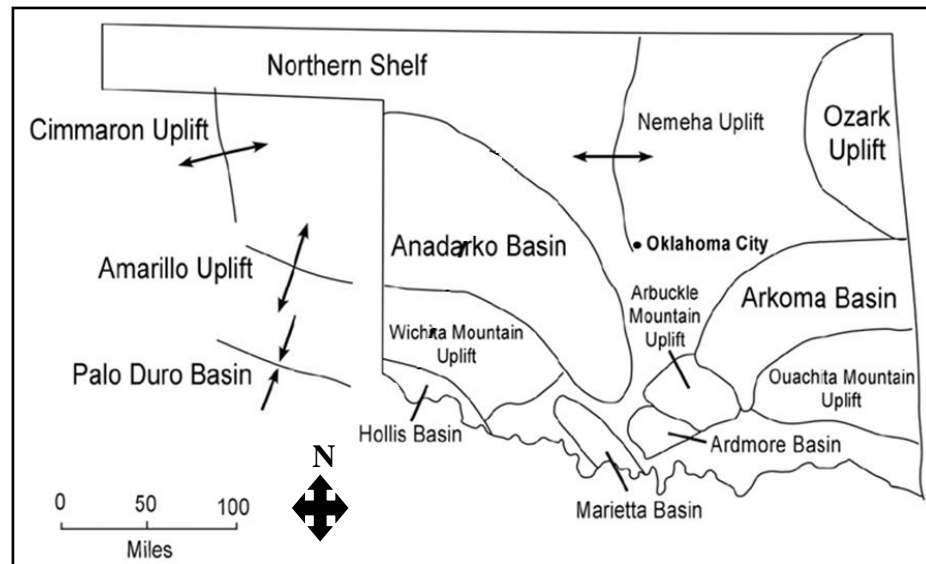


Figure 3. Geological features that contributed to the formation of the Anadarko Basin (Modified from Micklik, 1984).

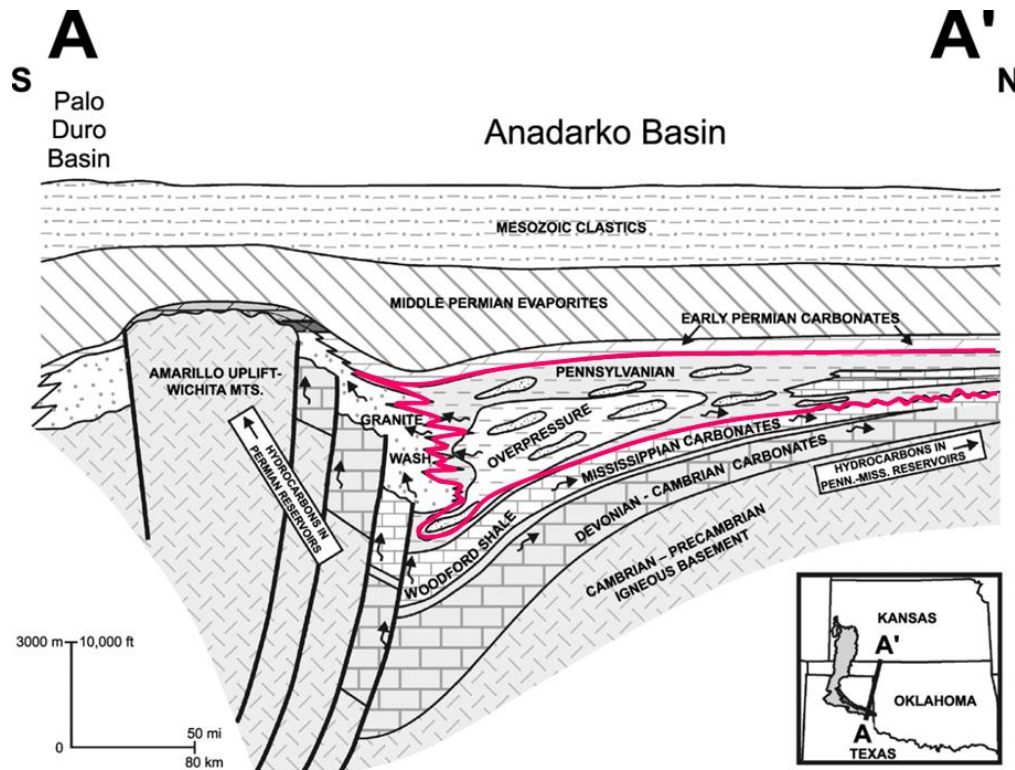


Figure 4. Cross-section of the Anadarko Basin showing the asymmetrical syncline and different faults (After Johnson, 1989).

According to Clement (1991), the subsidence of the Anadarko Basin and its rate of sediment deposition affected the generation of possible stratigraphic traps for hydrocarbon accumulation. The paleogeographic reconstruction shows the location of the Anadarko Basin during the early Pennsylvanian age (315 Ma) and Late Pennsylvanian (300 Ma) and geological events prevailing in the study area (Figures 5 and 6).

During the Pennsylvanian, Oklahoma was located south of the equator, and it was moving slowly northward (Figures 5 and 6). Variations in sea level during the Pennsylvanian caused multiple flooding in Oklahoma, which became dry land when the sea level fell. Plate tectonics, Pacific plate moving against North American plate, was

responsible for the rise and formation of the Arbuckle, Wichita and Ouachita Mountains.



Figure 5. Paleogeographic reconstruction, early Pennsylvanian (315 Ma). The red star indicates the location of the Anadarko Basin. Note that Oklahoma is flooded. (After Blakey, 2011)



Figure 6. Paleogeographic reconstruction Late Pennsylvanian (300 Ma). The red star indicates the location of the Anadarko Basin. Continental drift moved Oklahoma to the north. The Wichita and Ouachita mountains stand above sea level. (After Blakey, 2011)

My focus is on the Middle Pennsylvanian (Desmoinesian) age Red Fork Formation. The source of sediments filling the basin was from north to south, which was subsequently diverted to the west, due to the surrounding mountain uplift. The sands were deposited to the south by a river system through the Cherokee platform (Figure 1). The analysis of fine-grained sands and their distribution shows that the source of sediments is in structurally high areas near the northern part of Kansas or southern Nebraska (Clement, 1991).

The Red Fork Formation zone is characterized by three coarsening upward marine parasequences (the Lower, Middle, and Upper Red Fork Formation), divided according to different shale markers (Clement, 1991).

The Red Fork Formation sands are often well-sorted, enhancing reservoir quality. According to Tolson (1993), the Red Fork Formation also contains shale layers that were deposited by varying changes of sea level during the time of the Cherokee deposition (Desmoinesian) in the large Enid embayment during the Pennsylvanian (Figure 3). The Lower Red Fork is mainly deep-marine shale and siltstone. The Middle Red Fork is marine dominated and was deposited in a relatively deep basin on a steep, unstable delta-front slope. The Upper Red Fork was a deltaic sequence deposited in shallower water and is fluvial dominated.

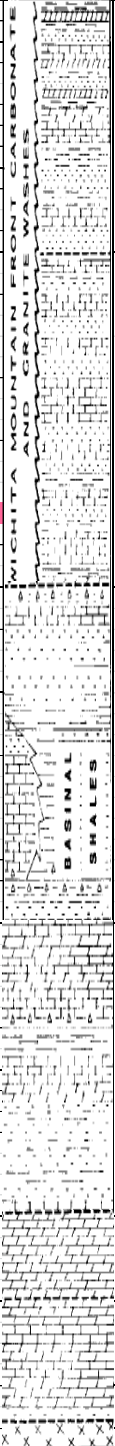
EON	SYSTEM/ SERIES	GROUP	FORMATION/ BED	ROCK TYPE	MAJOR OROGENESIS & UNCONFORMITIES
P A L E O Z O I C	PERMIAN	OCHOAN	CLOUD CHIEF FM.		ARBUCKLE OROGENY
		GUADALUPIAN	WHITEHORSE EL RENO		
		LEONARDIAN	ENID		
		WOLFCAMPAN	CHASE		
			COUNCIL GROVE		
			ADMIRE		
			WABAUNSEE		
		VIRGLIAN	SHAWNEE		
			DOUGLAS		
			ATOKAN		
	PENNSYLVANIAN	MISSOURIAN	OCHELATA		WICHITA OROGENY
			SKIATOOK		
			COTTAGE GROVE L. SS.		
			HOGSHOOTER L.		
		DESMONESIAN	LOWER LAYTON SS. (MARCHAND)		
			CHECKBOARD L.		
			CLEVELAND SS.		
			BIG LIME		
		CHEROKEE	OSWEGO LIMESTONE		
			PRUE SS.		
			VERDIGRIS L.		
			SKINNER SS.		
		MORROWAN	PINK L.		
			RED FORK FM.		
			INOLA L.		
			NOVI L.		
	MISSISSIPPIAN	CHESTERIAN	13 FINGER L.		WICHITA OROGENY
			UPPER MORROW FM.		
			LOWER MORROW FM. (PRIMROSE)		
			CUNNINGHAM SS.		
		MERAMECIAN	BRITT SS.		
			BOATWRIGHT SS.		
			CHESTER L.		
			GODDARD SH.		
		OSAGEAN	MANNING SS.		
			STE. GENEVIEVE L.		
			ST. LOUIS L.		
			CANEV SH.		
	DEVONIAN	ORISKANIAN	SPERGEN L.		ACADIAN OROGENY
			WARSAW L.		
			SYCAMORE L.		
			NAVES SH.		
		HUNTON	WOODFORD FM.		
			MISENER SS.		
			FRISCO FM.		
			BOIS D' ARC FM.		
		SILURIAN	HARAGAN FM.		
			HENRYHOUSE FM.		
			CHIMNEYHILL FM.		
			SYLVAN SH.		
	ORDOVICIAN	TRENTON	VIOLA L.		ARBUCKLE OROGENY
			BROMIDE FM.		
			TULIP CREEK FM.		
			MCLISM FM.		
		SIMPSON	OIL CREEK FM.		
			JOINS FM.		
			WEST SPRING CREEK FM.		
			KINDBLADE FM.		
		CANADIAN	COOL CREEK FM.		
			MCKENZIE HILL FM.		
	CAMBRIAN	CROIXIAN	BUTTERLY DOL.		ARBUCKLE OROGENY
			SIGNAL MTN. LS.		
			ROYER DOL.		
			FT. SILL LS.		
		TIMBERED HILLS	HONEY CREEK LS.		
			REAGAN SS.		
			GRANITE		
			GRANITE		
		PRE-CAMBRIAN	GRANITE		
			GRANITE		
			GRANITE		
			GRANITE		

Figure 7. Columnar section showing in a magenta box the Red Fork Formation (highlighted by pink) and some of the geologic formations that appear as strong reflectors on seismic. (Modified from Clement, 1991)

The Red Fork Formation overlays regionally extensive Inola Lime and Novi lime and is superposed by the Pink Lime that is characterized by containing fish scales, coffee-ground to branch-size lignitic plant debris, and brackish to shallow-marine ostracodes, linguloid brachiopods, Tasmanites algae, and gastropods (Clement, 1991).

The Upper Red Fork has an incised valley fill system which consists, according to Peyton et al. (1998), of five stages of incision fill, resulting in a stratigraphically complex internal architecture within the Anadarko Basin. Withrow et al. (1968) defined four distinct phases of sandstone deposition in the Anadarko shelf.

Phase I is the earliest event and for that reason has been eroded in many places. It includes poorly correlated channel sands and offshore bar deposits associated with sea retrogradation which allows the channel sands to be deposited and superposed upon a basal “lag” deposit. Phase II was deposited in a low energy environment indicated by thin shale layers corresponding to subaqueous offshore sand bar deposition, which happened during a period of valley widening and maturation. Phase III presents thinner sandstones and low resistivity marine shales and it was affected by rising sea level during a transgressive sequence. This phase appeared to have the last major incisement within the valley system. Phase IV contains erosions of older sediments, which indicates changes in sea level. This phase appears to be deposited in stream and river channels with effects in the sea level allowing the Pink lime carbonates to be deposited in a lagoonal swamp or by a head of a delta environment. Finally, Phase V is distinguished by non-productive sands and shales that eroded the productive Phase III (Figures 8 and 9). Phase V suffers from differential compaction on seismic data.

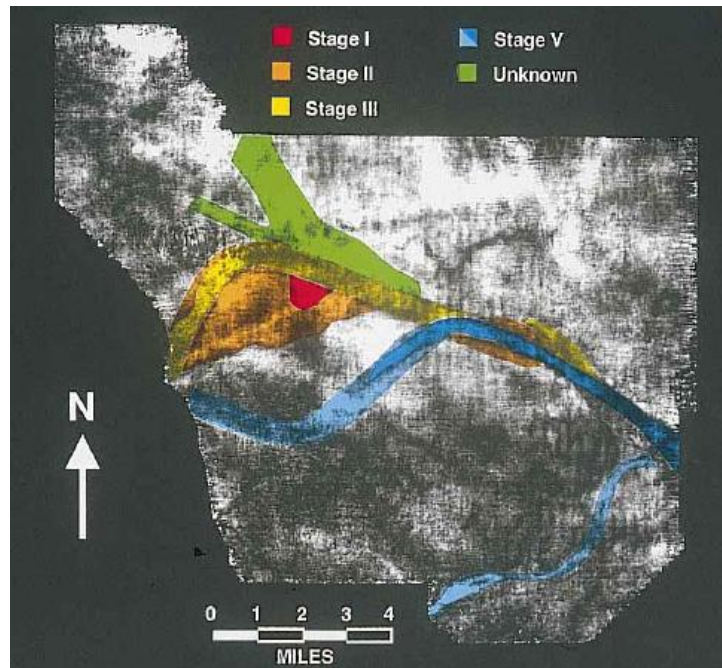


Figure 8. Spectral decomposition at 36Hz of the Red Fork seismic horizon, showing the principal incised valley phases (After Peyton et al., 1998)

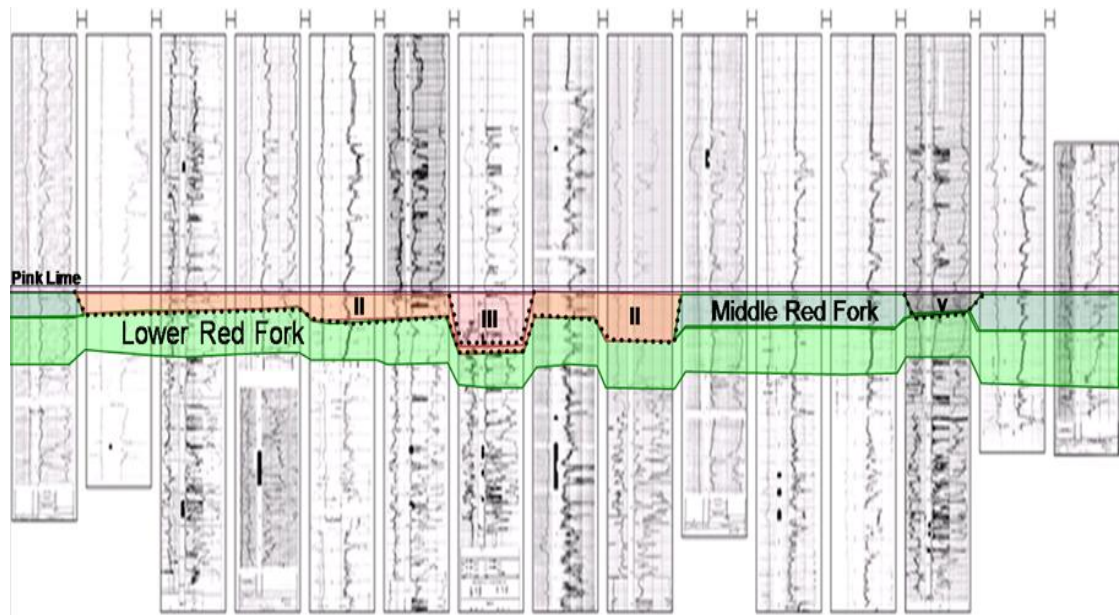


Figure 9. Stratigraphic cross-section showing stages of valley fill in the Red Fork Formation (After Suarez et al., 2008)

In this project, seven seismic horizons were interpreted to understand the geologic setting, taking into account that the target zone is between the Oswego and Novi Limes (Figure 10). The Oswego Limestone has a very strong and continuous character in the

seismic amplitude section (Figure 11). The Pink Lime horizon is patchy; its continuity is very hard to follow along the entire seismic survey. Acquisition footprint has a very strong signature on this horizon and deeper ones such as the Novi horizon (Figures 12 and 14). The Red Fork horizon was interpreted at the base of the most prominent channels in this interval. While smaller channels might have been omitted, they are seen on seismic attributes (Figure 13). The Novi limestone is a strong reflector that can be picked along the entire survey (Figure 14). The remaining horizons interpreted outside the zone of interest are not well tied, therefore they were only used as references.

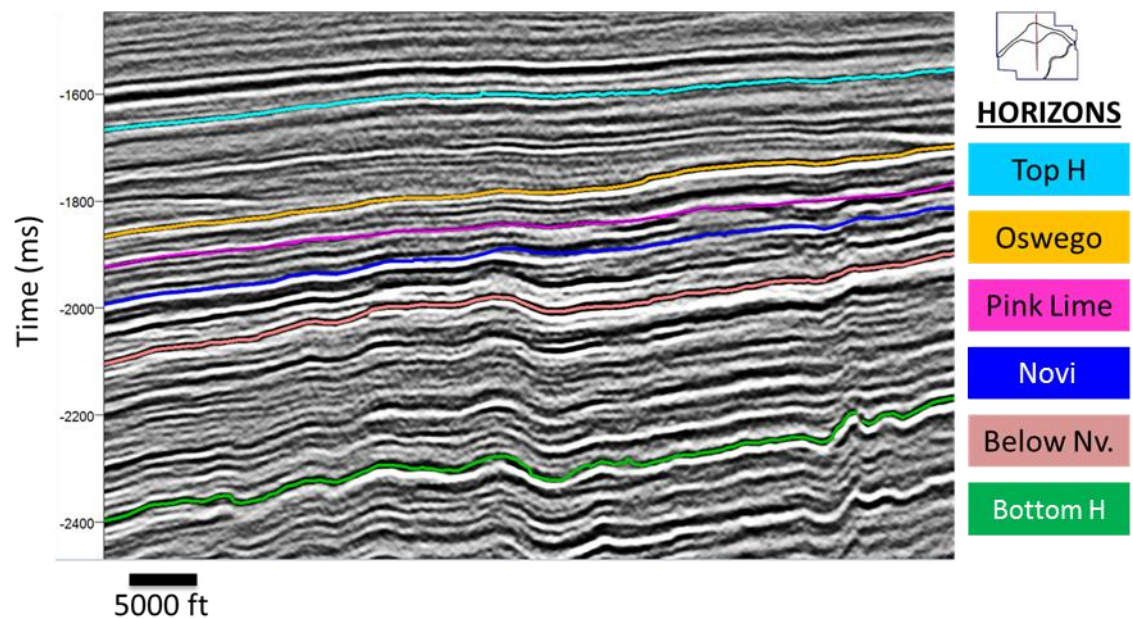


Figure 10. Seismic line highlighting interpreted seismic horizons.

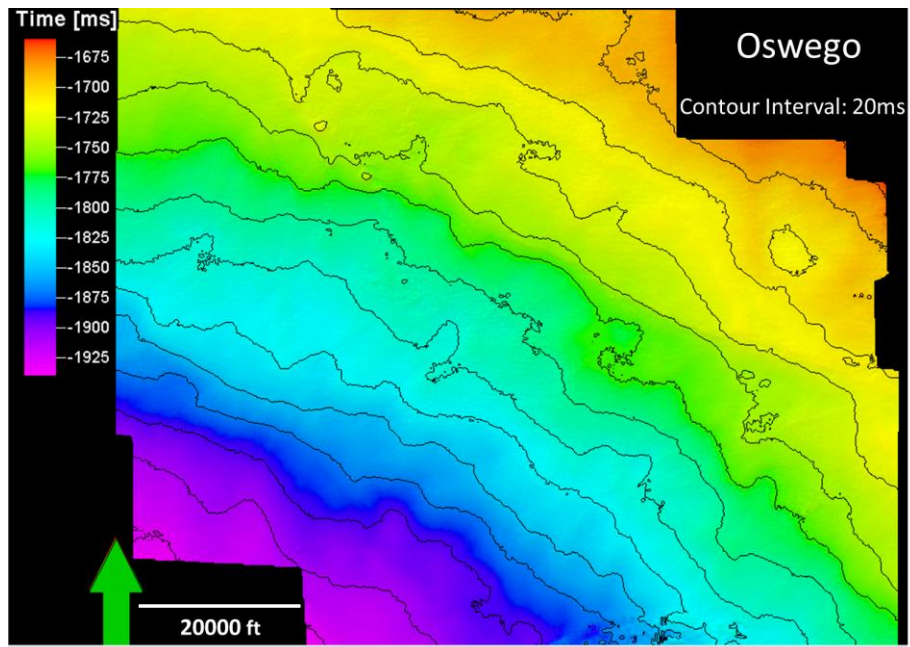


Figure 11. Time structural map of the top Oswego. Note how layers dip to the SW.

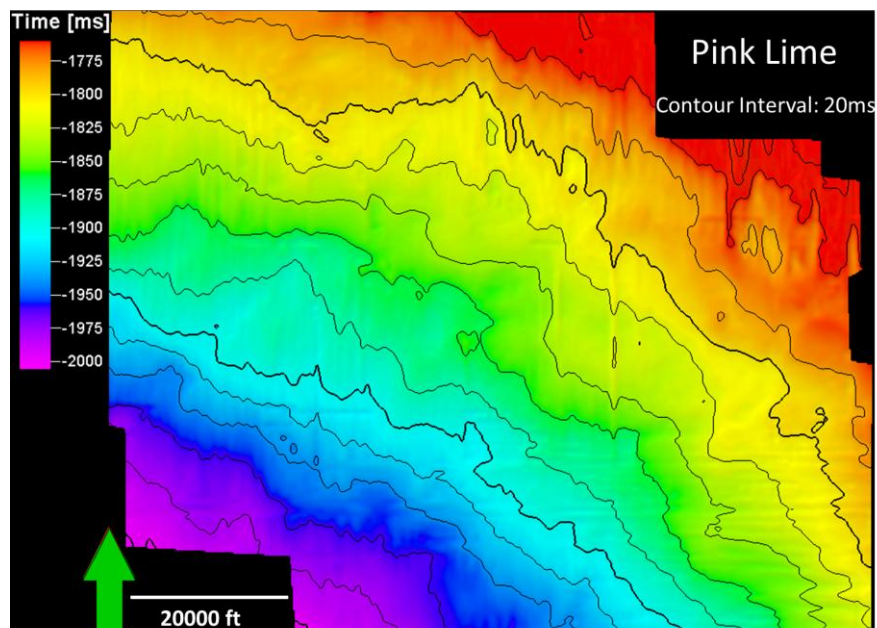


Figure 12. Time structural map of the top Pink Lime. Note how layers dip to the SW and how footprint give rise E-W and N-S trending artifacts.

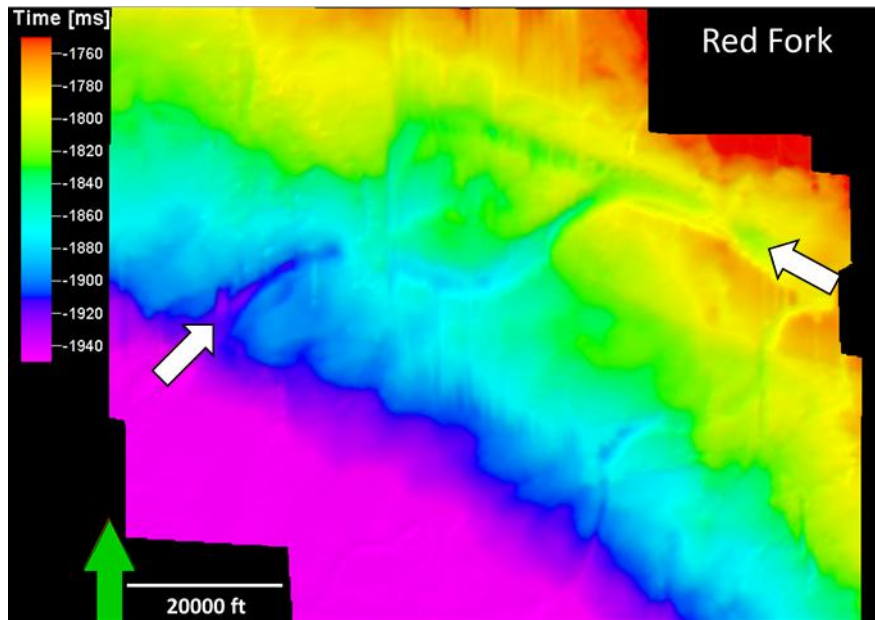


Figure 13. Time structural map of the top Red Fork. Note how layers dip to the SW. Footprint appears as E-W and N-S artifacts. This horizon was interpreted at the base of the most visible channels. Note the incised channel indicated by the white arrows.

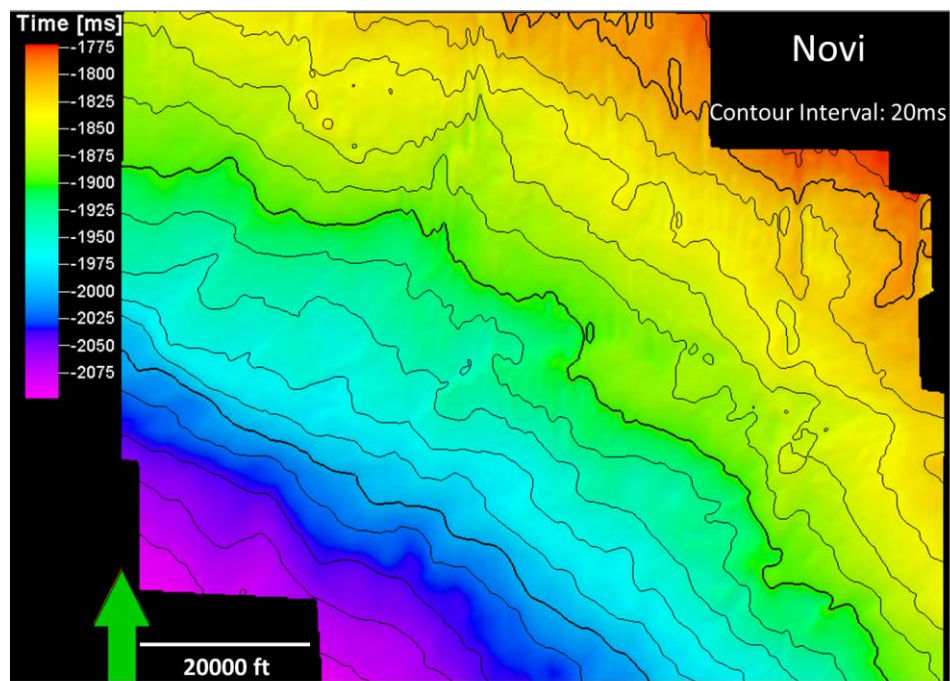


Figure 14. Time structural map of the top Novi. Note how layers dip to the SW.

Petroleum system elements

The Red Fork Formation is part of the Lower Desmoinesian Stratigraphic play which was deposited in a transgressive-regressive cycle that inundated the Anadarko Basin area with marine environments (Henry and Hester, 1995). This depositional cycle is reflected in alternating sandstone and limestone lithologies (interbedded with shale) that can be separated into stratigraphic packages of mostly sandstone or mostly limestone reservoirs (Moore, 1979; Rascoe and Adler, 1983). These packages in turn represent a mostly-sandstone play (lower part) and a mostly limestone play (upper part) (Henry and Hester 1995).

The predominance of sandstone reservoirs is the principal defining feature of the Lower Desmoinesian stratigraphic gas and oil play (Henry and Hester, 1995). It consists of all strata of the Middle Pennsylvanian Cherokee Group and those correlative strata in the lower part of the Middle Pennsylvanian Deese Group (Henry and Hester, 1995). The top of this play is the top of the Cherokee Group, which is the Prue sand or its correlatives (Henry and Hester, 1995). Depths to the top of the Prue sand range from 3,500 ft on the northern shelf to about 12,000 ft near the Wichita Mountain front (Henry and Hester 1995).

The main reservoirs consist of sandstones and limestones, including the Burgess, Bartlesville, Red Fork, Skinner, Prue, Osborne, Pooler, Hart, and Charleston sands. Rocks in this play generally thicken to the south, reaching an estimated 1,500 ft along the Wichita Mountain front (Henry and Hester, 1995).

The Red Fork sands were deposited as fluvial channels and offshore sand bars (Withrow, 1968) and are typical of other Lower Desmoinesian sands system as well (Henry and Hester, 1995). The Red Fork sandstone proportion is higher in the northeastern part of the province (Withrow, 1968) and mostly shale in the deeper-water facies (Whiting, 1984).

Porosity for this formation ranges from 12 to 15 percent (Henry and Hester, 1995). Meanwhile, in the southern and western part toward the deep Anadarko Basin, Red Fork sands consist of channelized density transport (Whiting, 1984). For this deeper interval, porosity ranges from 1 to 17 percent, with an average of about 8 percent (Henry and Hester 1995). Low permeability (about 0.1 mD) and variable reservoir quality is expected in the entire area (Withrow, 1968; Whiting, 1984; Lavine, 1984).

The source rocks can be identified as the potentially Middle and Upper Pennsylvanian black shales (Burrus and Hatch, 1989), with TOC between 0 and 18 percent from a mixture of type I and II kerogens (Henry and Hester, 1995). While the Colorado and Kansas parts are immature, most of the Oklahoma and Texas areas are thermally mature with respect to oil generation. Accumulation in these zones is probably sourced by the surrounding shales (Henry and Hester, 1995).

Basin modeling suggests potential source rocks of the Cherokee Group may have entered the thermal zone of oil generation at about 250 Ma (Schmoker, 1989). Numerous accumulations in this play prove favorable timing of trap development and hydrocarbon generation and migration (Henry and Hester, 1995).

Most of the reservoir traps types are typically stratigraphic (Henry and Hester, 1995), with little structural influence. Traps and seals could be formed by enclosing shales deposited over porous channel-filling subaerial or submarine sands, or over offshore bars (Withrow, 1968).

CHAPTER III

ATTRIBUTE EVALUATION OF MERGED AND REPROCESSED LEGACY SEISMIC SURVEYS.

Introduction

Since its introduction in the 1980s, 3D seismic surveys blanket more and more of Midcontinent of the USA and are not only used by geophysicists at large oil companies but also by geologists and engineers in small partnerships. Many of these non-geophysical seismic interpreters are unfamiliar with concepts of migration aperture and advances in seismic processing. Even for those well versed in seismic technology, they need to justify the purchase of merged, reprocessed data to their business colleagues. In this chapter, I provide a case study of such a financial investment illustrating the value through improved attribute images.

Impact of reprocessing merged surveys on poststack seismic interpretation

The Watonga survey was acquired by Amoco in three stages (1993, 1994 and 1996) with the main objective of imaging the Red Fork interval within the Anadarko Basin. The Watonga survey is of particular interest because it served as the first published application of 3D spectral decomposition analysis (Peyton et al., 1998). Chesapeake Energy bought the Amoco property and associated seismic data in the late 1990s. In 2009, Chesapeake and several other companies licensed their 3D surveys to CGG-VERITAS to form a “mega-merge” survey. Missing areas were shot to form more continuous coverage. To further facilitate the geologic interpretation of this area, these

newly acquired and legacy pre-stack volumes were then reprocessed together with newer technology including the noise attenuation and migration algorithm shown in Table 2, such that one survey helps imaging adjacent areas in previously separately processed, but adjoining surveys.

The Watonga survey forms part of the mega merged survey and covers the northeast part of it (Figure 15).

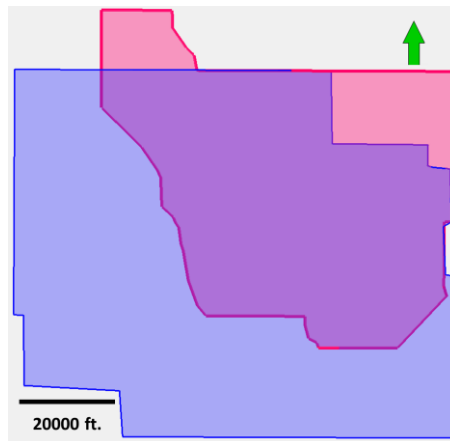


Figure 15. Base map of the mega merged survey (blue) and Watonga survey area (magenta).

Table 1 summarizes the survey geometry of the mega merged and the Watonga survey. Table 2 reviews the processing sequence applied to the mega merge survey, which included five input surveys.

	Mega merged survey	Watonga survey
Bin size	110ft*110ft	82.5ft*82.5ft
Inline direction	N-S	W-E
Crossline direction	W-E	N-S
Total number of inlines	872	886
Total number of crosslines	721	923
Seismic area	244.6 mi ²	136 mi ²

Table 1. Acquisition geometry of the mega merged and Watonga surveys.

2006 Processing sequence applied to the mega merged survey
Demultiplex/reformat (3D geometry and manual trace edits): Geometry QC: Binned 110ft by 110ft
Spreading gain recovery type: T ² (Phase Matching)
Noise burst attenuation (not on Watonga surveys)
Surface consistent deconvolution (Operator length 160 ms, prewhitening= 10%)
Surface consistent gain: Spiking Deconvolution: Operator length=160 ms. Consistency Scaling: Line/Shot/Receiver terms
Tomographic refraction statics (Datum: 1900 ft. Offset 0-10000 ft, replacement velocity=8500ft/s)
Velocity analysis, phase matching, surface consistent residual statics
Velocity analysis, noise burst attenuation, spectral whitening 4/8-115/130 Hz
Phase matching, surface consistent residual statics
FX Noise attenuation – shot domain, velocity analysis
Surface consistent gains, CDP Trim statics, 1500 ms pre-stack gain
Pre-stack time migrated Flexi-binning
Pre-stack time migrated velocity analysis
Pre-stack Kirchhoff time migration
Residual velocity analysis, NMO, mute application and tomographic long wavelength

Table 2. Processing parameters used to merge all seismic surveys.

Comparing the amplitude spectrum of the ‘mega merged’ and the Watonga surveys, I observe that the mega merged survey is better amplitude spectrally balanced than Watonga survey in the zone of interest (from the Oswego to the Novi) (Figure 16). This better distribution of the amplitude along the different frequency ranges provides better delineation of the geological features.

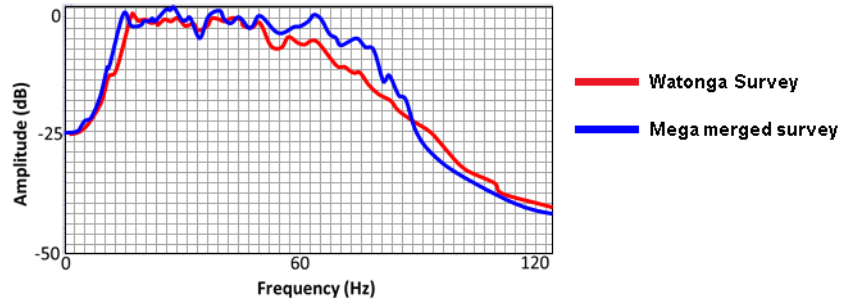


Figure 16. Amplitude spectrum of the Watonga and mega merged surveys. Note how higher frequencies are preserved on the mega merged survey.

CGG-VERITAS reprocessed the data using pre-stack time migration and one seismic survey as reference. The five legacy and infill surveys have different ranges of offsets, with more modern surveys having wider azimuths, longer offsets and greater fold. Examination of Figure 17 shows a lack of far offsets in the area of the 1993-1996 Watonga survey. In Figure 18, I plot a horizon slice along the top Oswego through different ranges of offset data volumes (0-5000 ft., 5000-8000 ft., 8000-11000 ft., 11000-14000 ft. and 14000-17100 ft.). Note that the data quality is good for all areas up to approximately 11000 ft. offset. Beyond this offset, the images in the Watonga survey contain only migration operator artifacts from the neighboring surveys acquired with larger offsets. This offset limitation will be key to our pre-stack inversion analysis in chapter V.

Processing sequences are applied soon after the data are acquired. For legacy surveys, these processing parameters may have been lost. In particular, the original sweep applied at the time of acquisition must be considered while reprocessing the old seismic data (personal communication with Dr. Tim Kwiatkowski)

Figure 19 through 23 show the enhancement of the data quality by reprocessing with newer technology. Note the reduction of migration artifacts, improvement of

channel imaging, and acquisition footprint removal in the “mega merged” survey compared to the original Watonga survey.

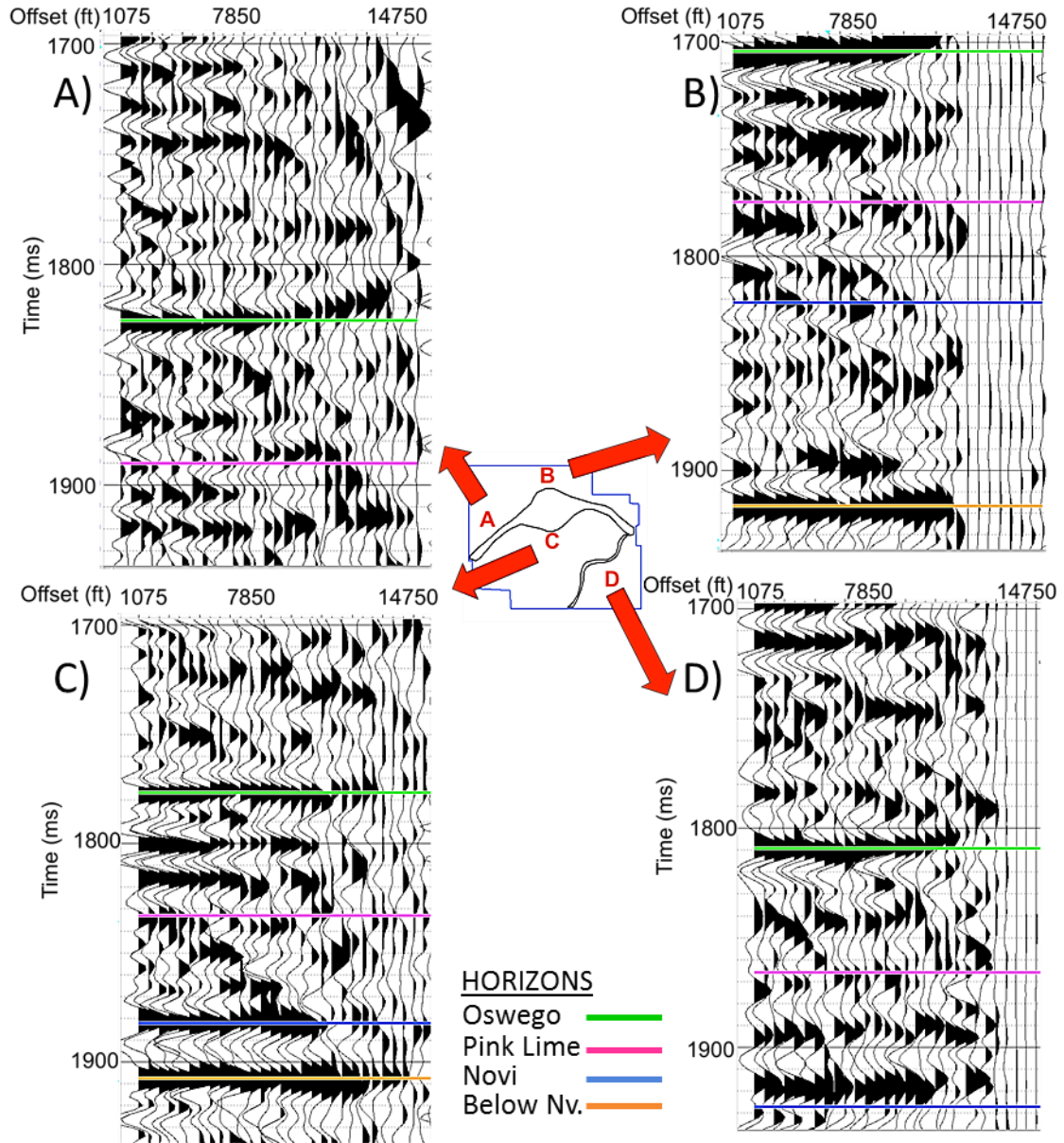


Figure 17. Representative gathers and base map indicating their location. Note that location A and D have good amplitude while B and C have low amplitude for far offsets. It appears that the maximum useable offset is about 10000 ft. for B and 12000 ft. for D. The small residual amplitudes beyond these ranges are due to migration ellipses from the longer offset surveys.

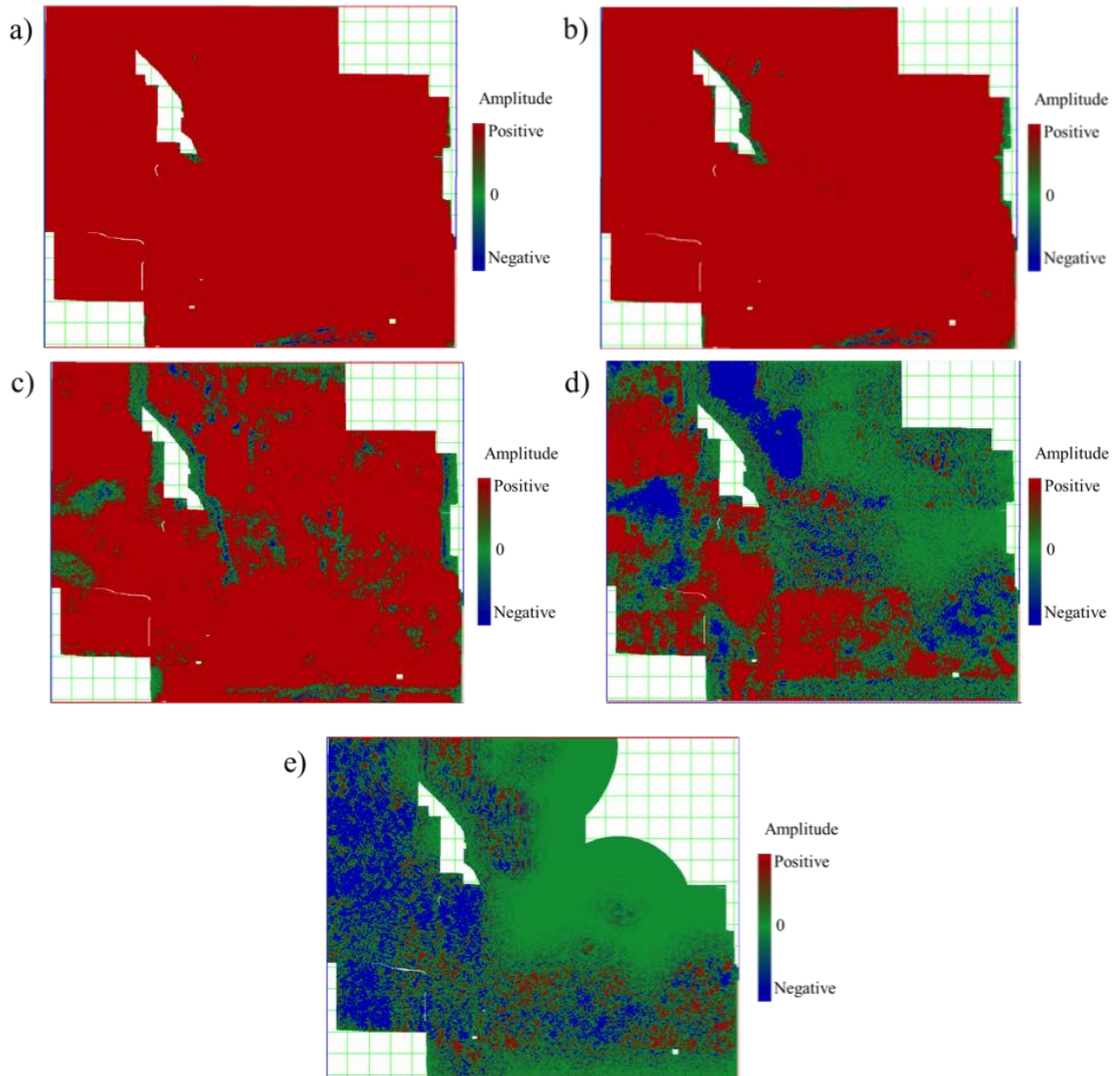


Figure 18. Horizon slice along the Oswego surface through offset-limited stacked amplitude volumes: (a) 0-5000 ft. (b) 5000-8000 ft. (c) 8000-11000 ft. (d) 11000-14000 ft. and (e) 14000-17100 ft. The Oswego Lime was interpreted as a strong peak along the seismic volume. Residual moveout (Figure 17) results in zero crossing and troughs at far offsets. Note how the amplitude approaches zero in the NE corner of the “mega-merged” survey for (e) 14000-17100 ft. offset.

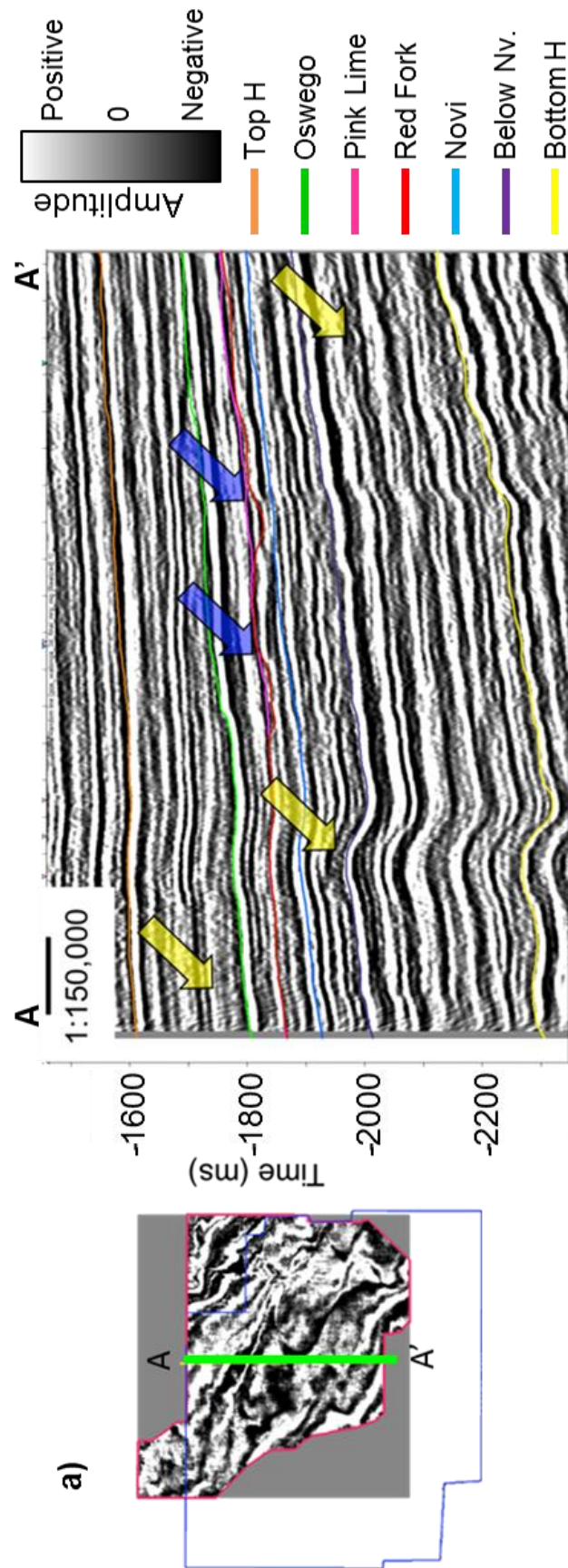


Figure 19. North-South vertical section through the Watonga survey. Blue arrows indicate channels and yellow arrows indicate migration and other noise artifacts.

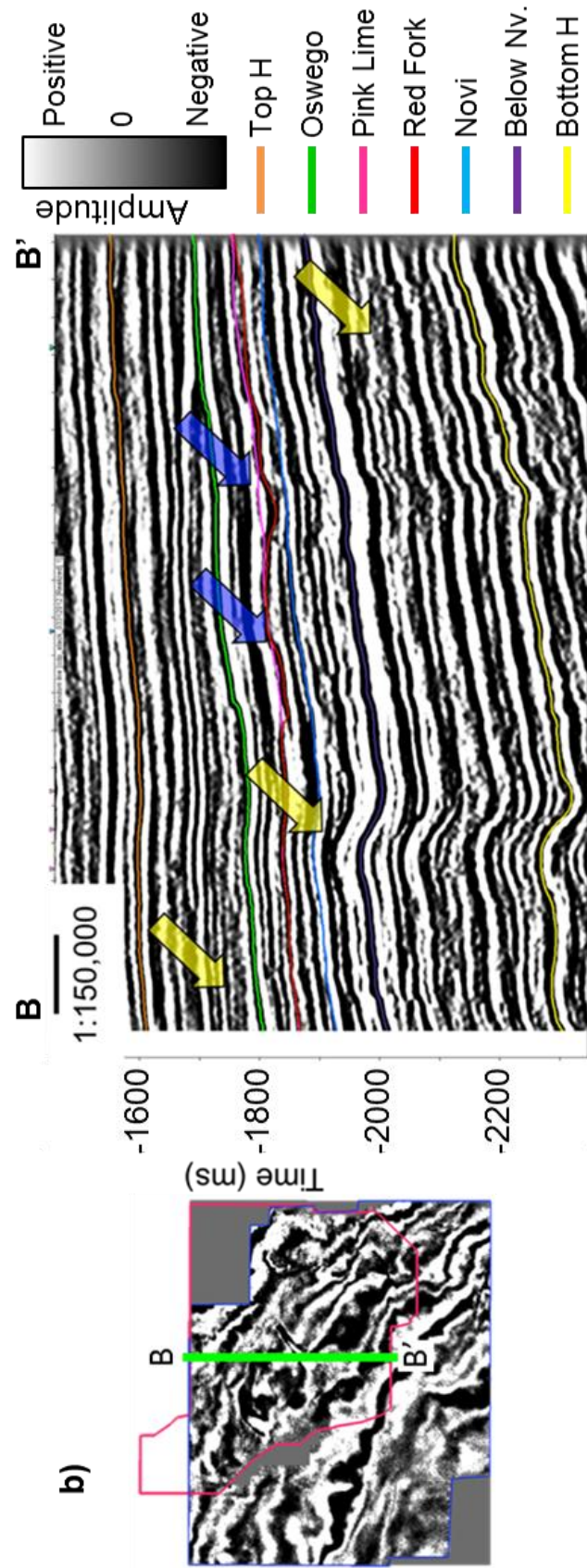


Figure 20. North-South vertical section through the "mega merged" survey. Blue arrows indicate channels and yellow arrows indicate migration and other noise artifacts.

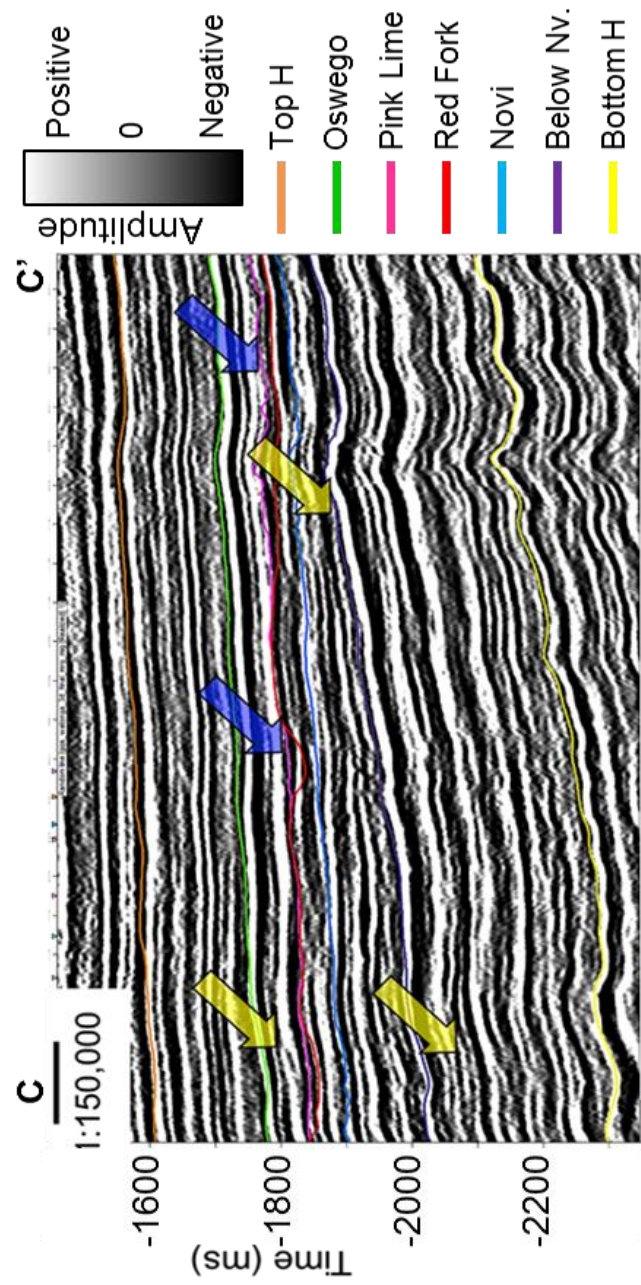


Figure 21. East-West vertical section across the Watonga survey. Blue arrows indicate channels and yellow arrows indicate migration and other noise artifacts.

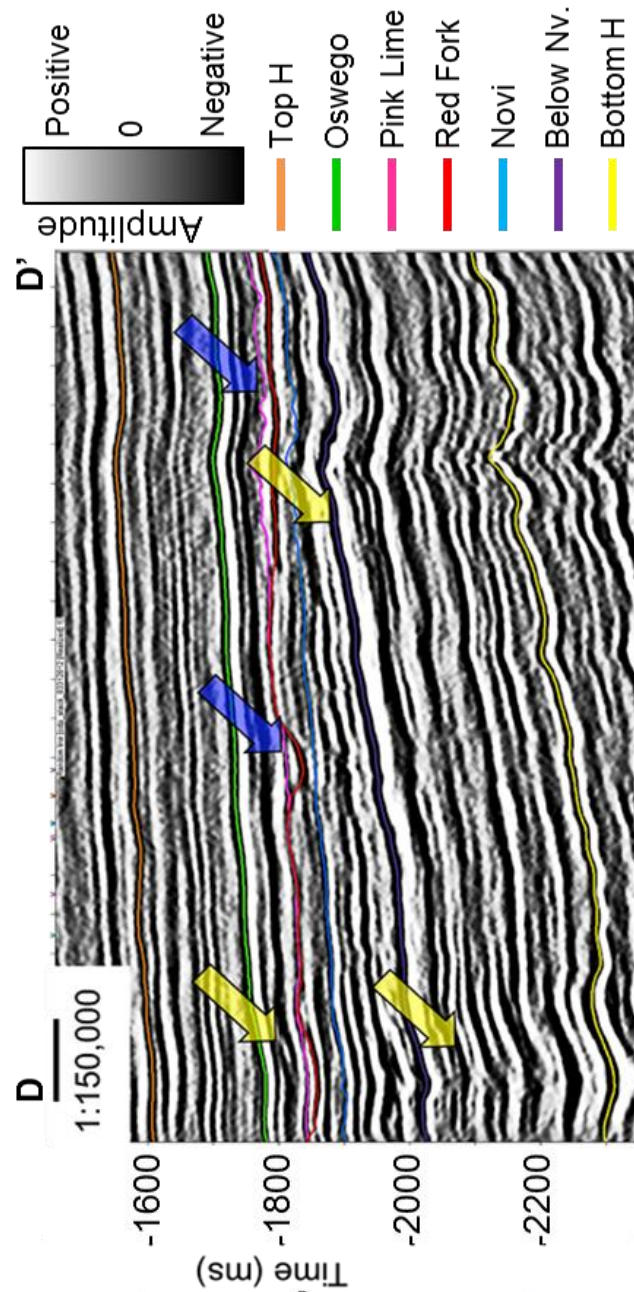


Figure 22. East-West vertical section across the "mega merged" survey. Blue arrows indicate channels and yellow arrows indicate noise artifacts.

Attribute sensitivity to reprocessing.

3D seismic attributes enable the interpreter to better visualize subtle subsurface geological structures. In the Red Fork interval, channel patterns can be delineated using edge- and facies-sensitive attributes such as coherence, Sobel filter similarity and most positive and most negative curvature. Lateral changes in amplitude and thickness can be mapped using spectral component attributes .

Acquisition footprint as well as other seismic artifacts are present in the Watonga survey, severely contaminating seismic attributes such as curvature. Reprocessing and merging adjacent legacy surveys, better delineates previously hidden geologic features.

The simplest and perhaps most important attribute is the time structure of the geologic formation of interest (Figures 11-14). Footprint is noticeable in the Pink Lime and deeper horizons.

Coherence

Coherence attributes are useful in delineating channel edges when those channels are thick enough to cause measurable changes in the form of the wavelet (Chopra and Marfurt, 2010). I use energy-ratio similarity volumes (the ratio of the energy of the Karhunen-Loeve filtered data over the energy of the original unfiltered data) to illustrate the impact of reprocessing (Figures 23 and 24).

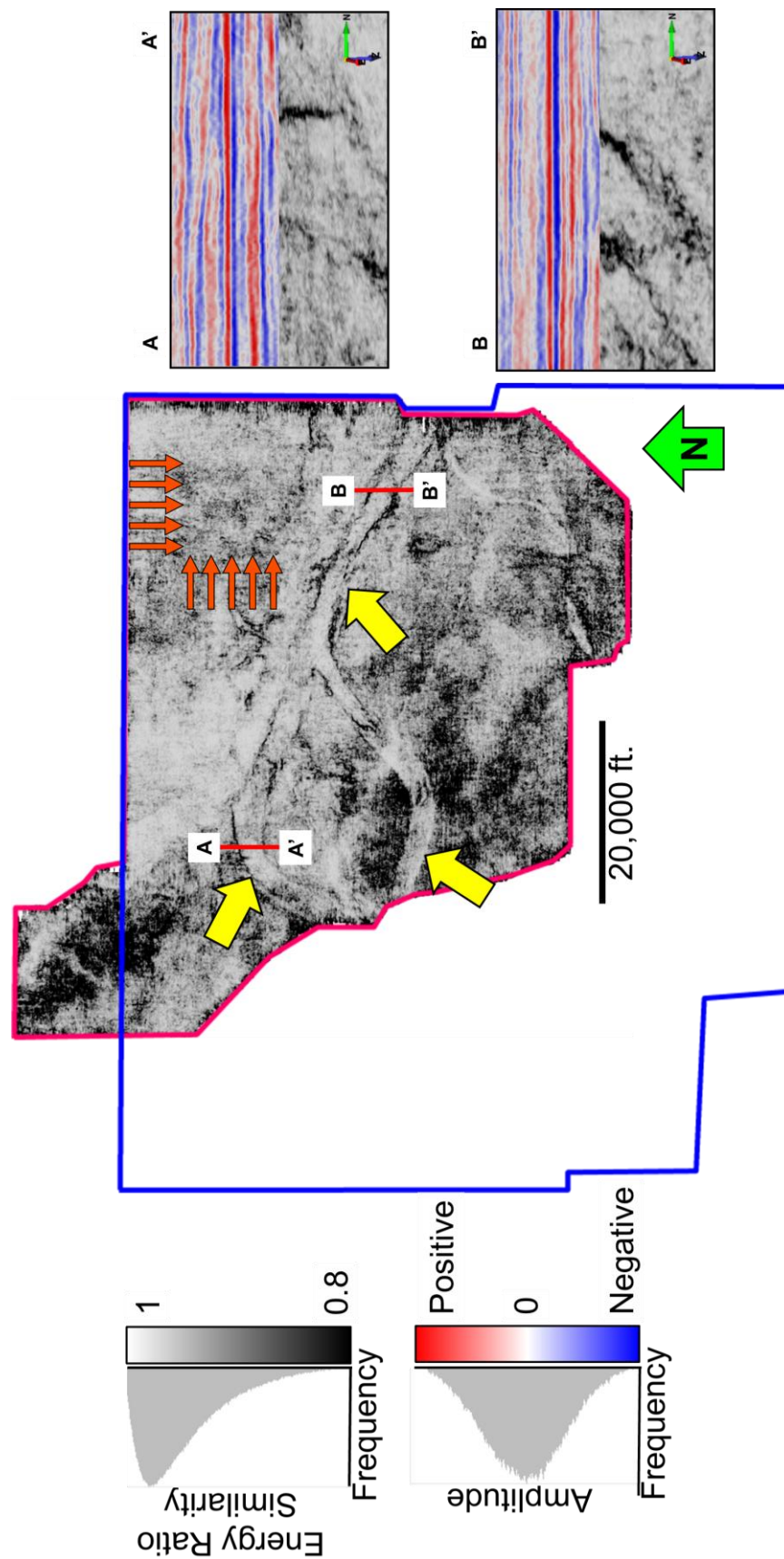


Figure 23. Phantom horizon slice 12 ms below the Pink Lime through the energy ratio similarity (coherence) volume computed from the 1993-1996 vintage Watonga survey. Yellow arrows indicate incised channels. Orange arrows indicate NS-EW footprint. A-A' and B-B' vertical sections illustrate the valley fill in the Red Fork Formation. Note that A-A' corresponds to B-B' and B-B' to C-C' on Figure 25.

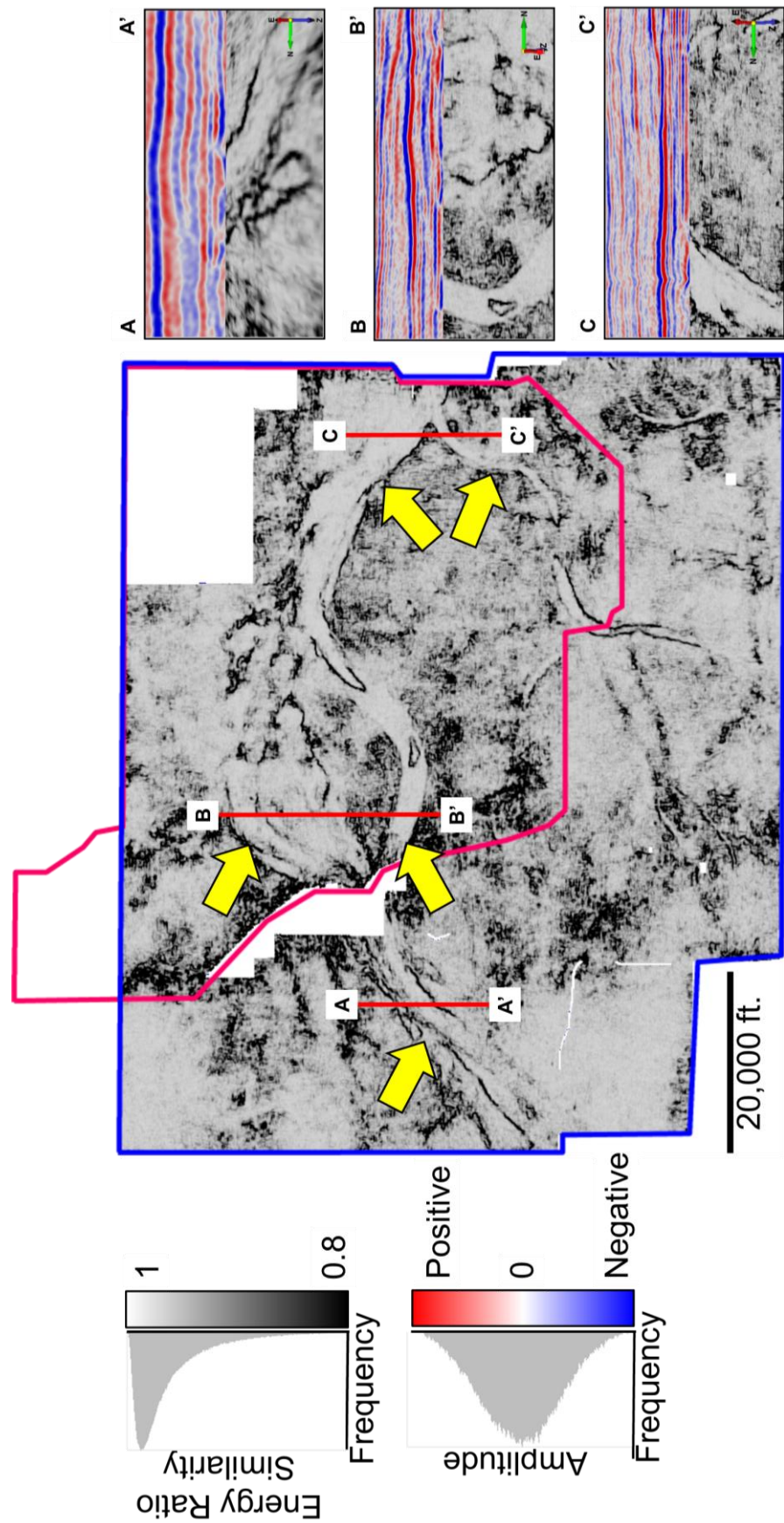


Figure 24. Phantom horizon slice 12 ms below the Pink Lime through the energy ratio similarity (coherence) volume computed from the mega merged survey. Yellow arrows indicate incised channels. Notice the reduction on the footprint. A-A', B-B', and C-C' vertical sections through the main valley fill in the Red Fork Formation.

Sobel filter similarity measures lateral changes in amplitude rather than the lateral changes in the waveform (Chopra and Marfurt, 2010). Depending on geology and data quality, Sobel filter similarity may delineate subtle edges not seen by energy ratio similarity, particularly for features below one fourth ($\frac{1}{4}$) wavelength resolution where the waveform does not change significantly. Figures 25 and 26 show a horizontal slice through the Sobel filter similarity volumes. The greater acquisition footprint is due to lack of careful amplitude balancing in the original processing.

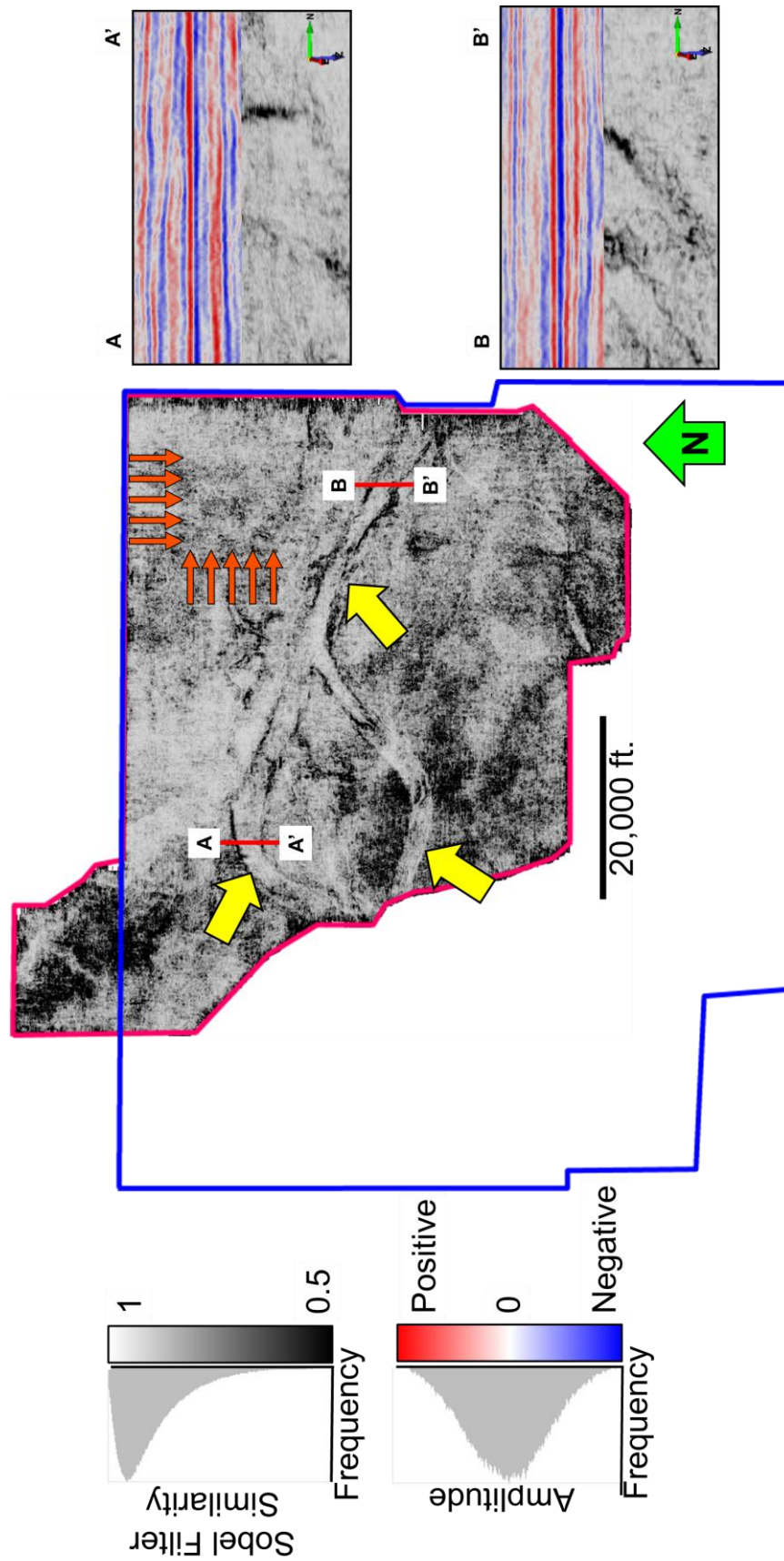


Figure 25. Phantom horizon slice 12 ms below the Pink Lime through the Sobel filter similarity volume computed from the 1993-1996 vintage Watonga survey. Yellow arrows indicate incised channels. Orange arrows indicate the strong NS-EW footprint patterns. A-A' and B-B' vertical sections illustrate the valley fill in the Red Fork Formation. Note that A-A' corresponds to B-B' and B-B' to C-C' on Figure 27.

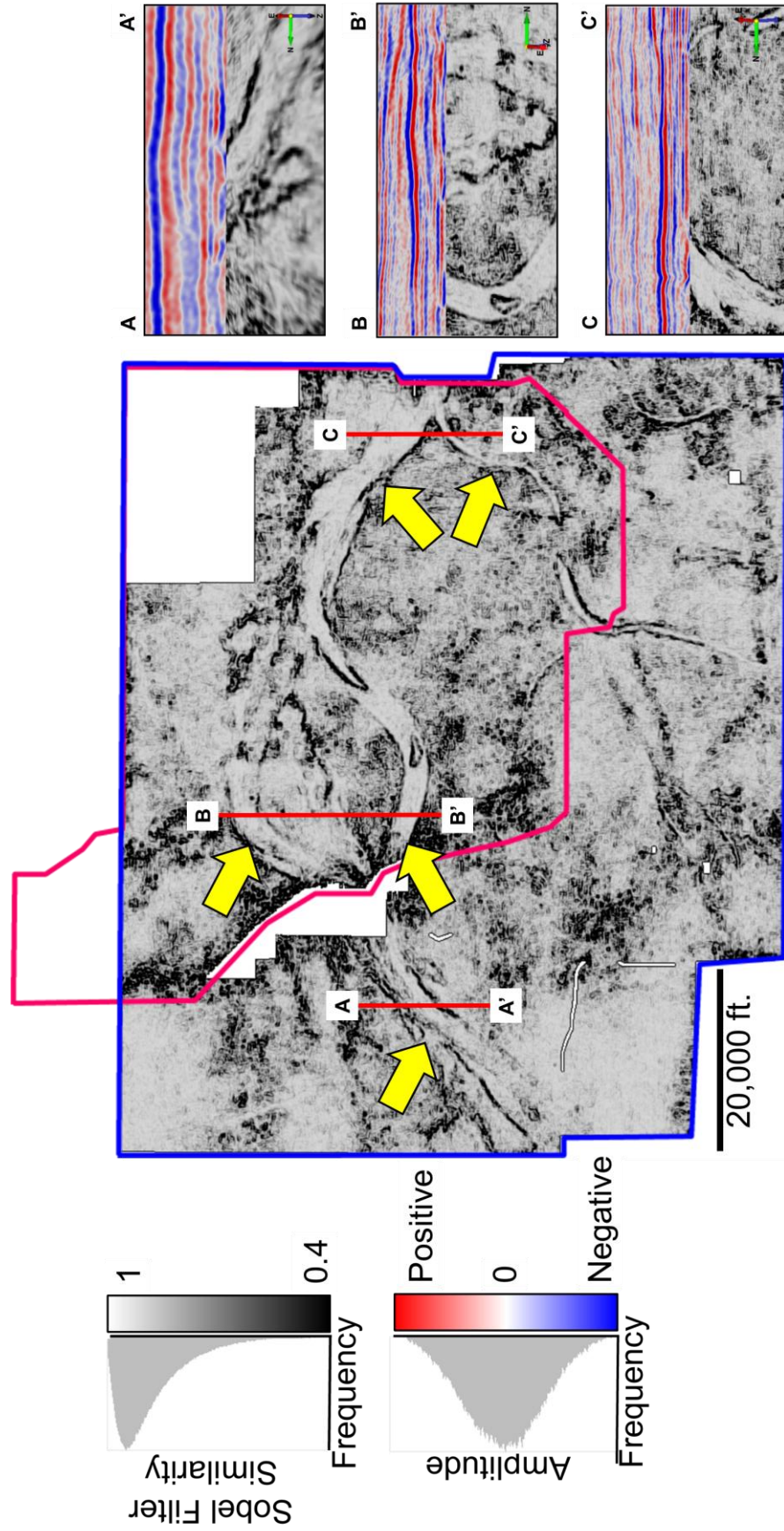


Figure 26. Phantom horizon slice 12 ms below the Pink Lime through the Sobel filter similarity volume computed from the mega merged survey. Yellow arrows indicate incised channels. Notice the reduction on the footprint. A-A', B-B', and C-C' vertical sections through the main valley fill in the Red Fork Formation.

Curvature

Curvature is defined by Chopra and Marfurt (2007) as the inverse of the radius of a circle tangent to a two-dimensional curve in a particular point (Figure 27). Structural curvature attributes measure bending and folding as well as sedimentological processes such as levees and differential compaction of incised valleys.

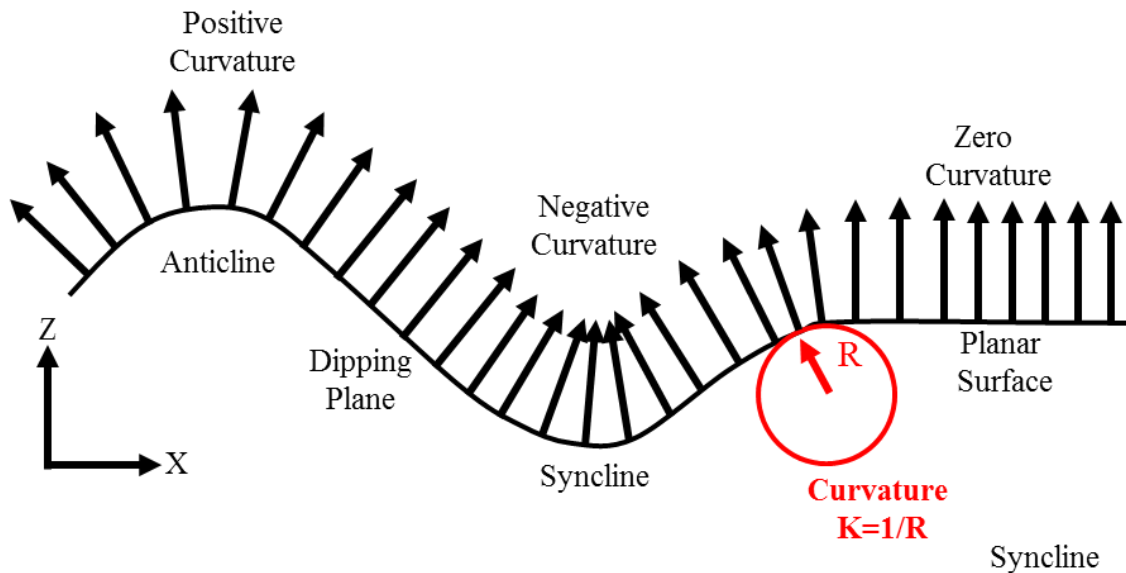


Figure 27. 2D curvature (K) of a two-dimensional line defined. Anticlinal features have positive curvature, synclinal features have negative curvature and planar features (horizontal or dipping) have zero curvature (After Roberts, 2001).

When extracting structural curvature attributes through the Red Fork Formation, two main curvature responses can be interpreted over the channels features. For narrow channels, I observe high most-positive curvature on the edges and high most-negative curvature values along the channel axis or thalweg (Figure 28a). For wide channels, I observe high most-positive curvature on the edges and high most-negative curvature values on the channel base edges and zero curvature on the bottom channel plane (Figure 28b).

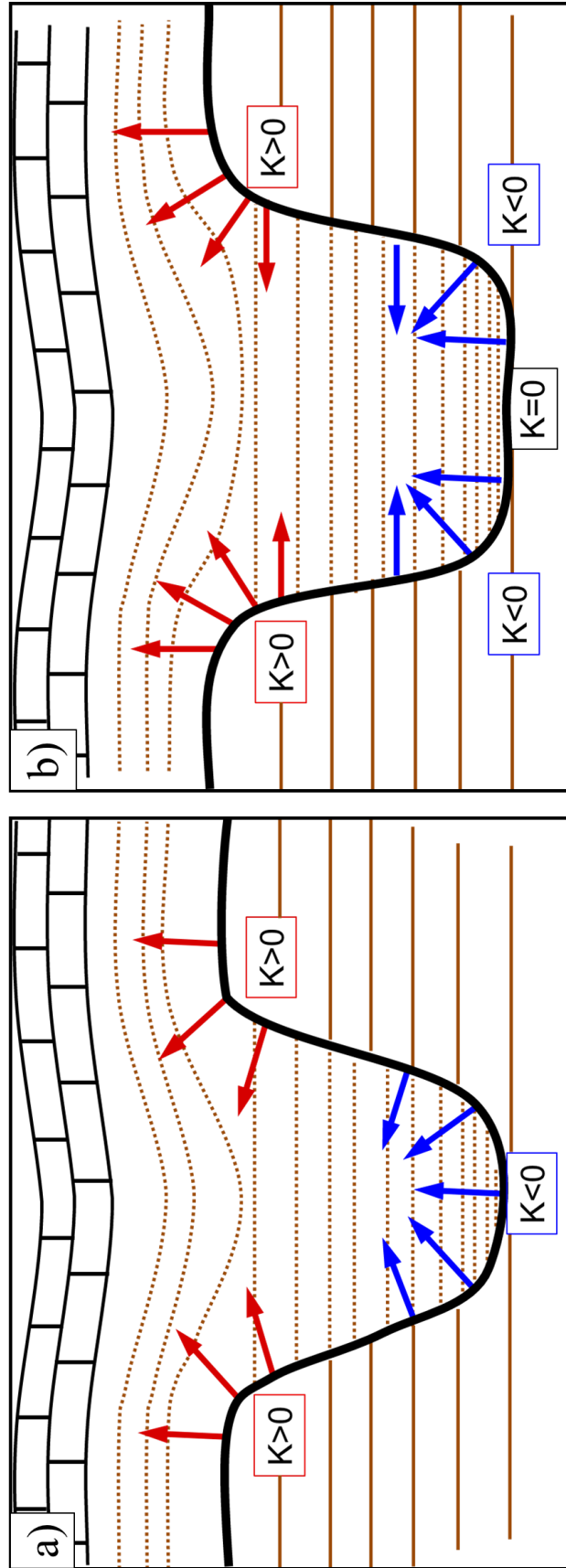


Figure 28. Curvature response of the Red Fork Formation channels under the Pink Lime Formation. a) Narrow channels are expected to have high most-positive curvature on the edges and high most-negative curvature values on the channel's thalweg. b) Wide channels are expected to have high most-positive curvature on the edges and high most-negative curvature values on the channel base edges and zero curvature on the thalweg plane. Both may give rise to differential compaction anomalies in overlying sediments.

Figures 29-32 show a representative phantom horizon slice through the most positive curvature and most negative curvature. Figures 33-36 show the most positive curvature and most negative curvature co-rendered with Sobel filter similarity to enhance the channels edges. Note how the curvature attributes over the 1993-1996 vintage Watonga survey are less detailed than over the newer mega-merge survey. The channel associated with the Red Fork Formation are better delineated by the attributes extracted over the mega-merged survey.

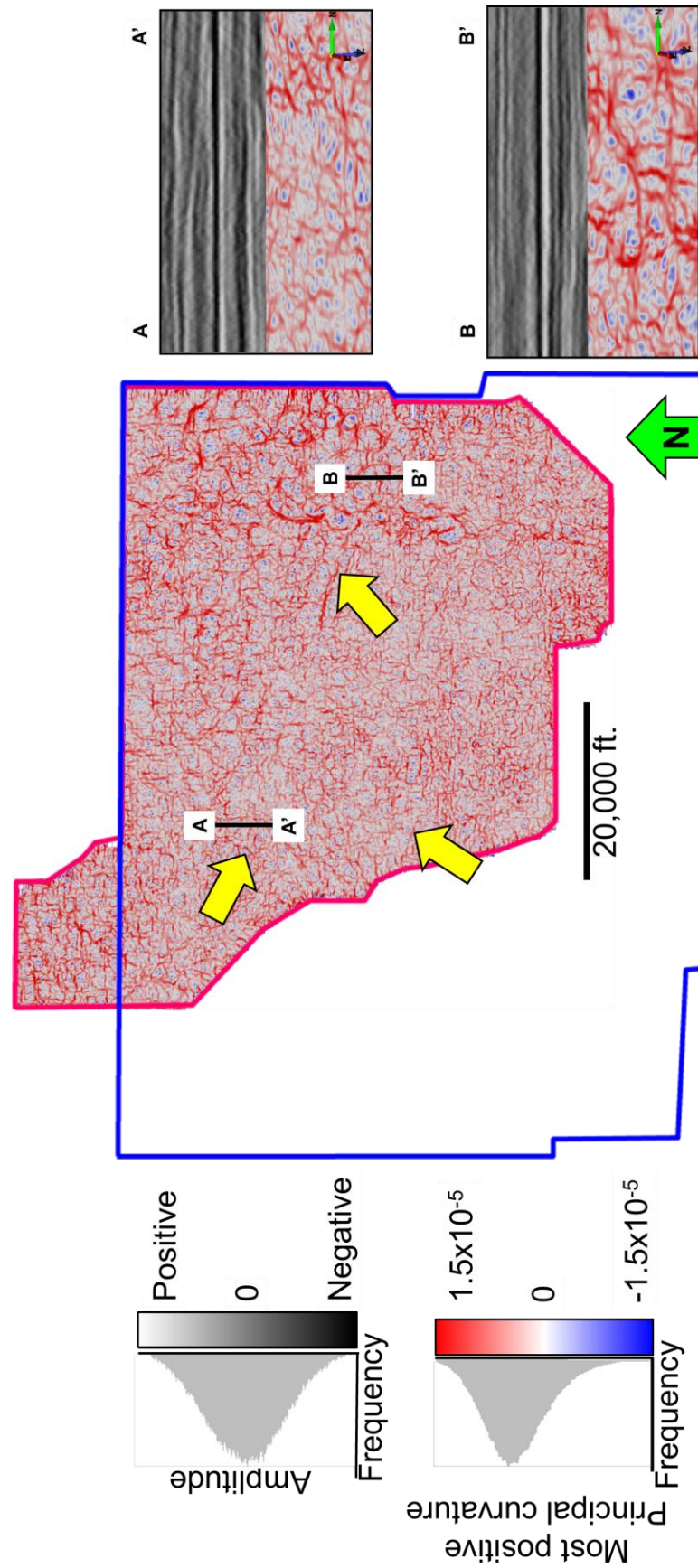


Figure 29. Phantom horizon slice 12 ms below the Pink Lime through the most positive principal curvature volume on the 1993-1996 vintage Watonga survey. Yellow arrows indicate incised channels. A-A' and B-B' vertical sections through the main valley fill in the Red Fork Formation. Note that A-A' corresponds to B-B' and B-B' to C-C' on Figure 32.

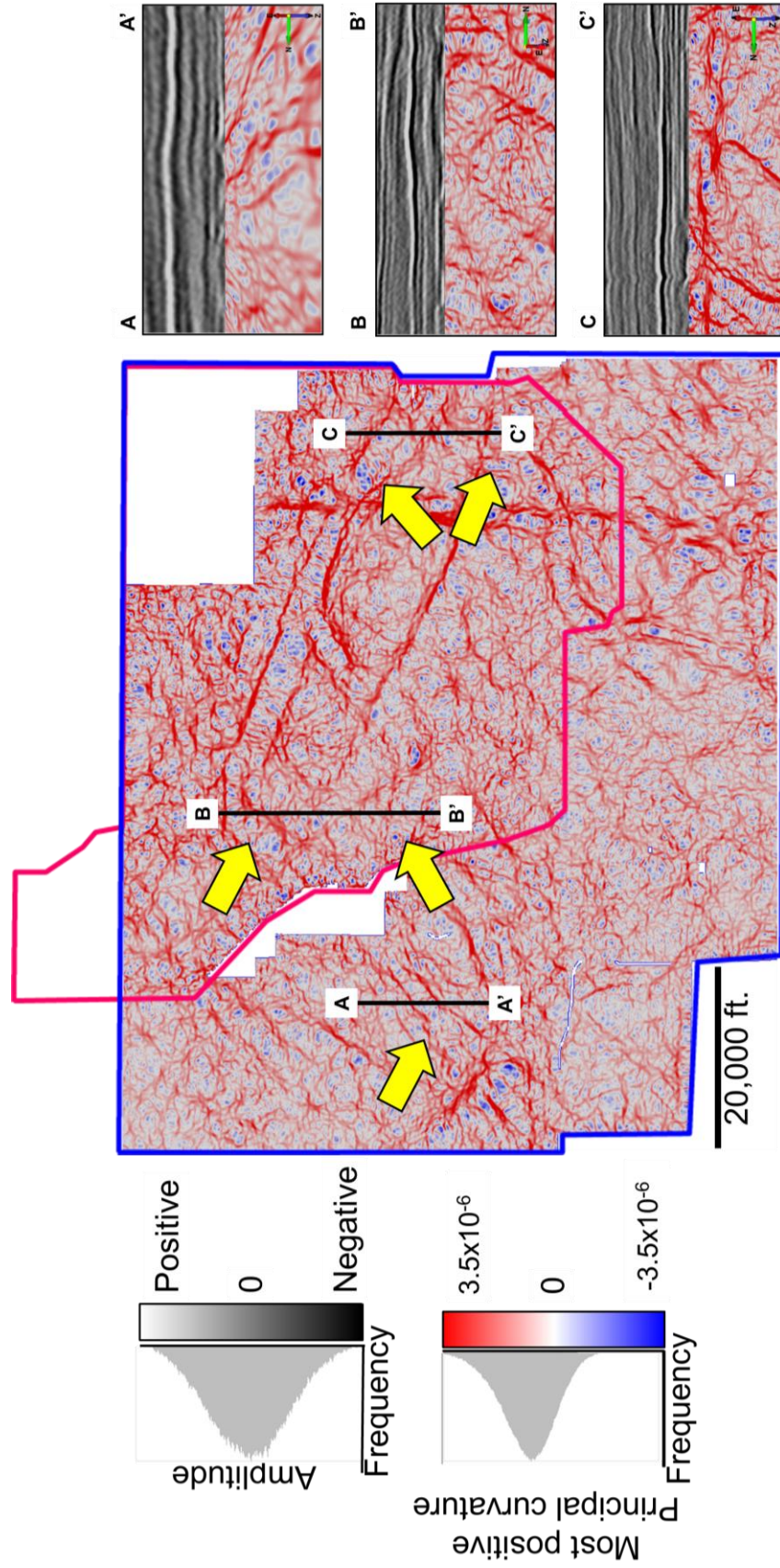


Figure 30. Phantom horizon slice 12 ms below the Pink Line through the most positive principal curvature volume on the mega merged survey. Yellow arrows indicate incised channels. A-A', B-B' and C-C' vertical sections through the main valley fill in the Red Fork Formation.

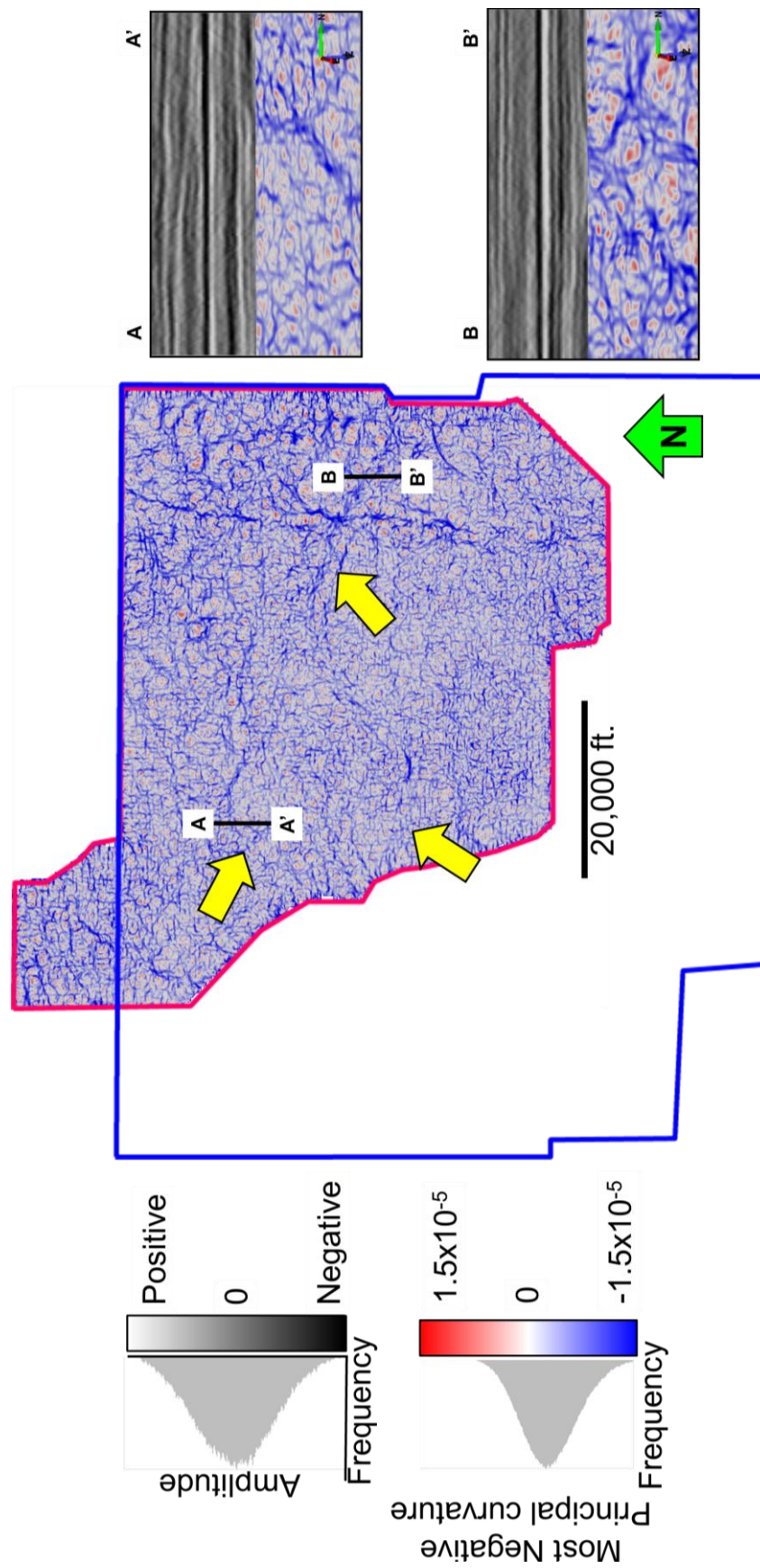


Figure 31. Phantom horizon slice 12 ms below the Pink Lime through the most negative principal curvature volume on the 1993-1996 vintage Watonga survey. Yellow arrows indicate incised channels. Notice the poor delineation of the channel features. A-A' and B-B' vertical sections through the main valley fill in the Red Fork Formation. Note that A-A' corresponds to B-B' to C-C' on Figure 33.

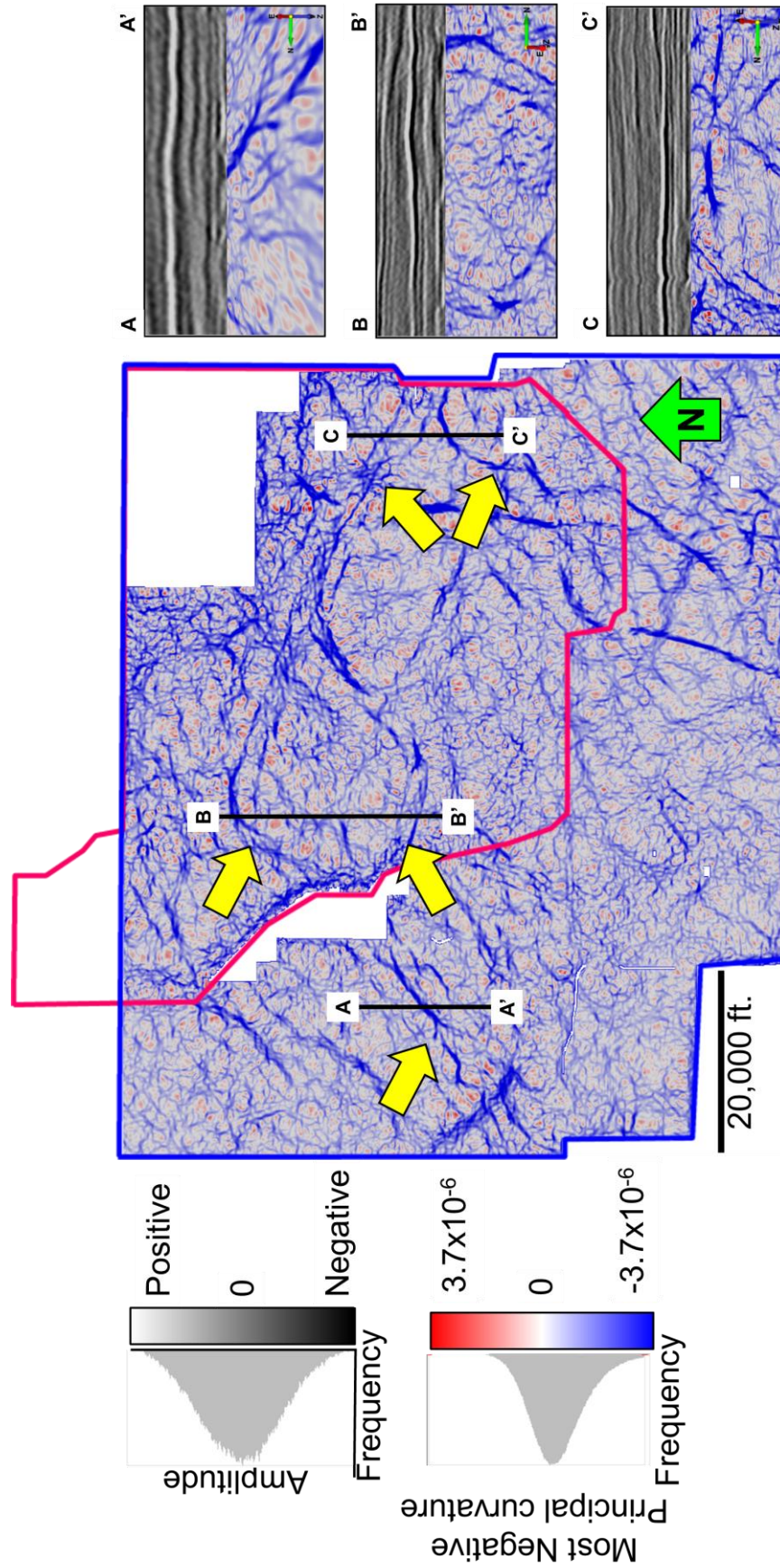


Figure 32. Phantom horizon slice 12 ms below the Pink Lime through the most negative principal curvature volume on the mega merged survey. Yellow arrows indicate incised channels. Negative curvature values correlate to the channel thalweg. A-A', B-B' and C-C' vertical sections through the main valley fill in the Red Fork Formation.

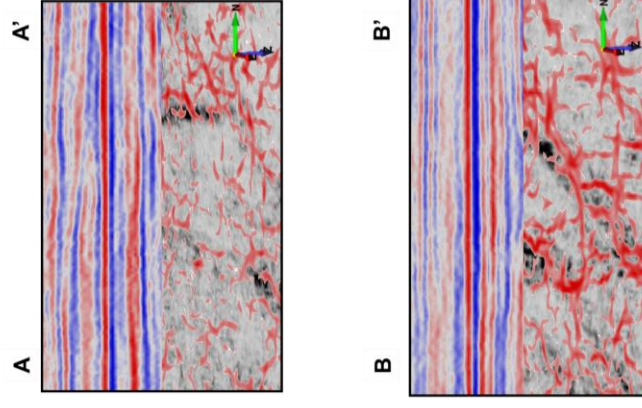
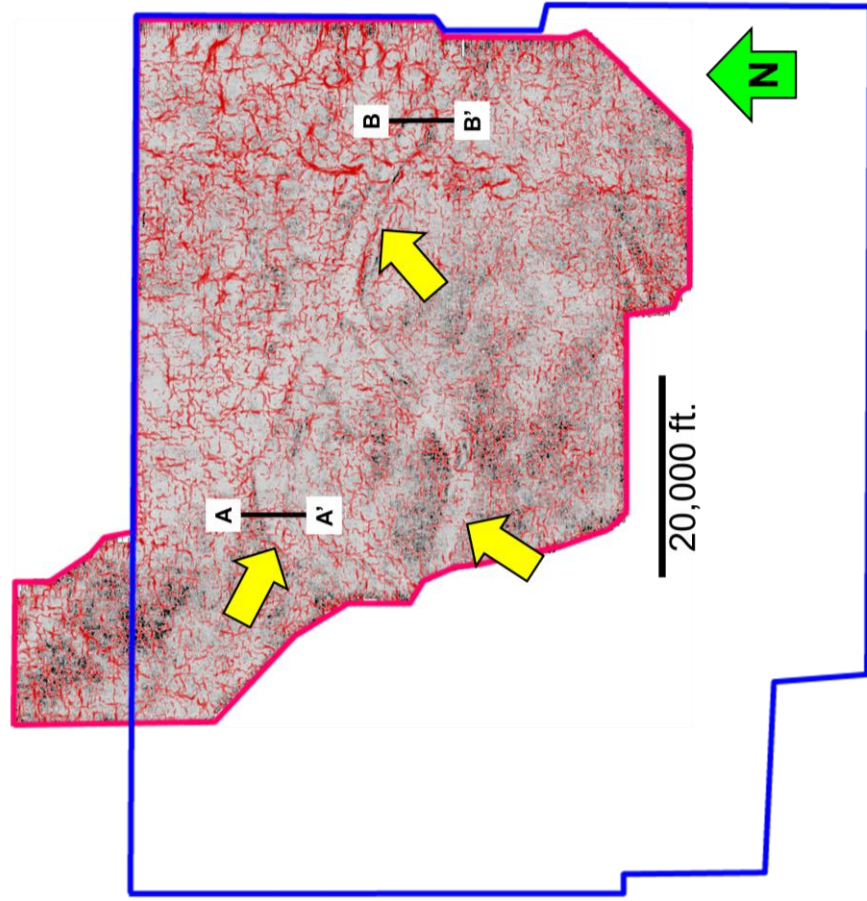
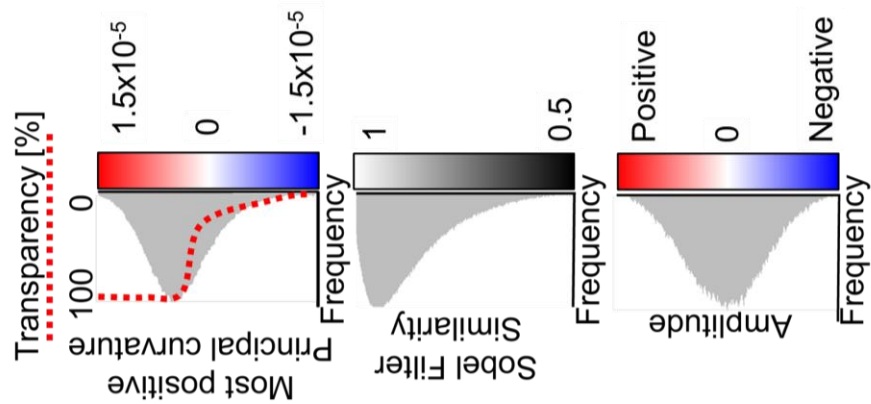


Figure 33. Phantom horizon slice 12 ms below the Pink Lime through the most positive principal curvature co-rendered with the Sobel filter similarity volume on the 1993-1996 vintage Watonga survey. Yellow arrows indicate incised channels. Notice how the edges of the channels are being delineated by the Sobel filter similarity and by the highest values of most positive curvature. A-A' and B-B' vertical sections through the main valley fill in the Red Fork Formation. Note that A-A' corresponds to B-B' and B-B' to C-C' on Figure 35.

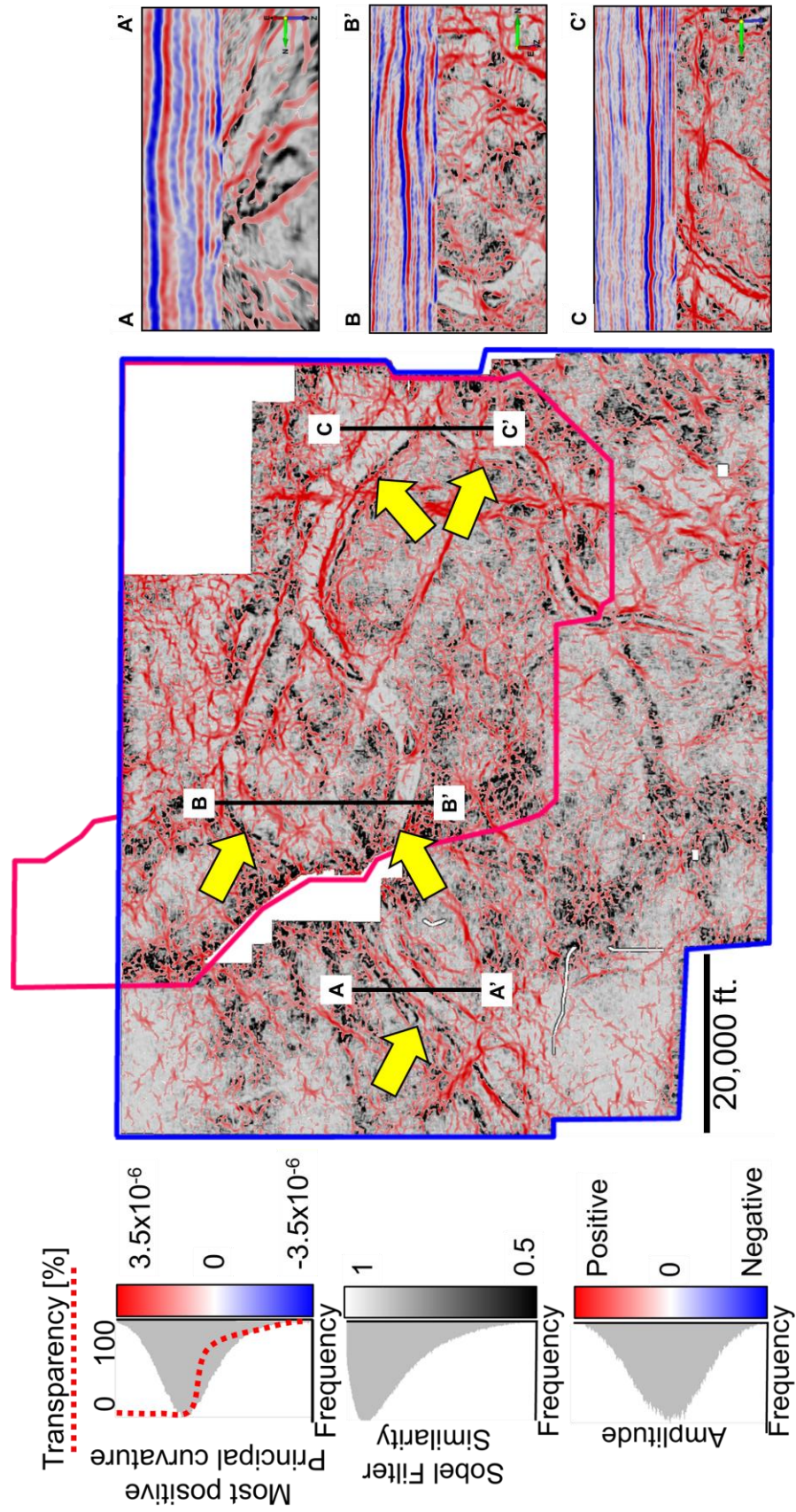


Figure 34. Phantom horizon slice 12 ms below the Pink Lime through the most positive principal curvature co-rendered with the Sobel filter similarity volume on the mega merged survey. Yellow arrows indicate incised channels. Notice the better delineation of the edges of the channels by the Sobel filter similarity and the highest values of most positive curvature. A-A', B-B' and C-C' vertical sections through the main valley fill in the Red Fork Formation.

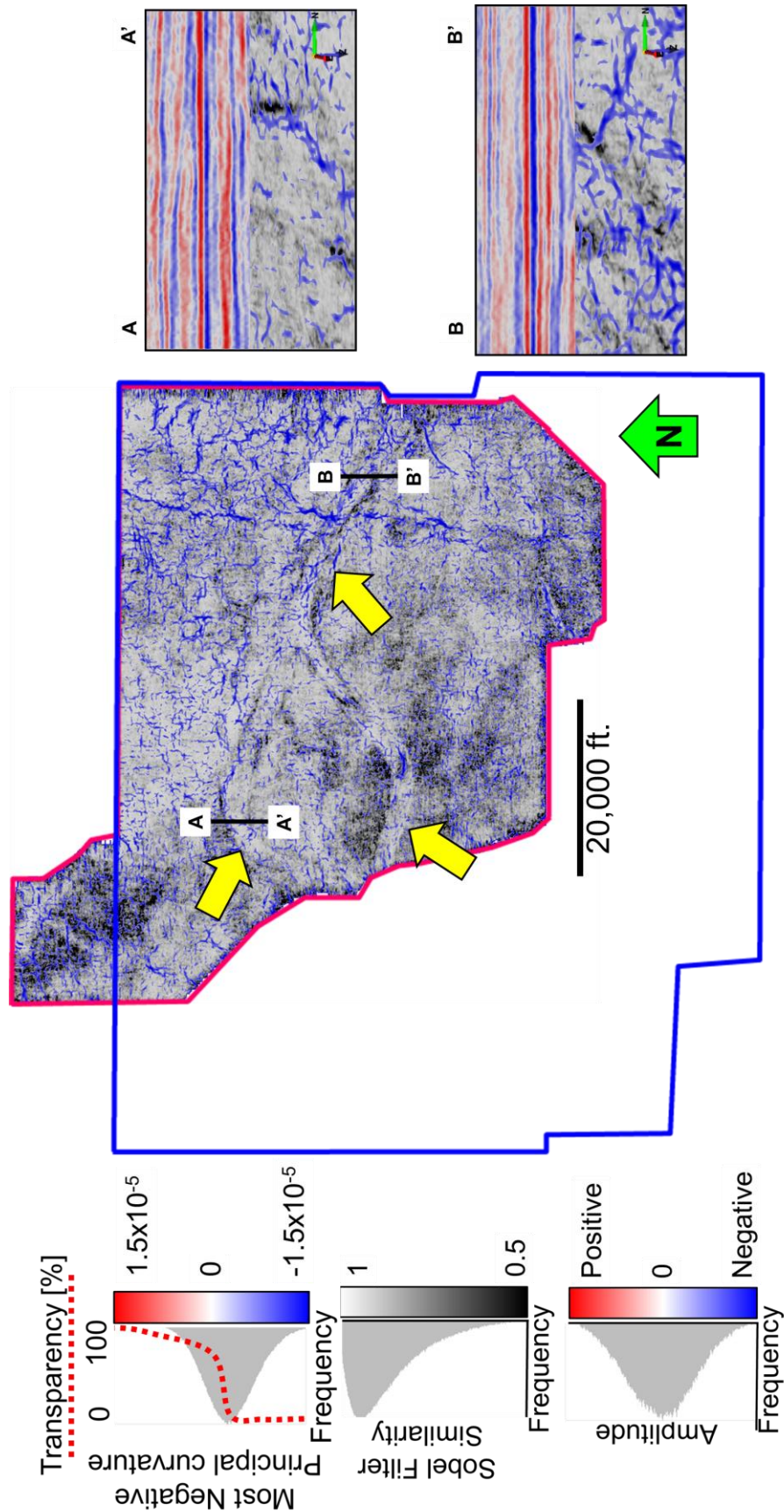


Figure 35. Phantom horizon slice 12 ms below the Pink Lime through most negative principal curvature co-rendered with the Sobel filter similarity volume on the 1993-1996 vintage Watonga survey. Yellow arrows indicate incised channels. A-A' and B-B' vertical sections through the main valley fill in the Red Fork Formation. Note that A-A' corresponds to B-B' to C-C' on Figure 37.

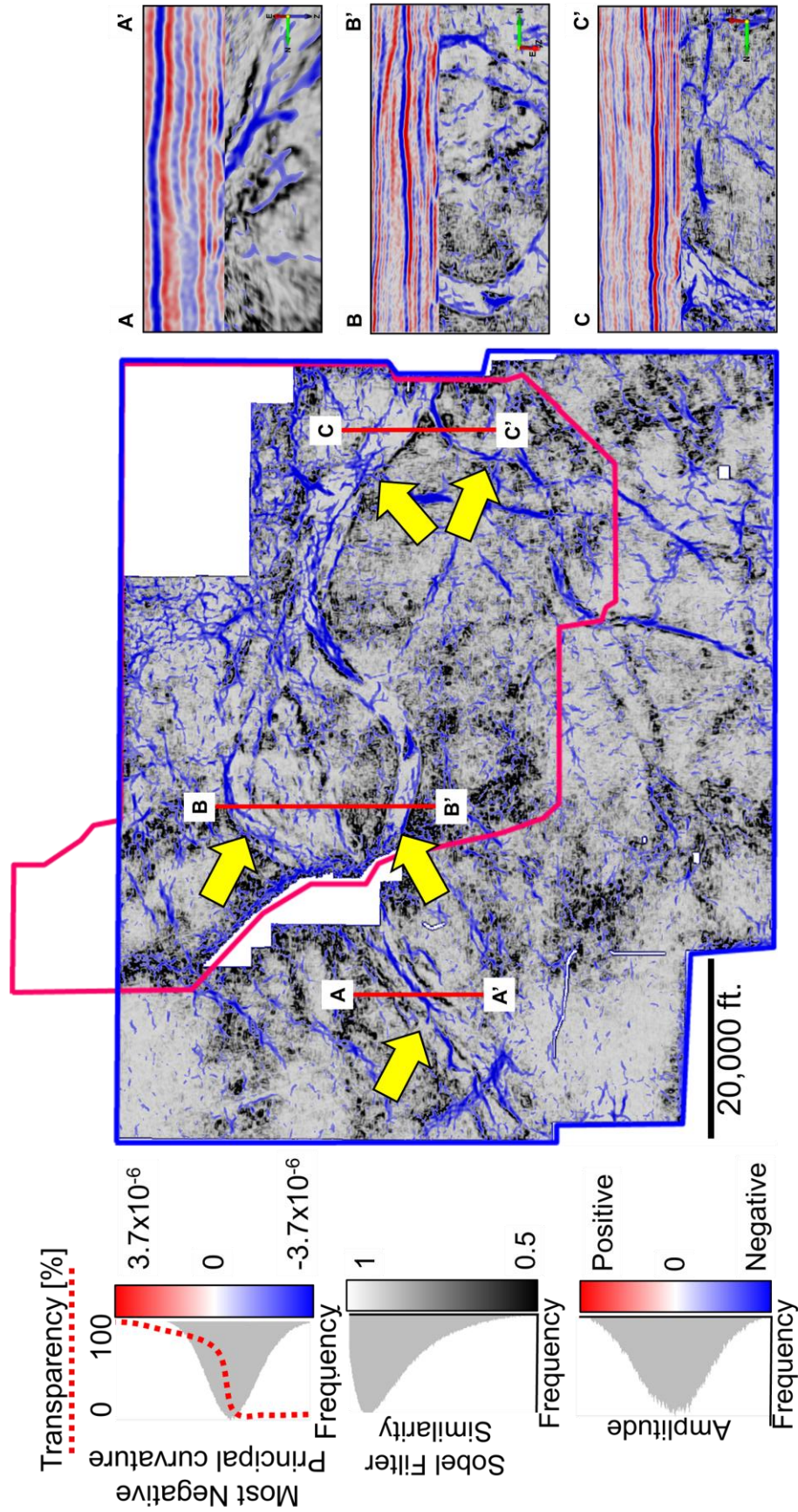


Figure 36. Phantom horizon slice 12 ms below the Pink Lime through the most negative principal curvature co-rendered with the Sobel filter similarity volume on the mega merged survey. Yellow arrows indicate incised channels. Notice how the edges of the channels are being delineated by the Sobel filter similarity and the lowest values of most negative curvature can be associated with the channel thalweg. A-A', B-B' and C-C' vertical sections through the main valley fill in the Red Fork Formation.

Spectral decomposition

Spectral decomposition is sensitive to subtle interference patterns, such as thin-bed tuning associated with channels in a plan view (Chopra and Marfurt, 2010). Since the data were previously spectrally whitened during the seismic processing stage, the spectral components exhibit the tuning effects of the geology with different channel thicknesses and infill exhibiting different spectral responses. In general, thinner beds will be better displayed with higher frequency components, and thicker beds with lower frequency components (Figure 37).

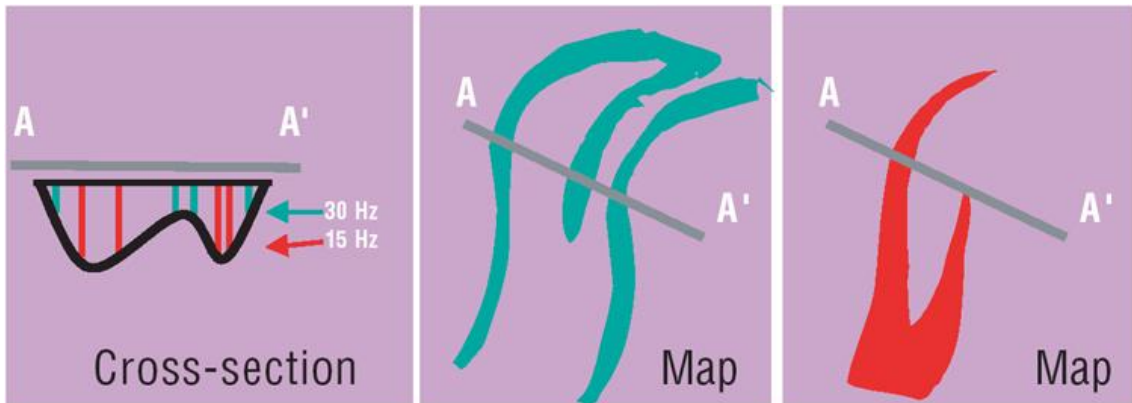


Figure 37. Schematic diagram showing the effect of thin bed tuning analyzed using different frequencies (After Laughlin et al., 2002).

In Figures 38 and 39, the 14 Hz, 34 Hz and 54 Hz spectral components are co-rendered along a horizon slice extracted 12ms below the Pink Lime Formation. Note how the stages of fill are defined by the different frequencies. The 14 Hz component is plotted against red and better delineates stages II, III and V. The 34 Hz component is plotted against green and delineates medium thickness stage V channels. The 54 Hz component is plotted against blue and delineates thinner stage V channels and part of stage III.

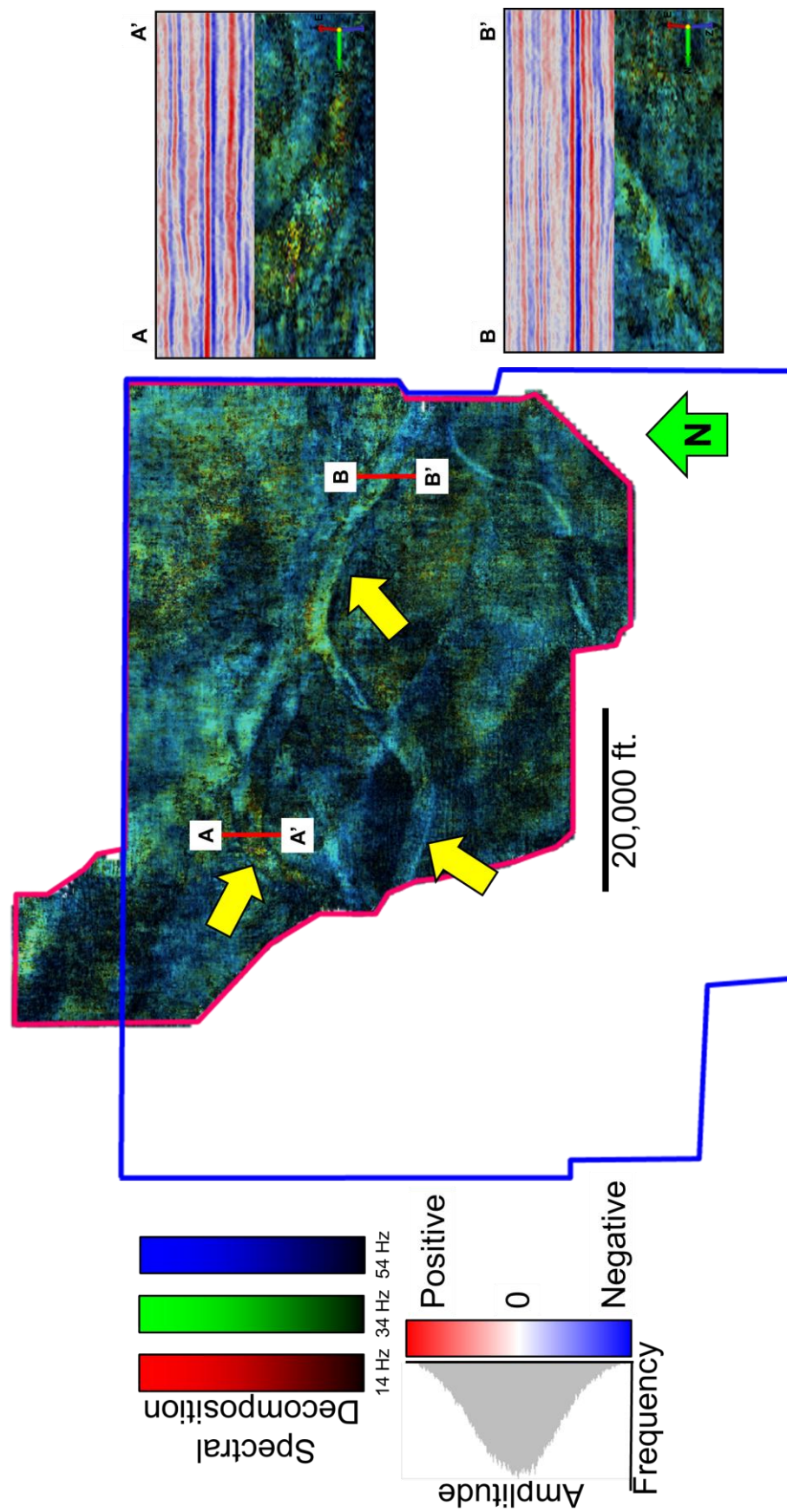


Figure 38. Phantom horizon slice 12 ms below the Pink Lime displaying channel features highlighted by three spectral frequencies at 14 Hz (red), 34 Hz (green), and 54 Hz (blue) on the 1993-1996 vintage Watonga survey. Yellow arrows indicate incised channels. A-A' and B-B' vertical sections through the main valley fill in the Red Fork Formation. Note that A-A' corresponds to B-B' and B-B' to C-C' on Figure 40.

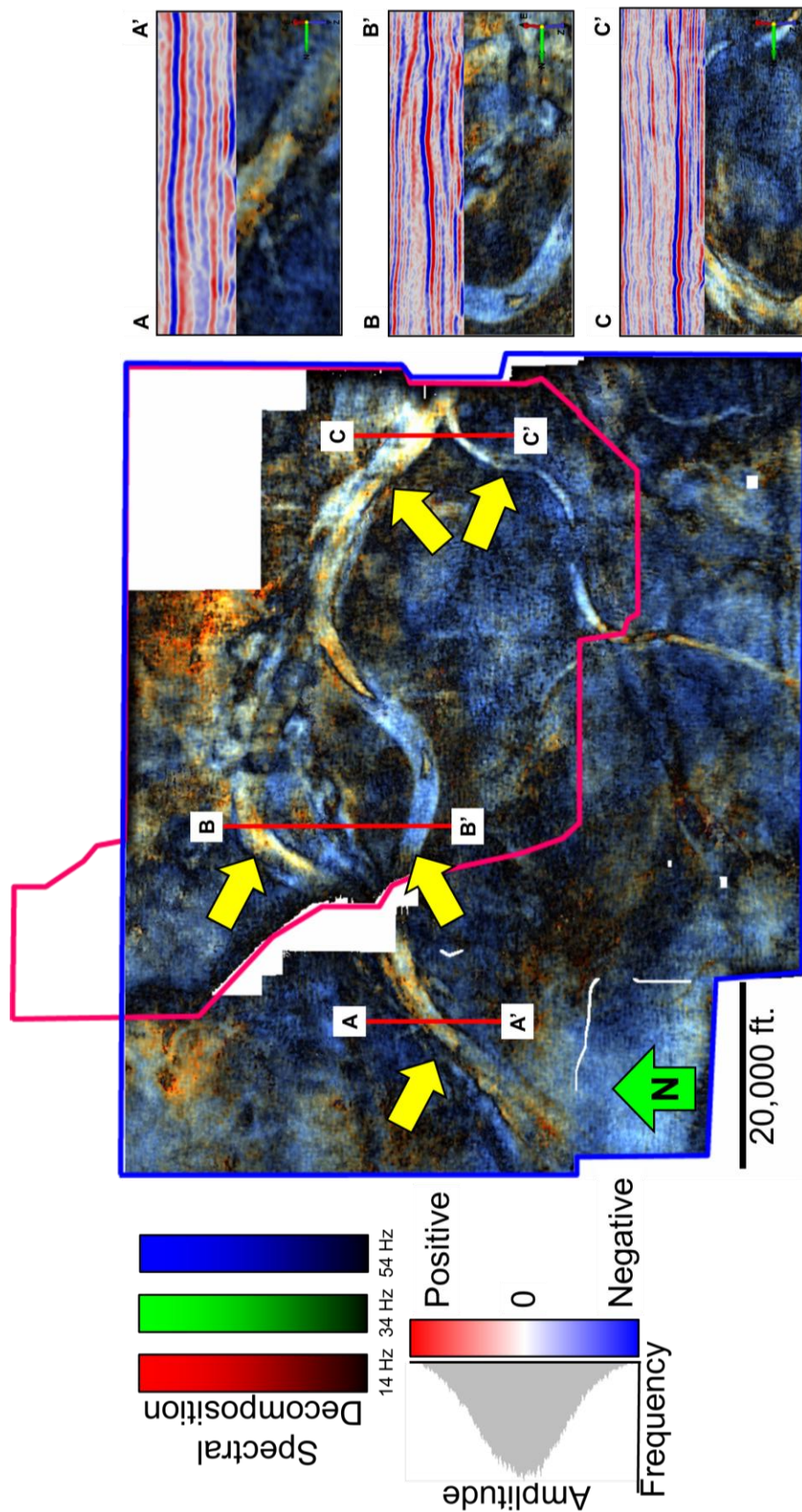


Figure 39. Phantom horizon slice 12 ms below the Pink Lime displaying channel features highlighted by three spectral frequencies at 14 Hz (red), 34 Hz (green), and 54 Hz (blue) on the mega merged survey. Yellow arrows indicate incised channels. A-A', B-B' and C-C' vertical sections through the main valley fill in the Red Fork Formation.

Coherent energy

The coherent energy attribute is a measure of the energy of the coherent component of the reflectors within the analysis window aligned along the dip and azimuth. High amplitude continuous features such as low impedance sands and high impedance limestones will exhibit high coherence energy. Low amplitude features (in this survey shale on shale reflectors) or high amplitude, incoherent features (such as karst in the deeper Hunton Formation) will exhibit lower coherent energy. A good way to better display the discontinuities, in this case channels, is to co-render the coherent energy attribute with the Sobel filter similarity (or any other edge detector attribute), such the channel features are better visualized. Channels will often give rise to a very abrupt lateral change in amplitude giving rise to a low Sobel filter similarity anomaly (Figures 40 and 41).

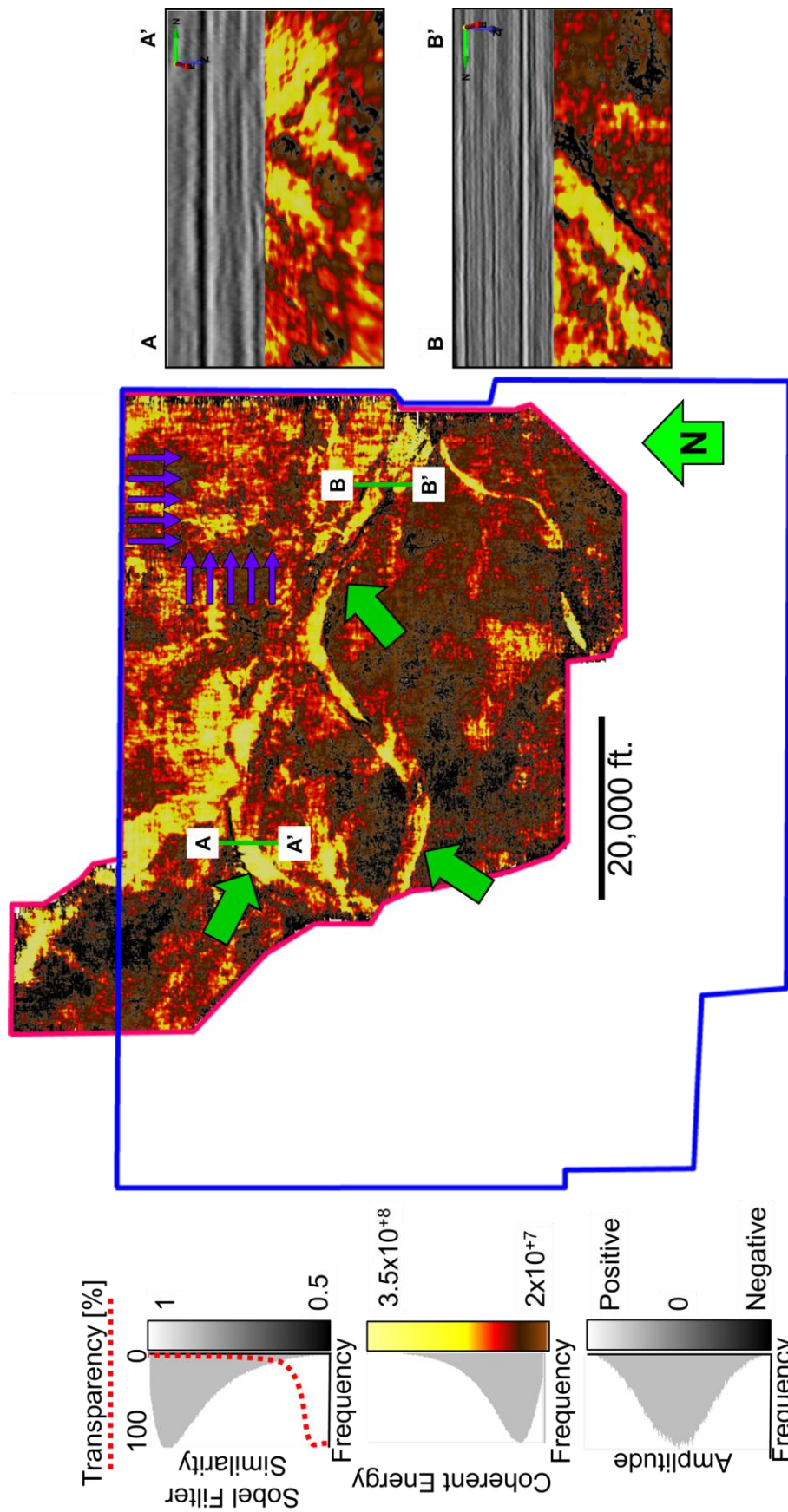


Figure 40. Phantom horizon slice 12 ms below the Pink Lime through the coherent energy co-rendered with Sobel filter similarity volumes on the 1993-1996 vintage Watonga survey. Green arrows indicate incised channels. Notice the delineation of the channel by the Sobel filter similarity and how the channels fills are being highlighted by the coherent energy. Purple arrows indicate NS-EW footprint. A-A' and B-B' vertical sections through the main valley fill in the Red Fork Formation. Note that A-A' corresponds to B-B' and B-B' to C-C' on Figure 44.

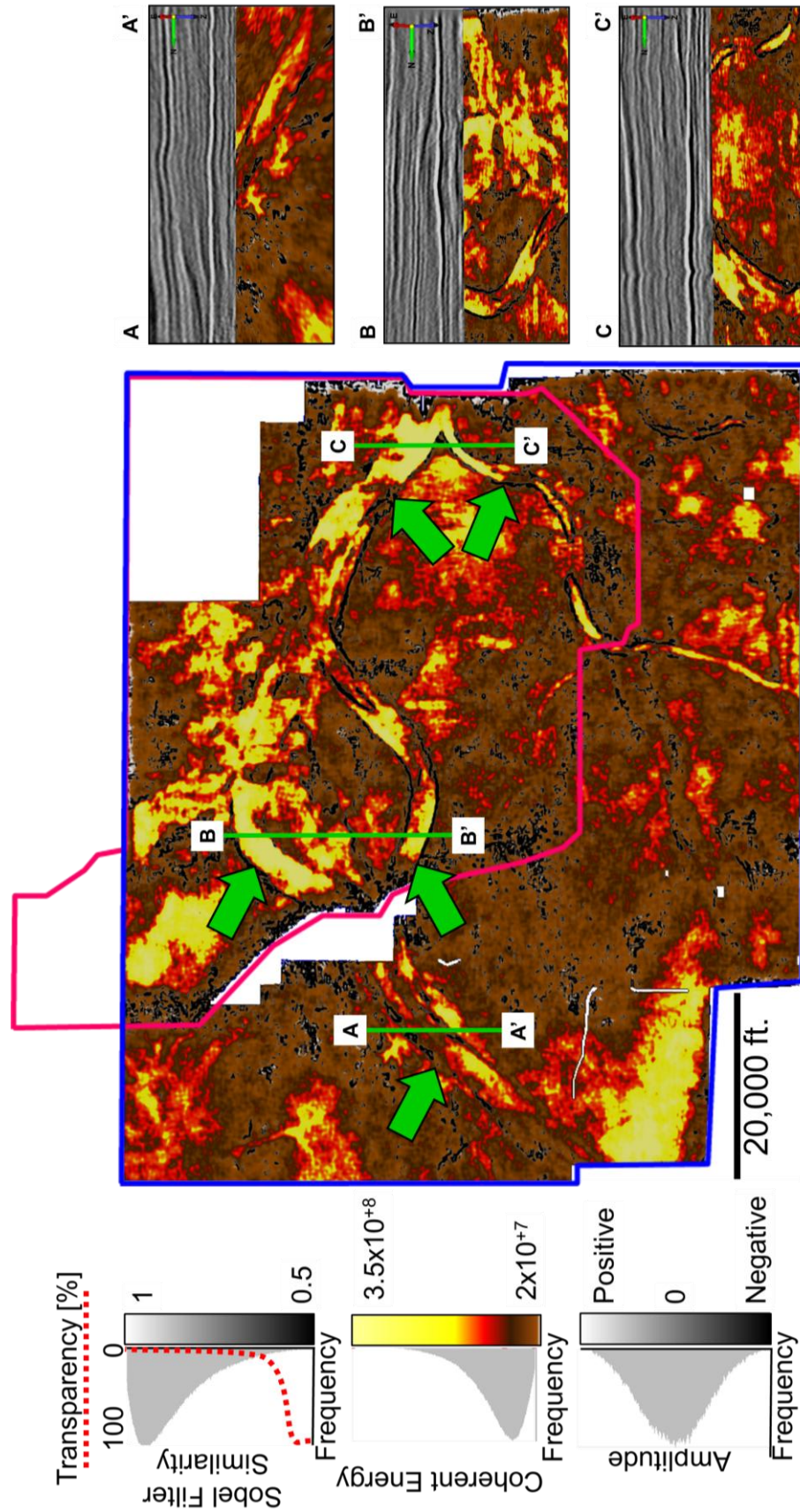


Figure 41. Phatom horizon slice 12 ms below the Pink Lime horizon through coherent energy co-rendered with Sobel filter similarity volumes on the mega merged survey. Green arrows indicate incised channels. Notice the delineation of the channel by the Sobel filter similarity and how the channels fills are being highlighted by the coherent energy. A-A', B-B', and C-C' vertical sections through the main valley fill in the Red Fork Formation.

Energy-weighted coherent-amplitude gradients:

The inline and crossline energy-weighted coherent-amplitude gradients are the horizontal derivatives of coherent energy in the analysis window (Chopra and Marfurt, 2007). They measure the lateral variation of amplitude across the analysis window along the dip and azimuth of the reflectors. When the gradients are high, there is a zone of rapidly varying high-amplitude coherent energy zone, and when the gradients are low, either the zone varies smoothly, has low energy, or the energy is incoherent.

These attributes emphasize subtle lateral changes in frequencies associated with edges. In this case study, the channel edges and the incoherent section of the channel fills are better highlighted using energy-weighted coherent-amplitude gradients co-rendered with coherent energy, than the similarity attributes previously presented (Figures 42-45).

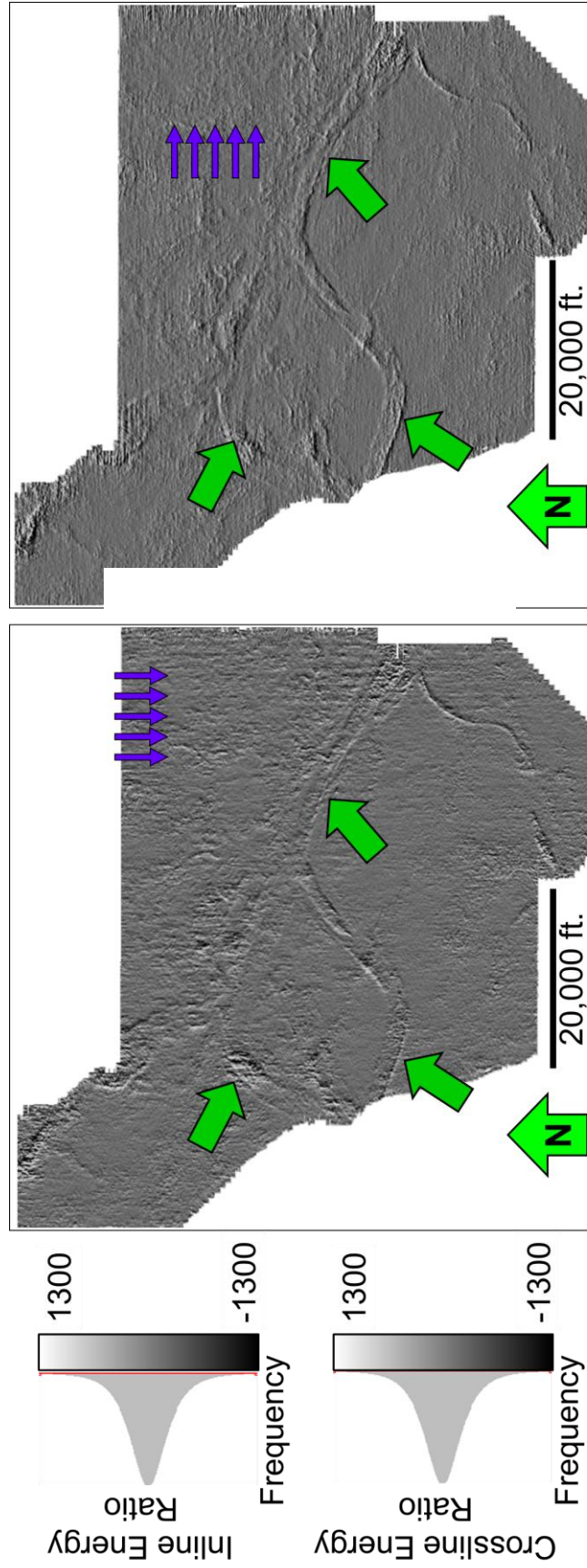


Figure 42. Phantom horizon slice at 12 ms below the Pink Lime on the Watonga survey through the inline coherent energy (left) and crossline coherent energy (right). Purple arrows highlight the strong acquisition footprint present in the seismic survey. Green arrows indicate incised channels.

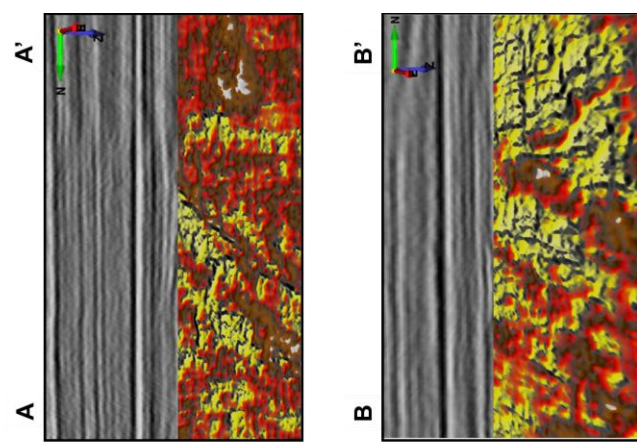
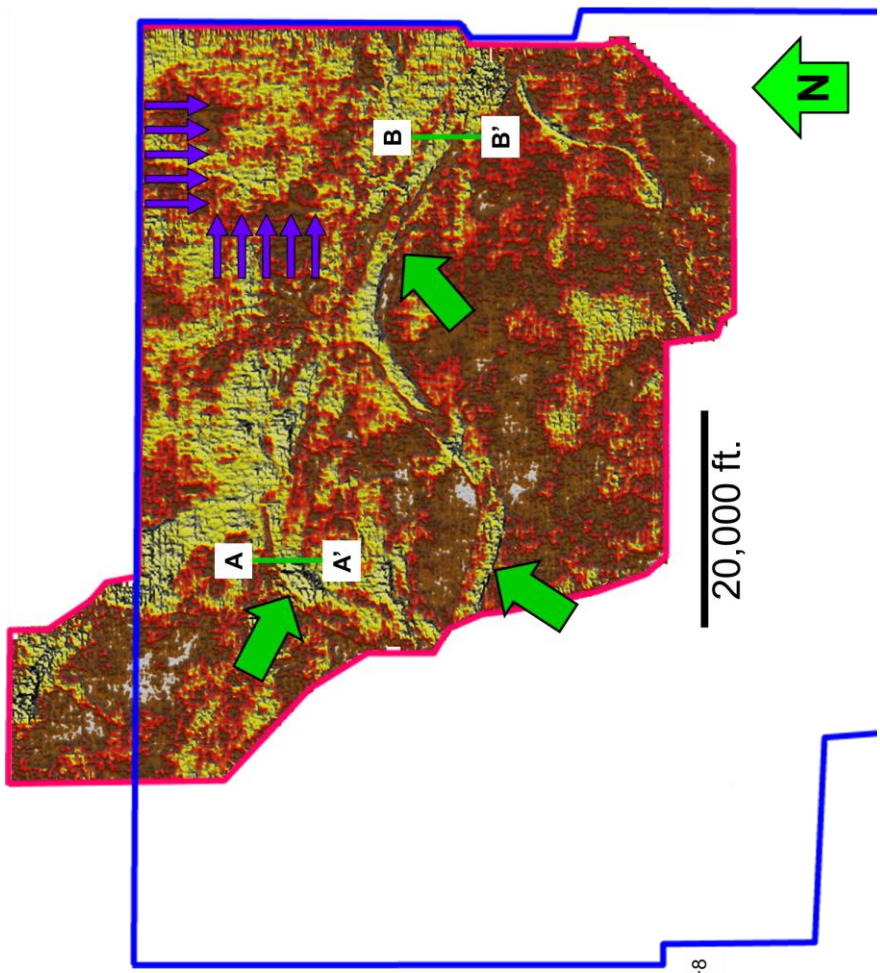
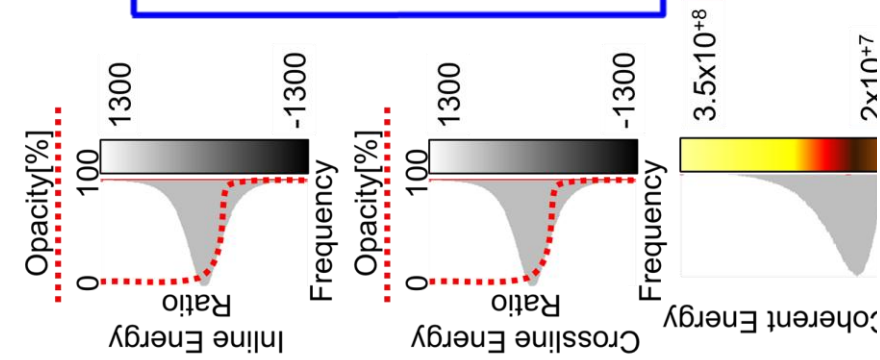


Figure 43. Phantom horizon slice at 12 ms below Pink Lime on the Watonga survey through the inline coherent energy co-rendered with crossline coherent energy and coherent energy volumes. Purple arrows highlight the strong acquisition footprint present in the seismic survey. Green arrows indicate incised channels. Notice the delineation of the channels by both coherent energy component and how the channels fills are being highlighted by the coherent energy. Purple arrows indicate NS-EW footprint. A-A' and B-B' vertical sections through the main valley fill in the Red Fork Formation. Note that A-A' corresponds to B-B' and B-B' to C-C' on Figure 46.

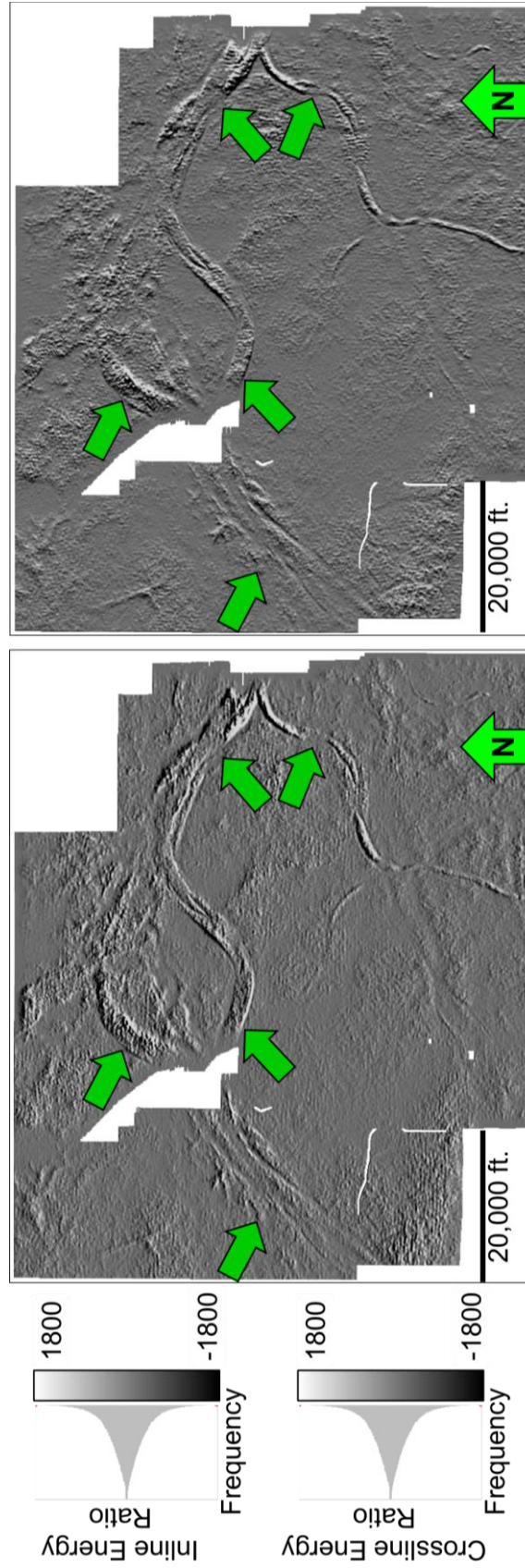


Figure 44. Phantom horizon slice at 12 ms below the Pink Lime on the mega merged survey through the inline coherent energy (left) and crossline coherent energy (right). Note that acquisition footprint has been diminished in the mega merged seismic survey, which increased the signal to noise ratio. Green arrows indicate incised channels better delineated in this seismic survey than in the Watonga.

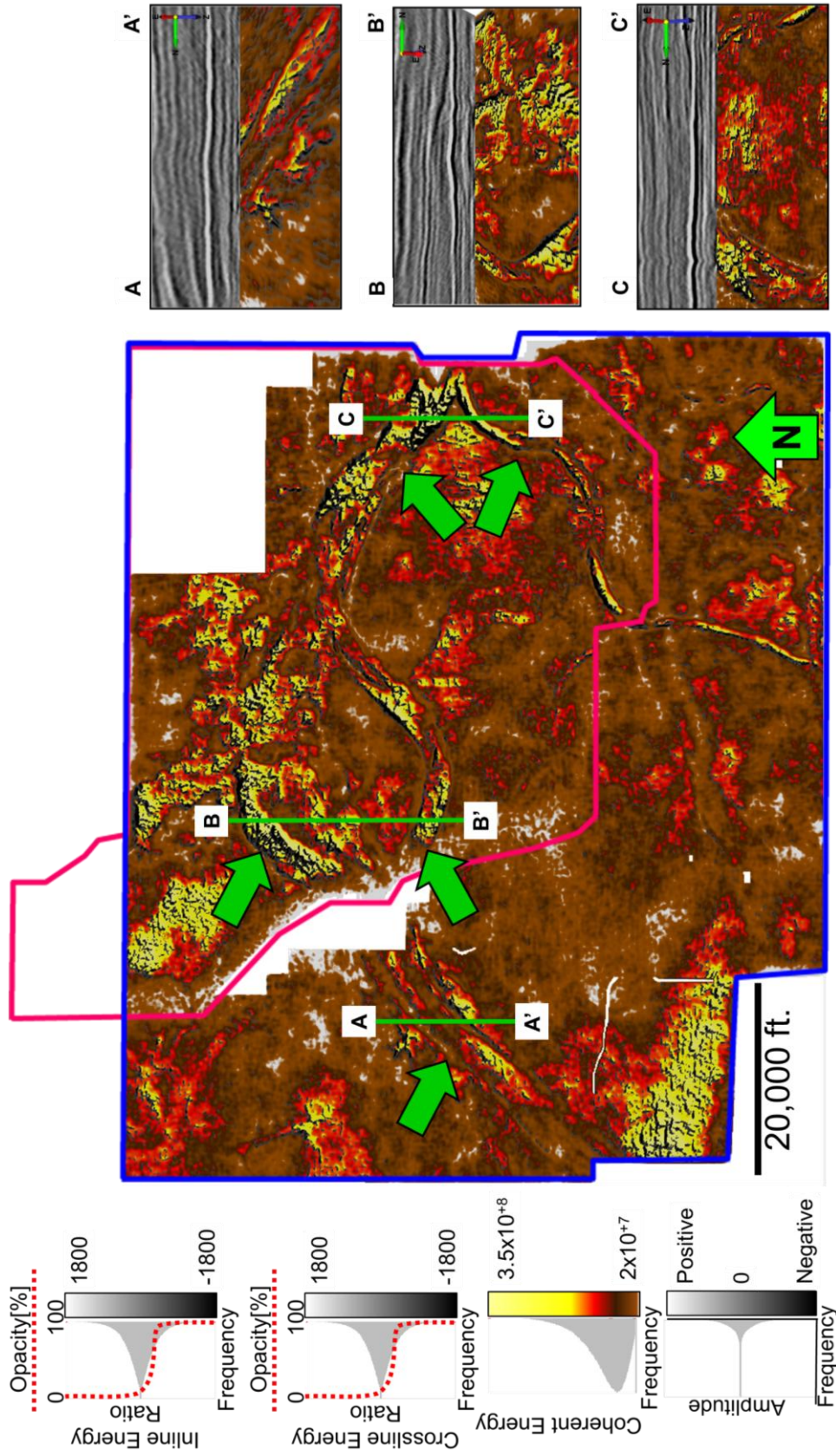


Figure 45. Phantom horizon slice at 12 ms below Pink Lime on the mega merged survey through the inline coherent energy co-rendered with crossline coherent energy and coherent energy volumes. Purple arrows highlight the strong acquisition footprint present in the seismic survey. Green arrows indicate incised channels. Notice the delineation of the channels by both coherent energy components and how the channels fills are being highlighted by the coherent energy. Purple arrows indicate NS-EW footprint. A-A', B-B', and C-C' vertical sections through the main valley fill in the Red Fork Formation.

Conclusions

Carefully re-processing of legacy seismic data can significantly improve the delineation of geologic features such as the Red Fork incised valleys.

Careful trace balancing diminishes acquisition footprint, which dominates not only edge-sensitive coherence and curvature attributes, but also spectral components and impedance inversion.

Merging multiple surveys not only improves the delineation of geology at the survey edges, but also by providing a larger view, places the acreage of interest into a larger depositional environment context.

CHAPTER IV

PETROPHYSICAL ANALYSIS

Well control

Although 1933 wells were available, only the ones that were located inside the seismic survey and had sonic and density logs were carefully analyzed, giving a final count of 22 wells which were used for petrophysical analysis and pre-stack seismic inversion. Figure 46 shows the distribution of these 22 wells with respect to the seismic coverage. The well density decreases to zero in the western part of the seismic survey because Chesapeake Energy does not operate in that area.

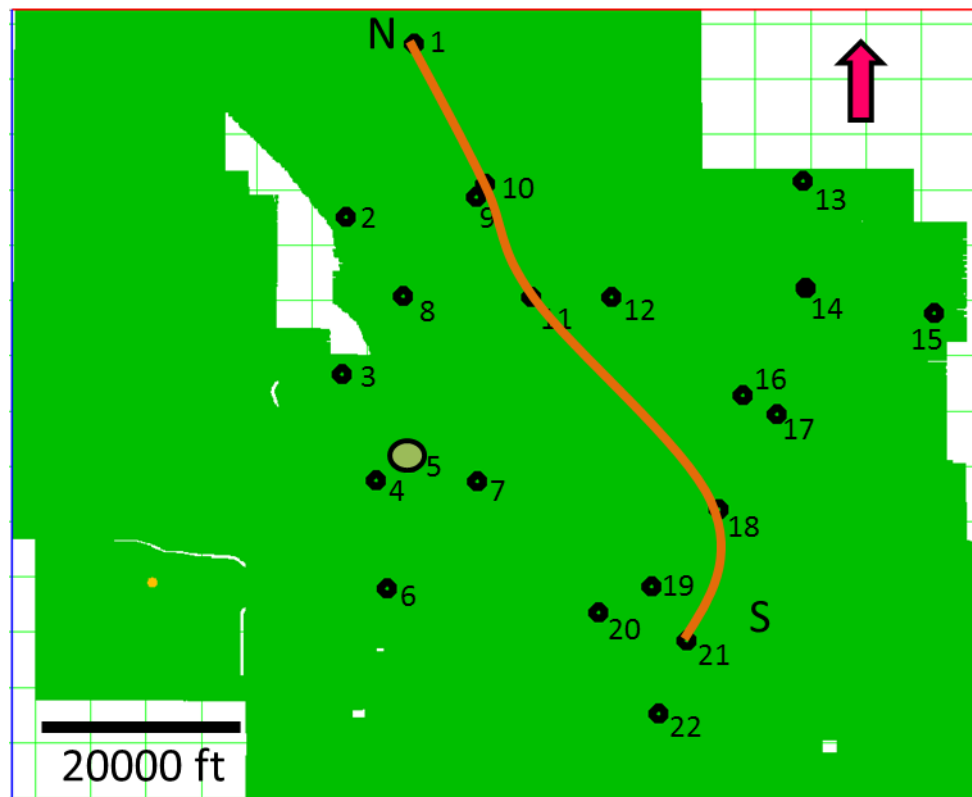


Figure 46. Seismic base map showing the distribution of wells with both density and sonic logs. Orange line represents the cross-section that will be displayed in subsequent figures.

Unfortunately only two wells have S-wave logs. Missing S-wave logs were thus reconstructed by multi-linear regression in four ways based on correlations of gamma ray, neutron porosity, density, and P-wave and S-wave logs in the two wells where they existed.

Figure 47 illustrates a good correlation between the predicted and the original S-wave on the two wells that had this log information. This quality control was done using a regression in which the two wells with the S-wave log were involved.

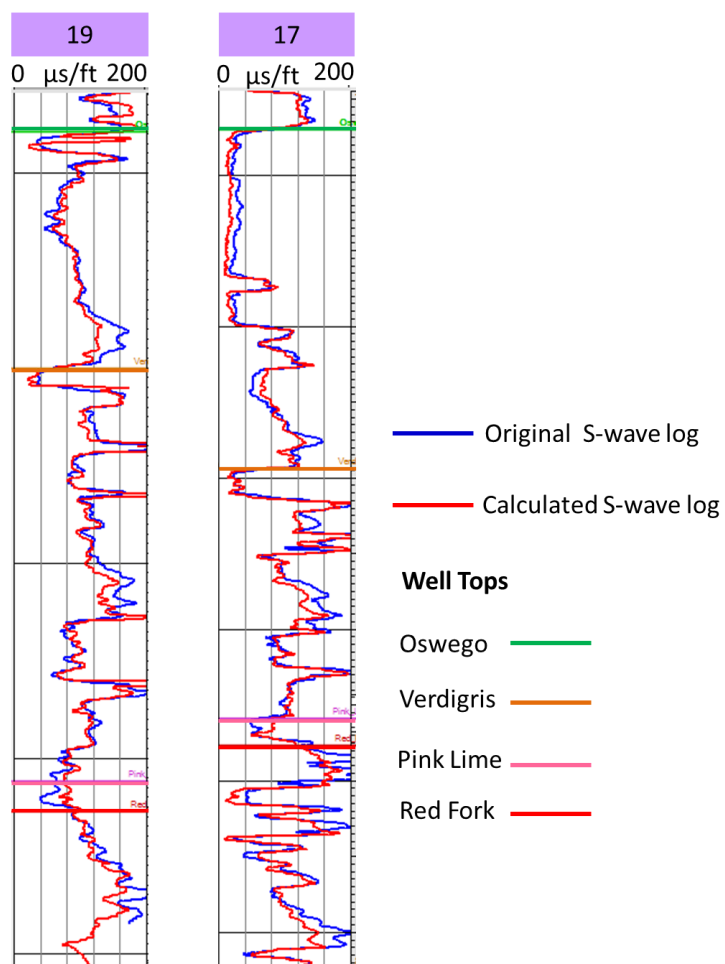


Figure 47. Quality control on the two wells that had S-wave logs. Note the similar trend of the estimated and measured S-wave log.

Figure 48 summarizes the workflow followed to achieve this calculation. In the case of missing one or two specific logs such as neutron porosity, the relationship is created with the remaining ones, but P-wave and density were considered to be essential input for every multi-linear regression.

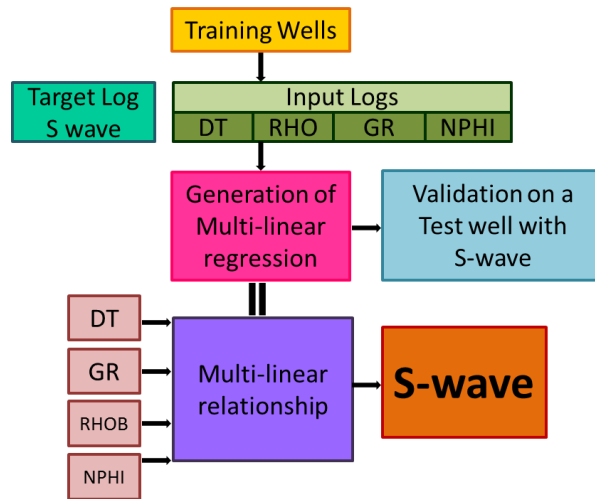


Figure 48. Workflow for S-wave log estimation from more common sonic (DT), gamma ray (GR), density (RHO), and neutron porosity (NPHI) logs.

Facies, V_{sh} and porosity calculation

Limestone, sandstone and shale facies were classified using different cut offs for each well. In some wells, the gamma ray log was insufficient to discriminate the three lithologies, for that reason density and photoelectric factor were combined with the gamma ray log to obtain the result. Lithology discrimination between clastics and limestones using gamma ray logs is only possible if the clastics contain mica, potassic feldspar, shale or other radioactive mineral.

The volume of shale, V_{sh} , present in each formation was calculated using two formulae based on the logs present in each well. If the gamma ray log was available, I used:

$$V_{sh} = \frac{GR - GR_{Min}}{GR_{Max} - GR_{Min}} . \quad (1)$$

In the absence of a gamma ray log, I used the neutron porosity :

$$V_{shND} = \frac{\phi_N - \phi_D}{\phi_{N(shale)} - \phi_{D(shale)}} , \quad (2)$$

where ϕ_N is the log value for neutron porosity and the density porosity is defined by

$$\phi_D = 100 \frac{2.65 - RHO_B}{2.65 - 1} . \quad (3)$$

The neutron porosity, ϕ_N used in equation 2 was corrected assuming a sandstone matrix based on Figure 49 to define the sandstone matrix neutron porosity, $\phi_{N_{SS}}$, using

$$\phi_{N_{SS}} = 1.055\phi_N + 1 . \quad (4)$$

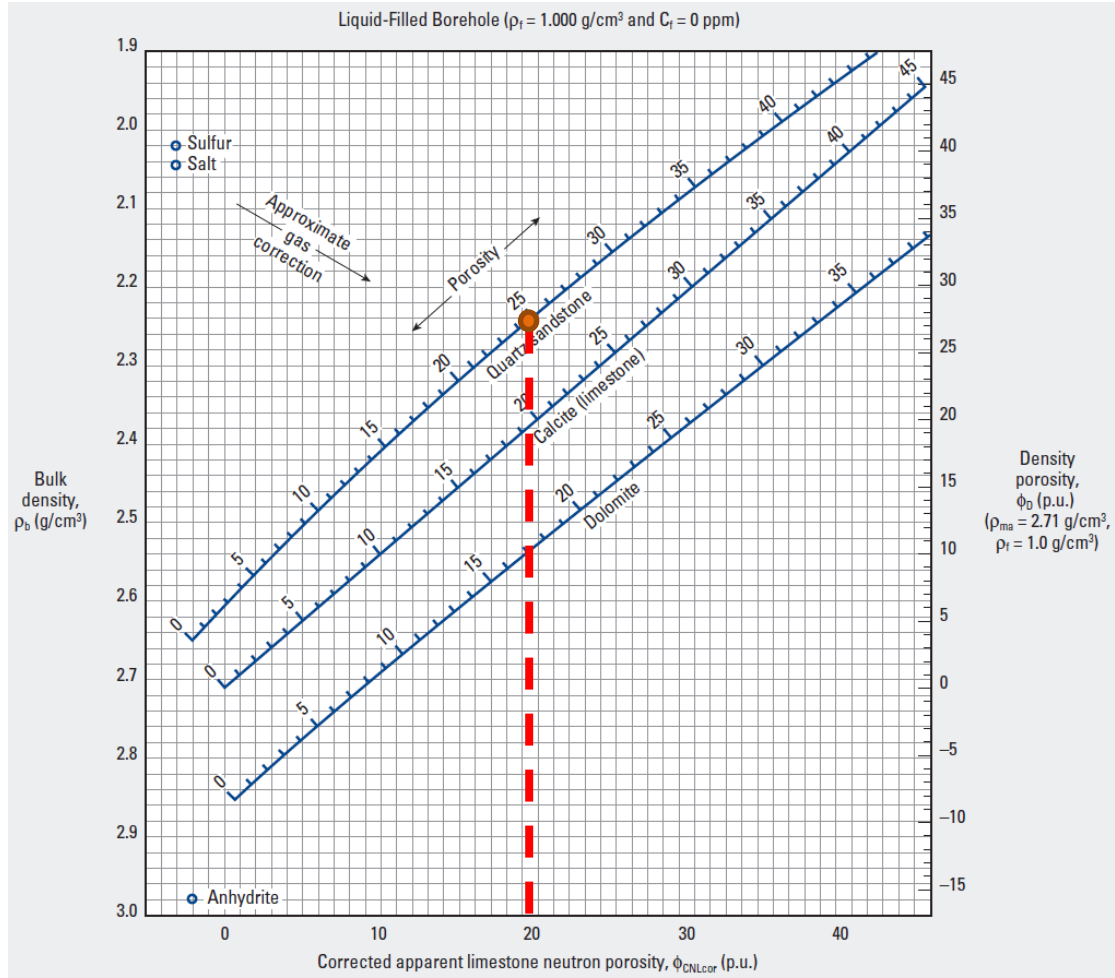


Figure 49. Apparent limestone neutron porosity correction chart used to obtain neutron porosity values of a sandstone matrix. The left ordinate is the bulk density of the rock. The right ordinate is the density porosity of the rock and the abscissa is the corrected neutron porosity in a limestone matrix. Assuming a sandstone matrix equal to $\phi_{N_{SS}} = 25\%$ (orange dot), the corrected neutron porosity is equal to $\phi_{CNLCOR} = 20\%$. This linear relationship can be applied to well logs. (After Schlumberger, 2009)

After calculating V_{sh} , the effective porosity, ϕ_E , was estimated using

$$\phi_{Edensity} = \phi_D - V_{sh}\phi_{sh} \quad (5)$$

where ϕ_{sh} is the value used as a density porosity discriminating parameter for a clean shale. Each well in this project has a different discriminating parameter value. I used effective porosity log, ϕ_E , in the geologic interpretation combined with the well-tie

seismic inversion results to differentiate those channels that are filled with porous sand from those filled with shale.

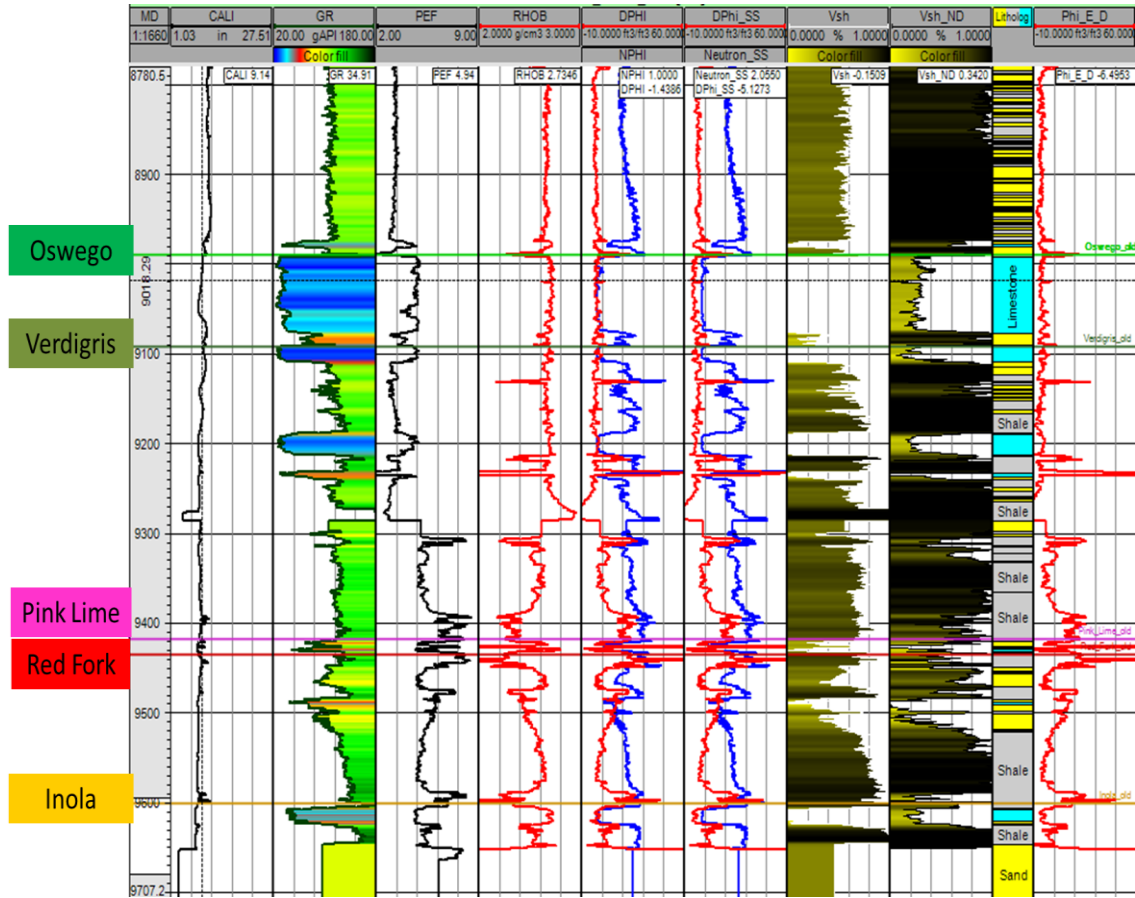


Figure 50. A representative suite of logs from well 5 displaying track 1: caliper, track 2: gamma ray, track 3: photo electric factor, track 4: density, track 5: density and neutron porosity, track 6: corrected sandstone matrix density and neutron porosity, track 7: volume of shale using equation 1, track 8: volume of shale using equation 2, track 9: facies and track 10: calculated effective porosity.

Figure 51 shows a cross-section of facies distribution across the main channel system. Note how the interval Oswego-Verdigris thickness decreases from North to South. The overall shale content on the Red Fork-Inola interval is very high with more limestone found in the southern part of the cross-section (Figure 52).

Figure 52 is a NS cross-section showing the V_{sh} distribution for the profile in Figure 46. In limestone formations the content of V_{sh} decreases to almost zero. Within the Red Fork zone a high content of V_{sh} is found.

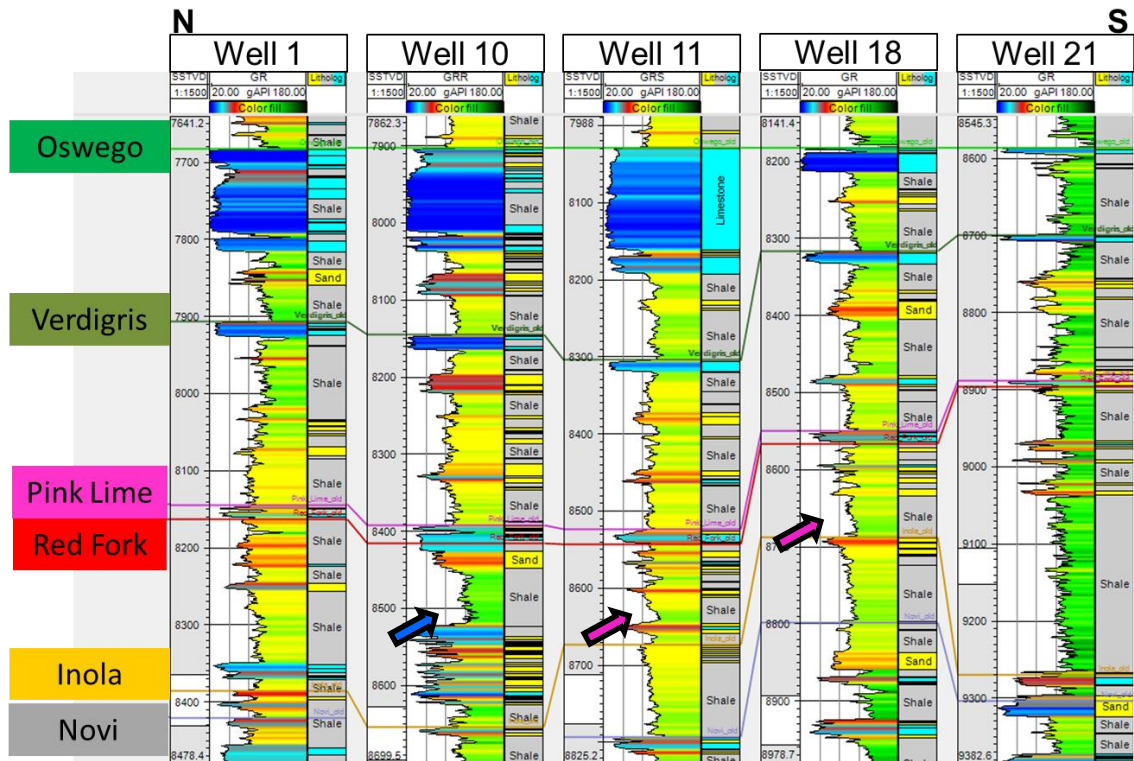


Figure 51. Cross-section showing facies distribution along the main incised valley fill system. Location of wells shown on Figure 47. Blue arrow shows the high content of sand found in Stage III while Stage V penetrated by wells 11 and 18 shows high shale content according to the facies analysis based on the GR and PEF cutoff for each well.

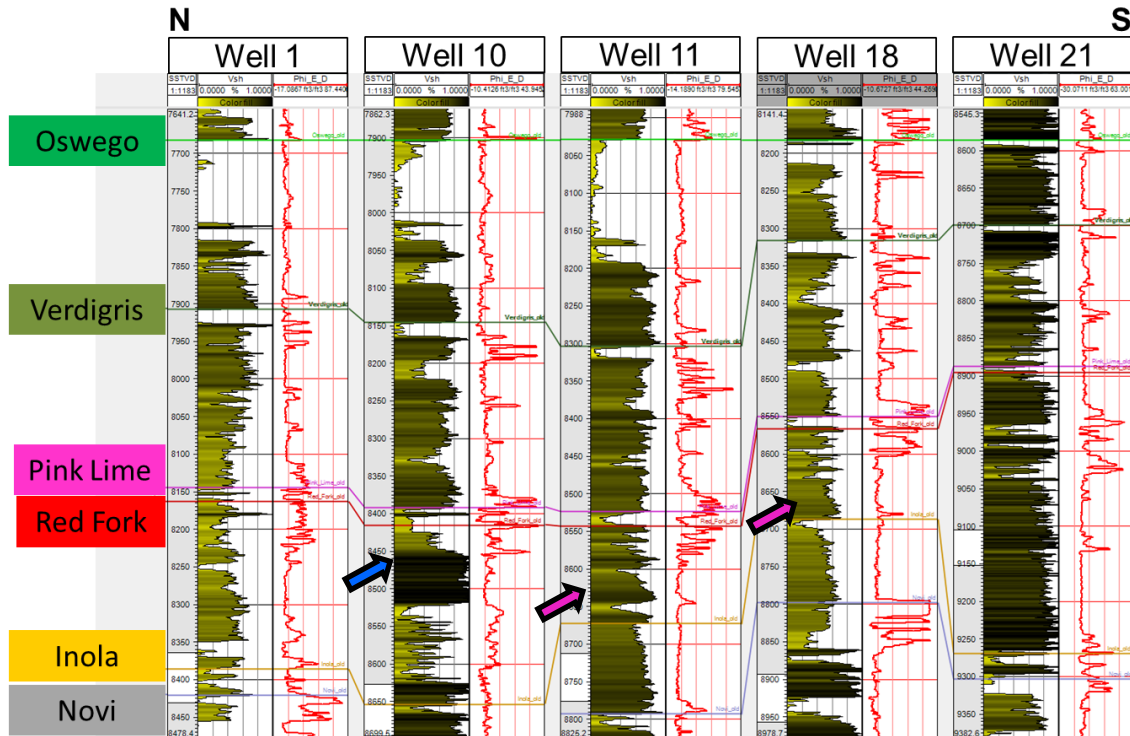


Figure 52. Cross-section showing facies distribution along the main incised valley fill system. Location of wells shown on Figure 47. Blue arrow shows the high content of sand found in Stage III while Stage V penetrated by wells 11 and 18 shows interbedded sands and shale according to Vsh analysis based on the GR cutoff for each well.

Lithology discrimination using cross-plots

Cross-plotting different petrophysical parameters using well log data provides discrimination between sandstone, shale and limestone. These results are then applied to the geologic interpretation of the incised valley fill deposits.

Sand and shale lithologies are poorly discriminated in the $\lambda\rho\text{-}\mu\rho$ crossplot (Figure 53a). A more subtle discrimination is observed in the average porosity vs. P - and S -impedance, as indicated by the ovals in Figure 53c. Discrimination between lithologies is possible on the various crossplot spaces because each different lithology type (sand, shale, limestone, etc.,) has unique elastic properties, such as differences in Young's modulus, Poisson's ratio, and mineralogic content.

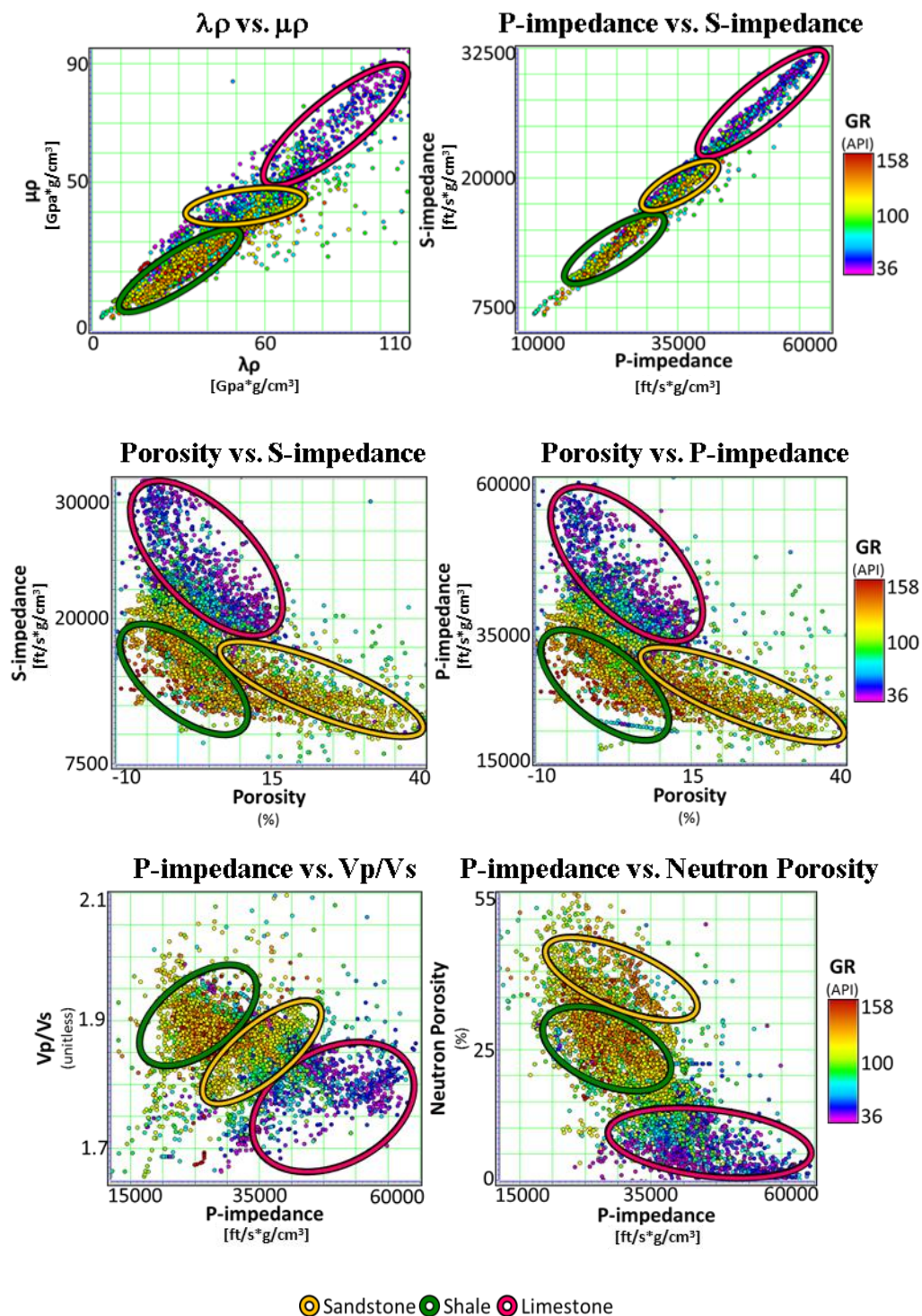


Figure 53. Petrophysical parameters cross-plots using GR log as lithology discriminator. Note that shale-sandy zones have low values of $\lambda\rho$ - $\mu\rho$ and high values of GR. Limestone zones have high values of $\lambda\rho$ - $\mu\rho$ and low GR and porosity and Sandstones have high porosity and intermediate $\lambda\rho$ - $\mu\rho$ values.

CHAPTER V

SEISMIC INVERSION

Introduction

Unlike amplitude that measures relative changes in rock properties, seismic inversion is directly correlated to the rock properties of each lithologic unit (Swisi, 2009). Impedance is the product of intrinsic properties of the rock such as P-velocity and density, ρV_P , and S-velocity and density, ρV_S . These rock properties can be extracted from well-log measurements and, by tying the wells to the seismic amplitude, these seismic impedances provide estimates of rock properties such as porosity that are used to characterize the reservoir.

In order to obtain an accurate estimation of rock properties from seismic, the latter need to be properly conditioned. In this chapter, I will give an overview of the data conditioning process done in order to invert from the pre-stack seismic P- and S-impedances, which are used as input to estimate other rock properties necessary to evaluate the incised valley fill system in the Red Fork Formation.

Data conditioning

My input data consist of pre-stack time migrated gathers from the mega merged survey. Figure 55 illustrates the seismic data conditioning workflow I applied to the already time processed mega merged survey in order to run the simultaneous pre-stack seismic inversion. Refer back to Table 2 for information on the time processing of the data.

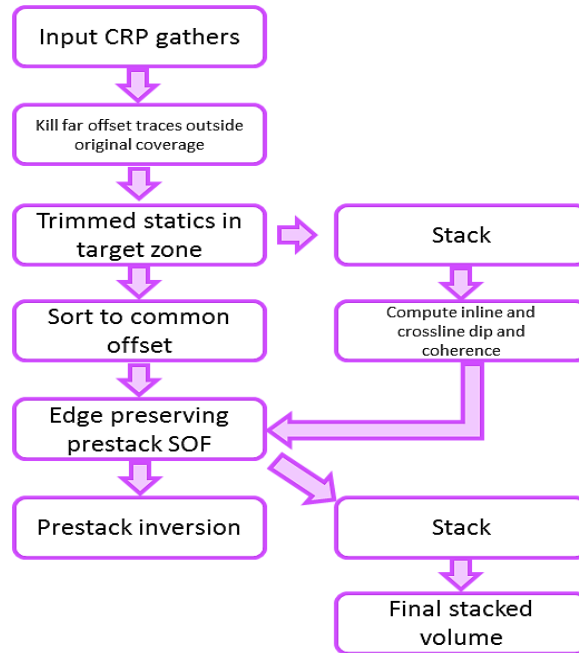


Figure 54. Data conditioning workflow

I first used trimmed statics in order to condition the seismic data for pre-stack inversion (Figure 56b). Trimmed statics estimates an optimal shift to apply to each trace in a gather within a target zone, by cross-correlating each trace with a reference stacked trace to correct any residual moveout or time miss-alignment. The evaluating window used in the alignment process of the traces was 100 ms about the strong, coherent “Below Nv.” horizon, allowing a 10 ms range maximum shift.

Structural Oriented Filtering, SOF, was applied to the pre-stack common-offset gathers after trimmed statics correction using the inline and crossline dip computed from the stacked volume. This process retains the coherent component of the signal and rejects events inconsistent with the dip.

Figure 56 shows a CRP gather of the seismic data before and after applying SOF and trimmed statics. Note that the zone of interest is between the Pink Lime and Novi horizons. Therefore trimmed statics parameters were chosen taking into account that the

most optimum results should be good for the entire volume and not only for the interval of interest.

Figure 55 illustrates how the amplitude spectrum increases after applying the structurally oriented filter, which will benefit the channel features delineation.

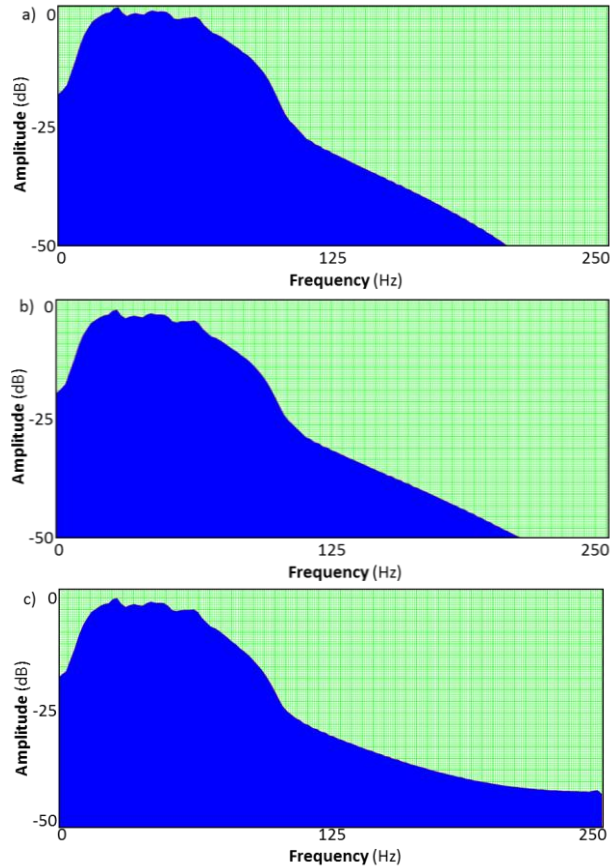


Figure 55. Amplitude spectrum of the prestack mega merged survey from 1750-2000 ms (a) original (b) after Trimmed statics, and (c) after SOF. Since no spectral balancing was applied and the data were not stacked, the spectrum is effectively unchanged.

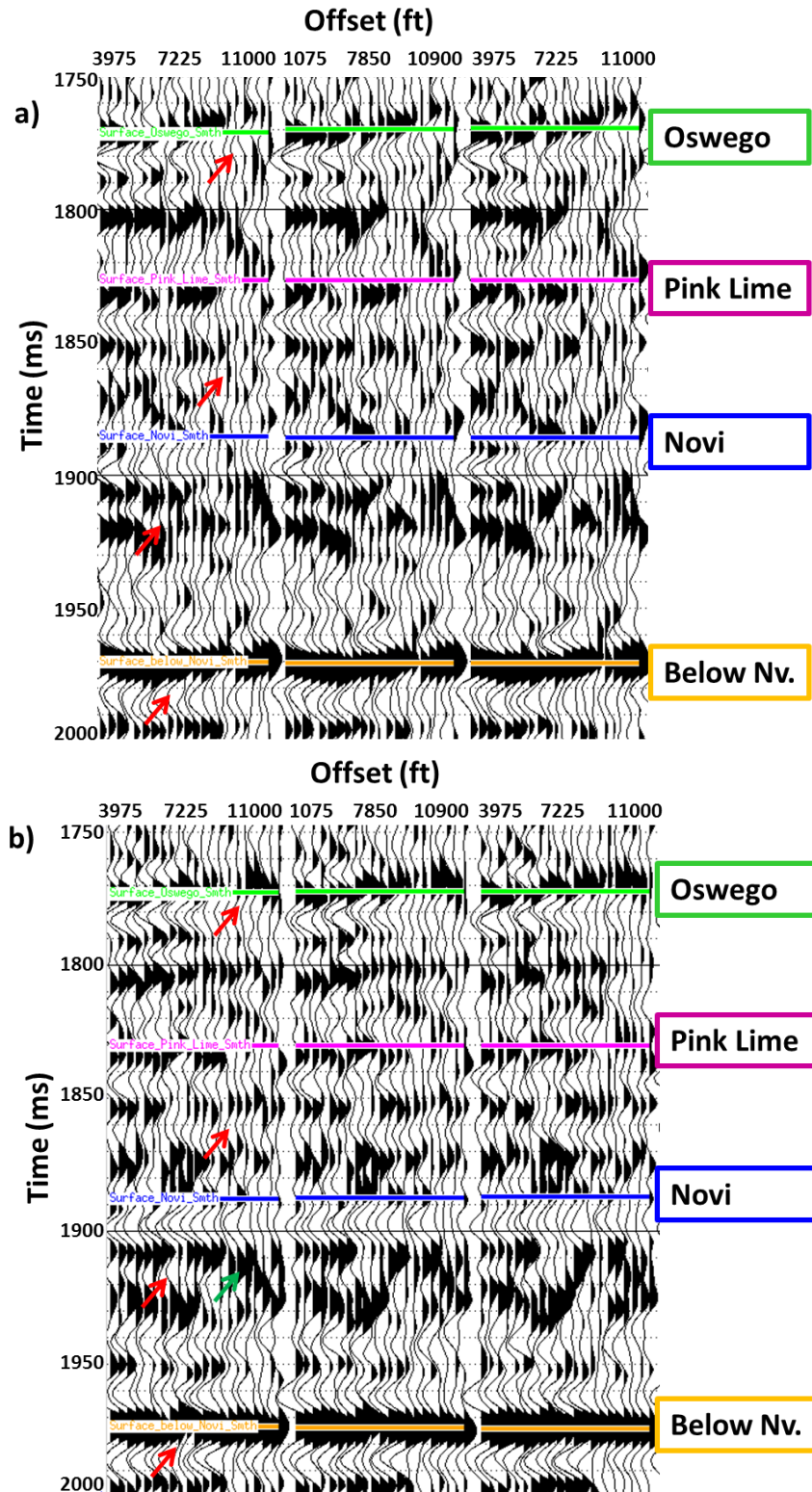


Figure 56. Representative CRP gathers of the (a) original seismic data and (b) after aligning the reflectors with trimmed statics along the Bellow Nv. horizon.

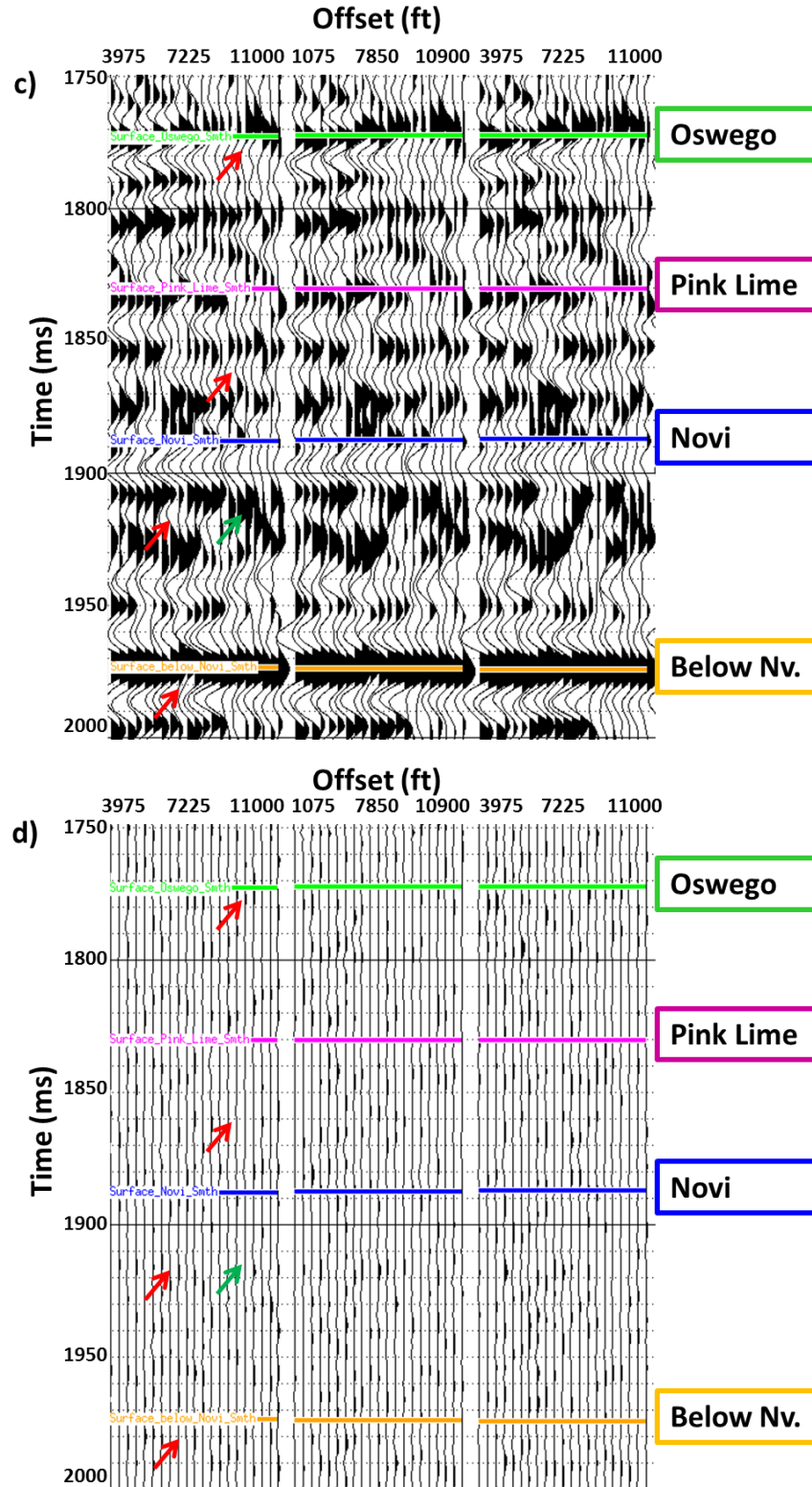


Figure 56. Representative CRP gathers of the original seismic data (c). Removed noise from the applied SOF (d). Red arrows indicate the improvement along the reflectors. Green arrow highlights improvement after applying SOF. The zone of interest is between the Pink Lime and Novi horizon. Trimmed statics were computed about the strong "Below Nv" horizon.

Simultaneous pre-stack seismic inversion

Barber (2010) showed in a nearby survey that acoustic impedance was insufficient to discriminate between Red Fork sands and shales. Pre-stack inversion uses the variations of reflection amplitudes within the individual migrated common reflection point gathers (CRP) to extract the elastic properties, Z_P and Z_S or alternatively $\lambda\rho$ and $\mu\rho$, from the zone of interest. For quality long-offset data one may also estimate density, ρ . The stacked seismic volume is tied to the wells in the area, and its crosscorrelation coefficient ranges from 0.6 to 0.7. In this process the seismic was tied to the Oswego lime horizon, which is a strong peak reflector corresponding to the high impedance contrast with the overlying Cleveland sandstone. The Pink Lime is a weaker reflector that overlies the Red Fork channels. Its structural time map is shown in Figure 12.

Figure 17 illustrated how the seismic data degrade beyond 11000 ft offset, or approximately 28° . Examining the gathers shown in Figure 18, note the absence of far offsets information in much of the survey. The reflectors at far offsets are not well aligned with migration moveout artifacts from the surrounding wider offset legacy surveys filling the gap. I therefore generated two seismic inversions: the first one with angles ranging from 5 to 27 degrees, and a shorter offset inversion ranging between 4 to 20 degrees range.

For both seismic inversions, 4-20 and 5-27 degree offset, statistical wavelets were used. The wave extraction parameters are shown in Table 3 and resulting wavelets in Figures 57 and 58.

Zero-phase wavelet extraction parameters	
Top limit	-50 ms from Oswego Surface
Bottom limit	+50 ms from Novi Surface
Wavelet length	120 ms
Taper length	25 ms
Sample rate	2 ms
Phase rotation	0 degrees
Phase Type	Constant Phase

Table 3. Wave extraction parameters to generate far, middle and near offset wavelet.

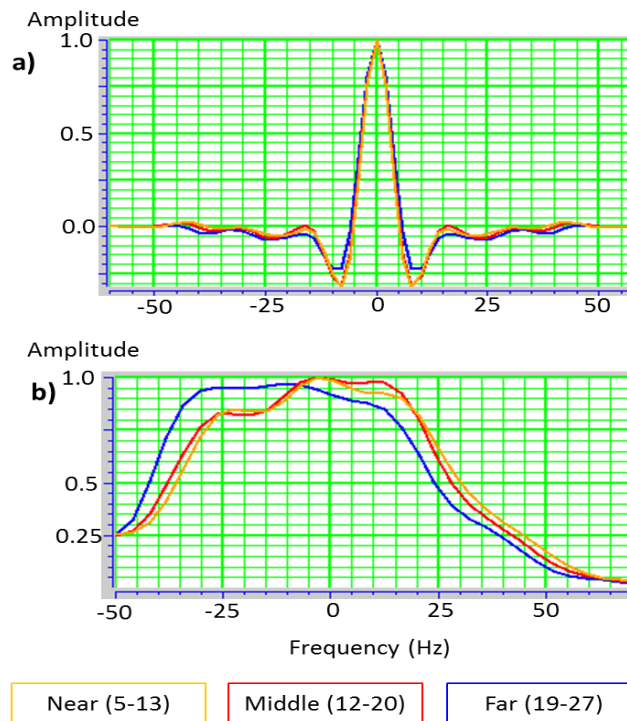


Figure 57. Wavelet extraction for angle gathers of 5-27 degrees of offset: (a) Time domain wavelets and (b) their corresponding frequency spectrum.

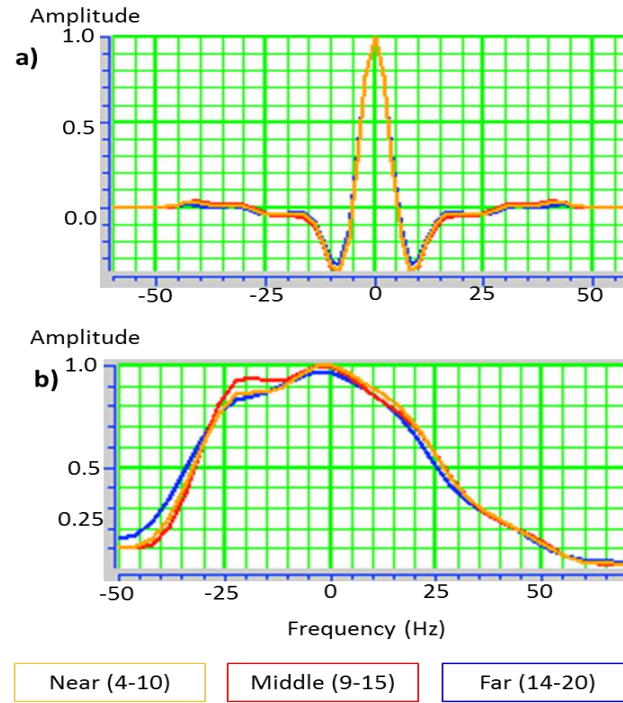


Figure 58. Wavelet extraction for angle gathers of 4-20 degrees of offset: (a) Time domain wavelets and (b) their corresponding frequency spectrum.

I used modelbased simultaneous inversion to extract the P- and S-wave impedances tied to the well log information. The low frequency model was built from the well logs and seven interpreted horizons (Figures 63 and 64).

Comparing the error between the original well log P- and S- impedance and the inverted seismic data during the preparation process for seismic inversion provides quality control of the results. To do so, the error of each inverted rock property over each well is analyzed. Figure 59 shows the normalized RMS error of the P-wave and S-wave impedances using the 4°-20° inversion angle range and the one extracted from the seismic for every well.

Based on this analysis, I reject well 9 which has an anomalously high RMS error. Figure 60 illustrates the quality of the seismic inversion results. In this case, the

correlation factor between the synthetic and the measured seismic is approximately 0.85 with an error coefficient ranging from 0.4 to 0.5.

Figure 61 shows the distribution of the wells with the best correlation, for P- and S-impedance for the 4° - 20° inversion. For both impedances, relatively low correlation is obtained on the wells located to the southwestern part of the seismic area.

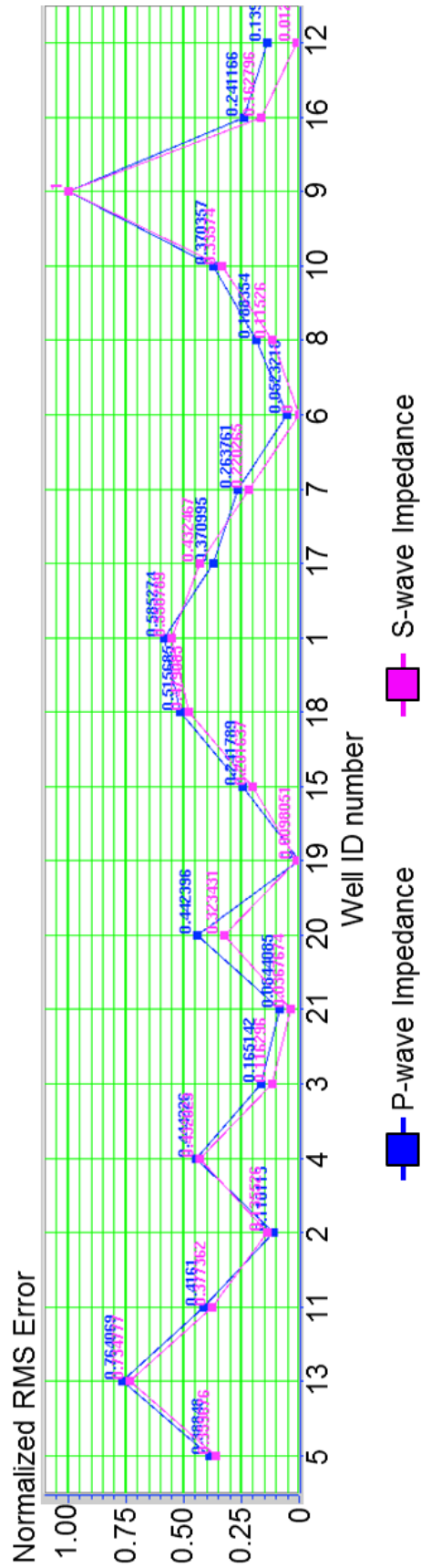


Figure 59. Normalized error between the inverted and the well-calculated P-wave and S-wave impedances.

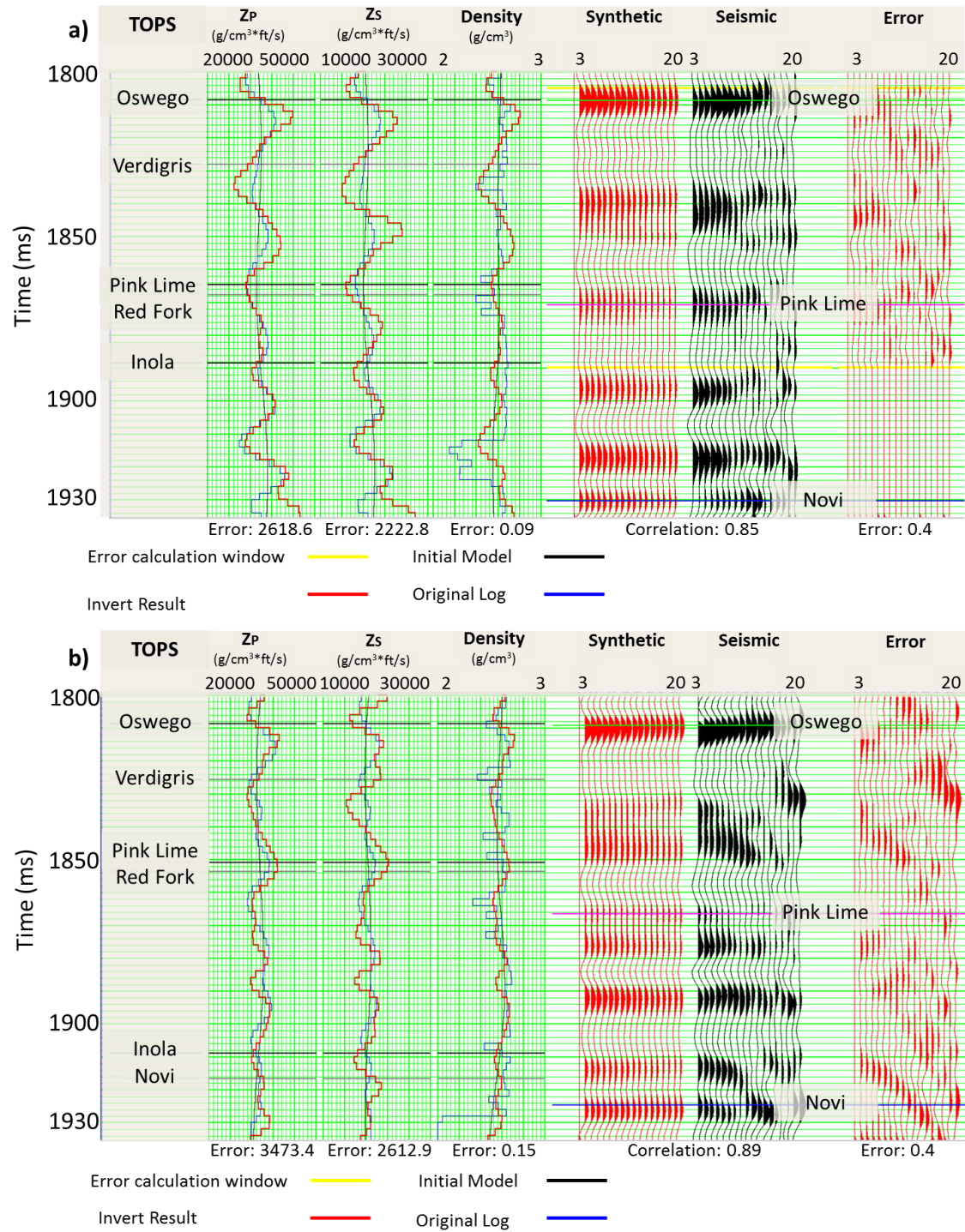


Figure 60. Validation analysis of P- and S- impedance, density and the comparison of the original seismic and the inverted result using a wavelet from the 4°-20° seismic inversion for (a) well 5 and (b) well 21.

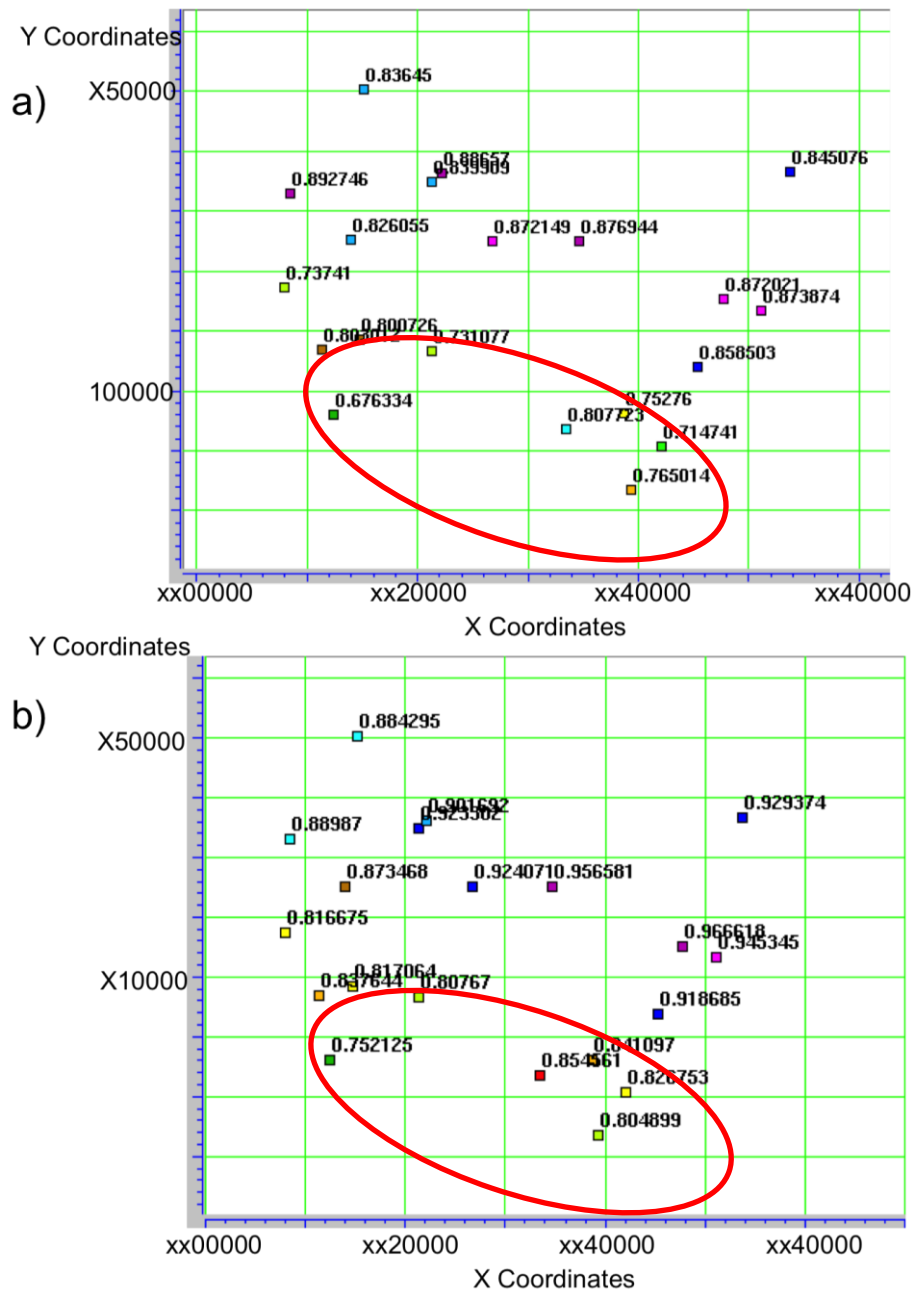


Figure 61. Seismic inversion correlation base map for offset range 4-20 degrees (top) and 5-27 degrees (bottom). Note that wells with lower correlation are located in southwestern part of the seismic area (red oval).

As part of the validation of the accuracy of the inverted results, the P- and S-impedance computed with original well logs and inverted results at the 20 wells were cross-plotted (Figure 62).

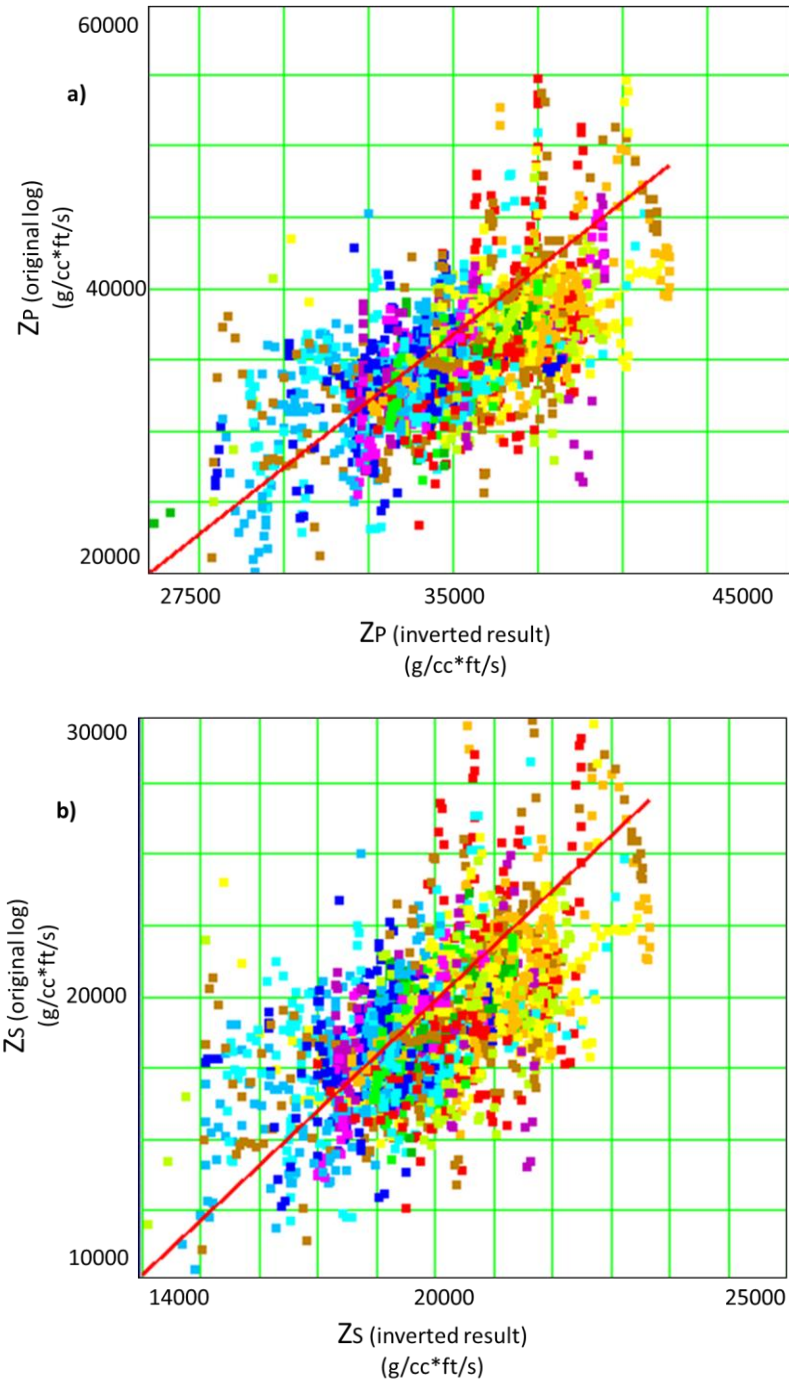


Figure 62. Crossplot of seismic inverted impedance against the estimated impedance from logs. (a) P-wave and (b) S-wave.

Linear relationships for P- impedance and S-impedance from the inverted result and the original well data regression, were computed to provide a correction factor to adjust the inversion to more closely match the well data:

$$Y_{(P-impedance\ from\ well)} = a * X_{(P-impedance\ inverted)} + b , \quad (6)$$

where $a = 1.86627$ and $b = -28522.9$, and

$$Y_{(S-impedance\ from\ well)} = a * X_{(S-impedance\ inverted)} + b , \quad (7)$$

where $a = 1.92186$ and $b = -16631.5$.

A well not used in the seismic inversion or “blind well”, is used to verify the seismic impedance inversion results (Figures 64-67). In this specific case, well 14 was not included in any analysis and well 9 was dismissed based on the high error coefficient obtained during the exploratory data analysis step prior to the simultaneous seismic inversion. Note the good correlation between the P- and S-impedance calculated from the well and the inverted result from the seismic data.(Figures 65 and 66).

Figures 67 and 68 illustrate a phantom horizon slice through the P-and S- impedance volumes. In these figures the major incised valley fill system is highlighted by arrows.

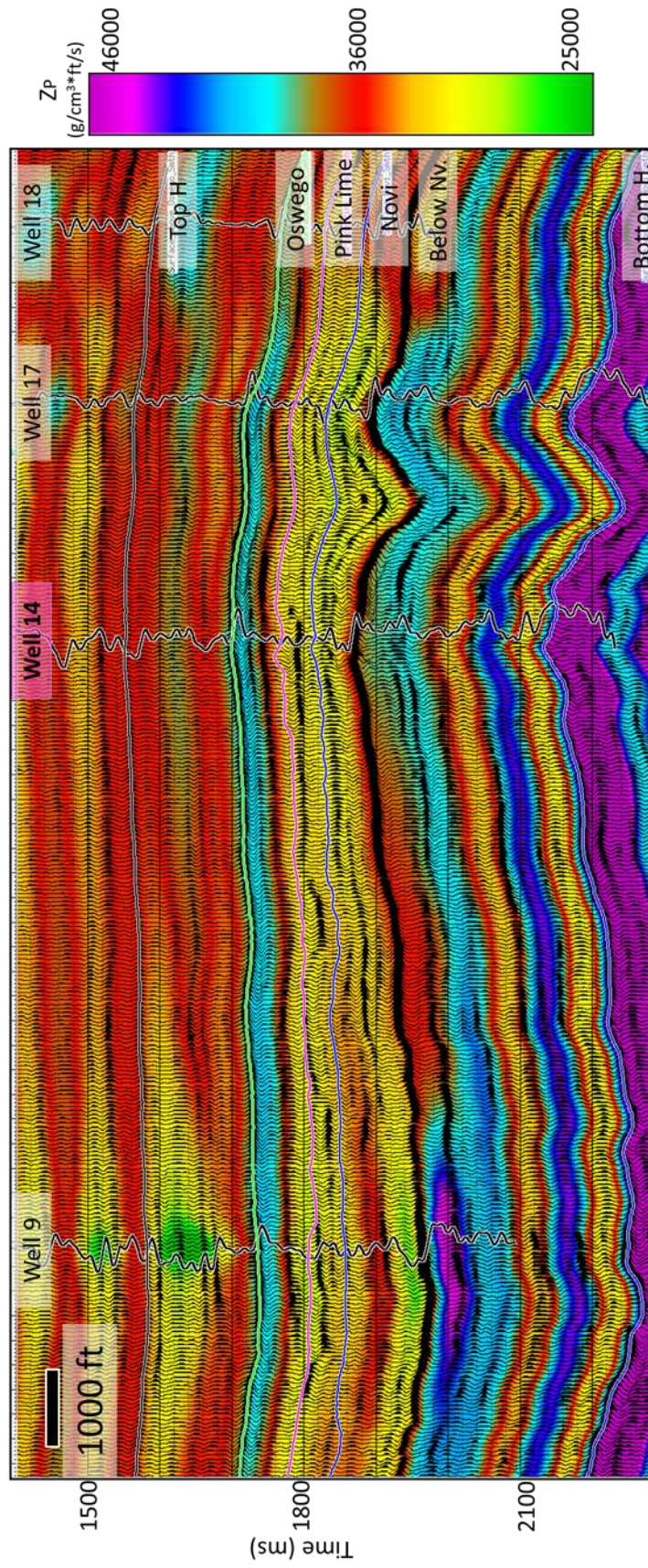


Figure 63. P-impedance low frequency model used in the simultaneous seismic inversion. Note that well 14 (blind test) was not used in the seismic inversion.

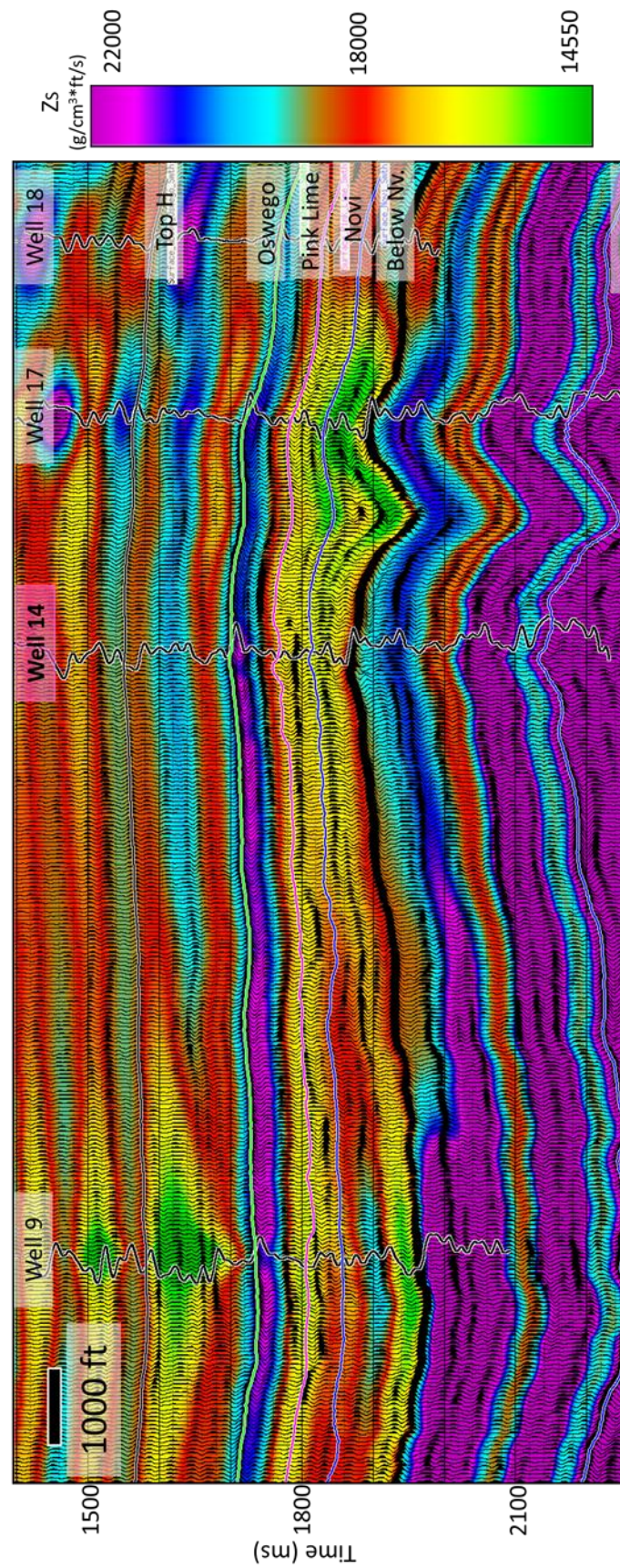


Figure 64. S-impedance low frequency model used in the seismic inversion. Note that well 14 (blind well) was not used in the simultaneous seismic inversion.

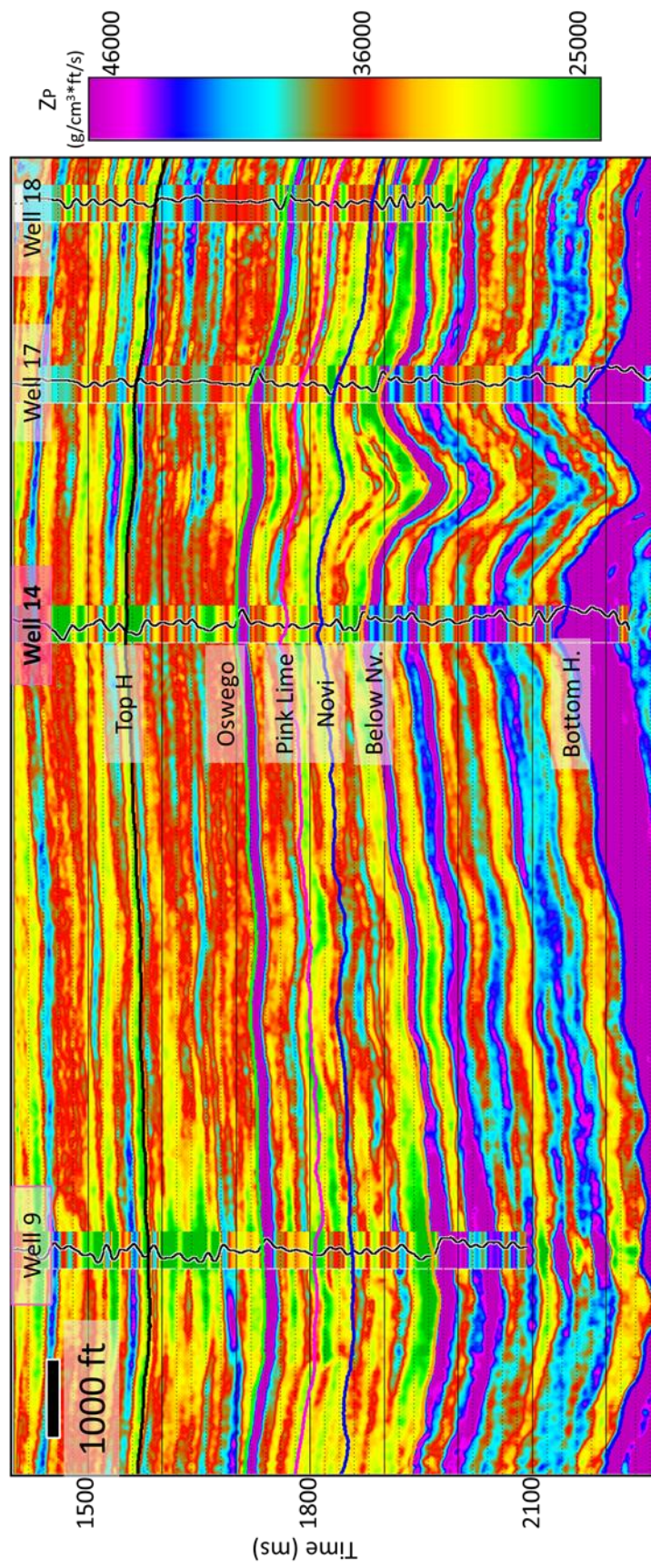


Figure 65. P-impedance arbitrary seismic vertical line. Well 14 was not used in the inversion. Note the good correlation in the zone of interest between Oswego and Novi Formations.

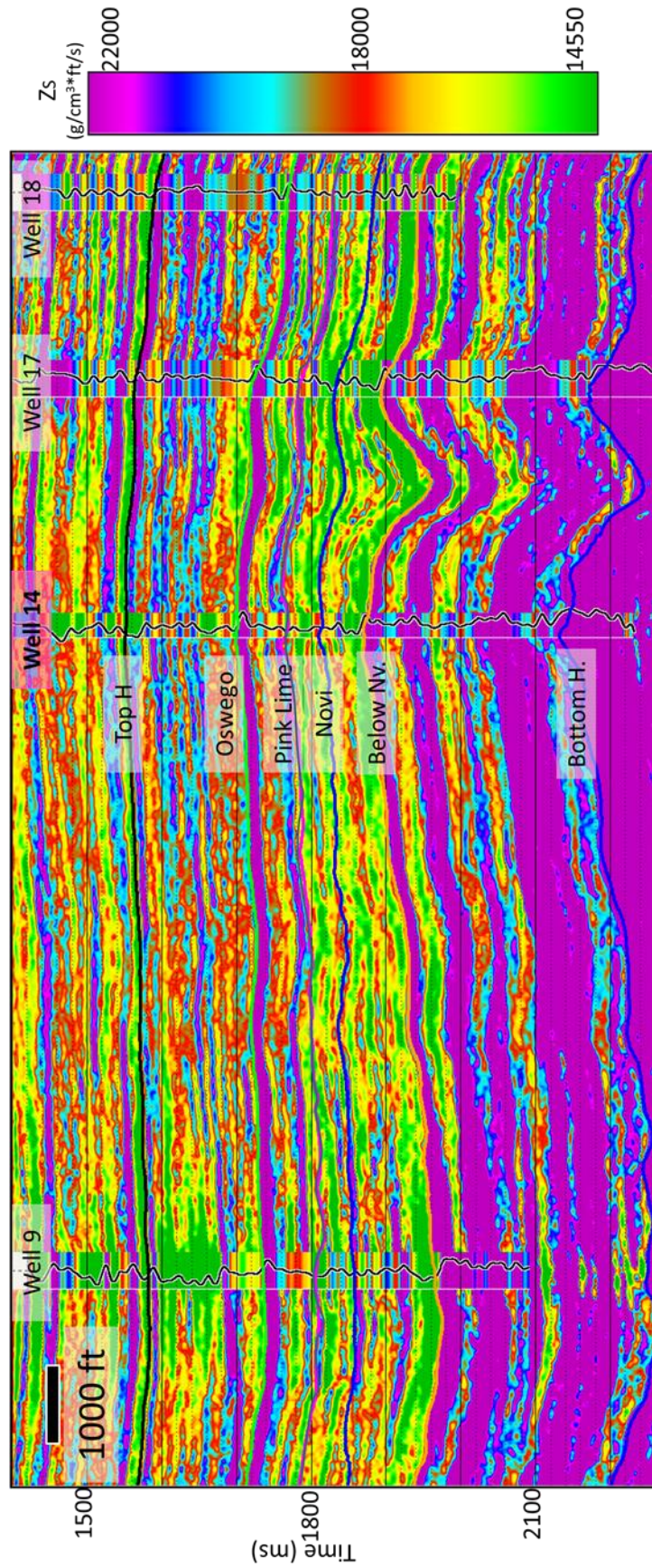


Figure 66. S-impedance arbitrary seismic vertical line. Well 14 was not used in the inversion. Note the good correlation in the zone of interest between Oswego and Novi Formations.

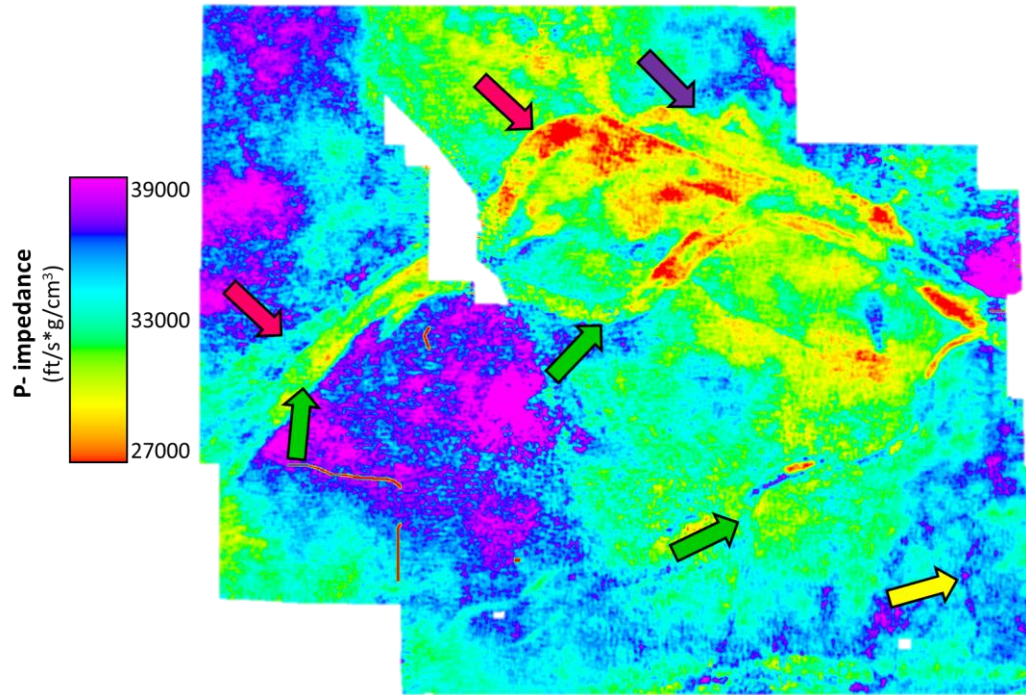


Figure 67. Phantom horizon slice 80ms below Oswego through the P-impedance volume. Magenta arrows indicate stage III and green arrows show stage V, both merging in the west part of the seismic survey.

Purple arrow indicates incised channels of Stage II. Yellow arrow indicates stage VI which has a northeast-southwest direction. Note better delineation of the channel features compared to S-impedance.

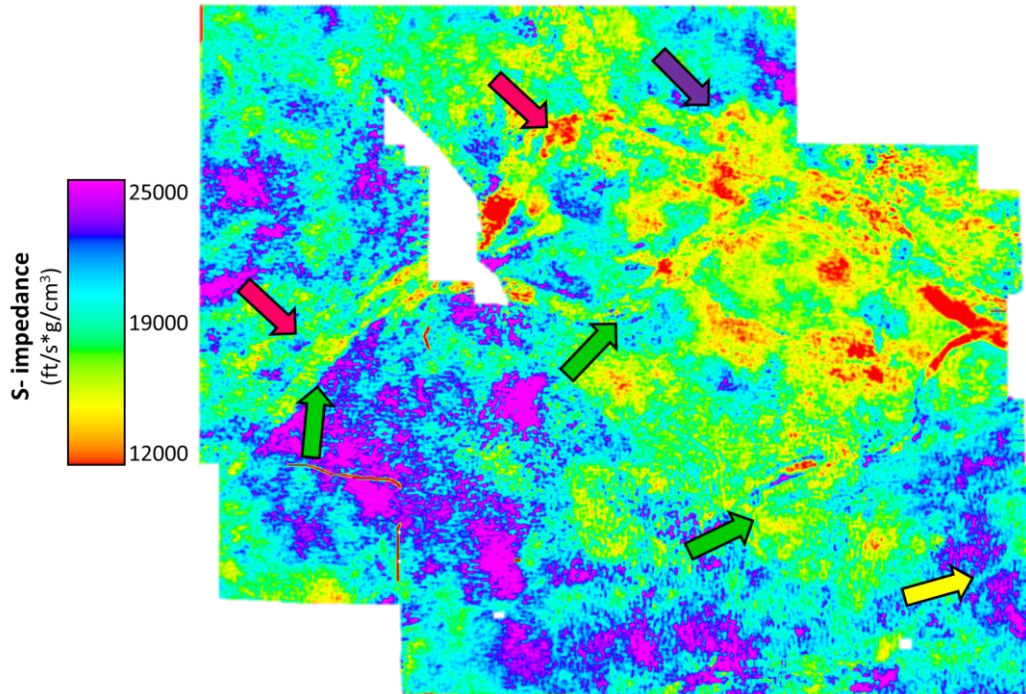


Figure 68. Phantom horizon slice 80ms below Oswego through the S-impedance volume. Magenta arrows indicate stage III and green arrows show stage V, both merging in the west part of the seismic survey.

Purple arrow indicates incised channels of Stage II. Yellow arrow indicates stage VI which has a northeast-southwest direction.

CHAPTER VI

GEOLOGICAL INTERPRETATION

The Red Fork incised valley fill stages were described in chapter II using the definitions of Withrow (1968) and Peyton et al. (1998). In this chapter, I will redefine these stages in terms of Clement's (1991) and Davogustto et al.'s (2012) geophysical analysis.

Clement (1991) describes the Red Fork valley system as having three stages of deposition. Stage I consists of basal lag structures and low sinuosity channels with very low width/depth ratio, moderate relief on the basal scour surface and steep banks. This stage eroded part of the Middle and Lower members of the Red Fork (Figure 69a). Stage II is characteristic of laterally variable, confined meander belt sequences, which gave rise to amalgamated point bar, clay plug and overbank deposits. The meander belts have a moderate width/depth ratio and moderate to high relief on basal scour surfaces (Figure 69b). Stage III is characterized by active downcutting channels through poorly consolidated older valley fill. The channels have a low width/depth ratio and exhibit similar characteristics to Stage I. The sand found in this stage is reworked and redistributed by marine-tidal processes during transgression (Figure 69c).

Davogustto et. al. (2012) interpreted five stages based on the definitions of Clement (1991). He found that by applying phase residues to the seismic data, these stages could also be defined on the seismic data volume. Figure 70 illustrates a vertical seismic line with the interpretation of the channel base. Davogustto et al. (2012) found that Stage I

and IV are invisible on the seismic data but not on the well logs (Appendix E). The remaining stages are visible on the seismic data.

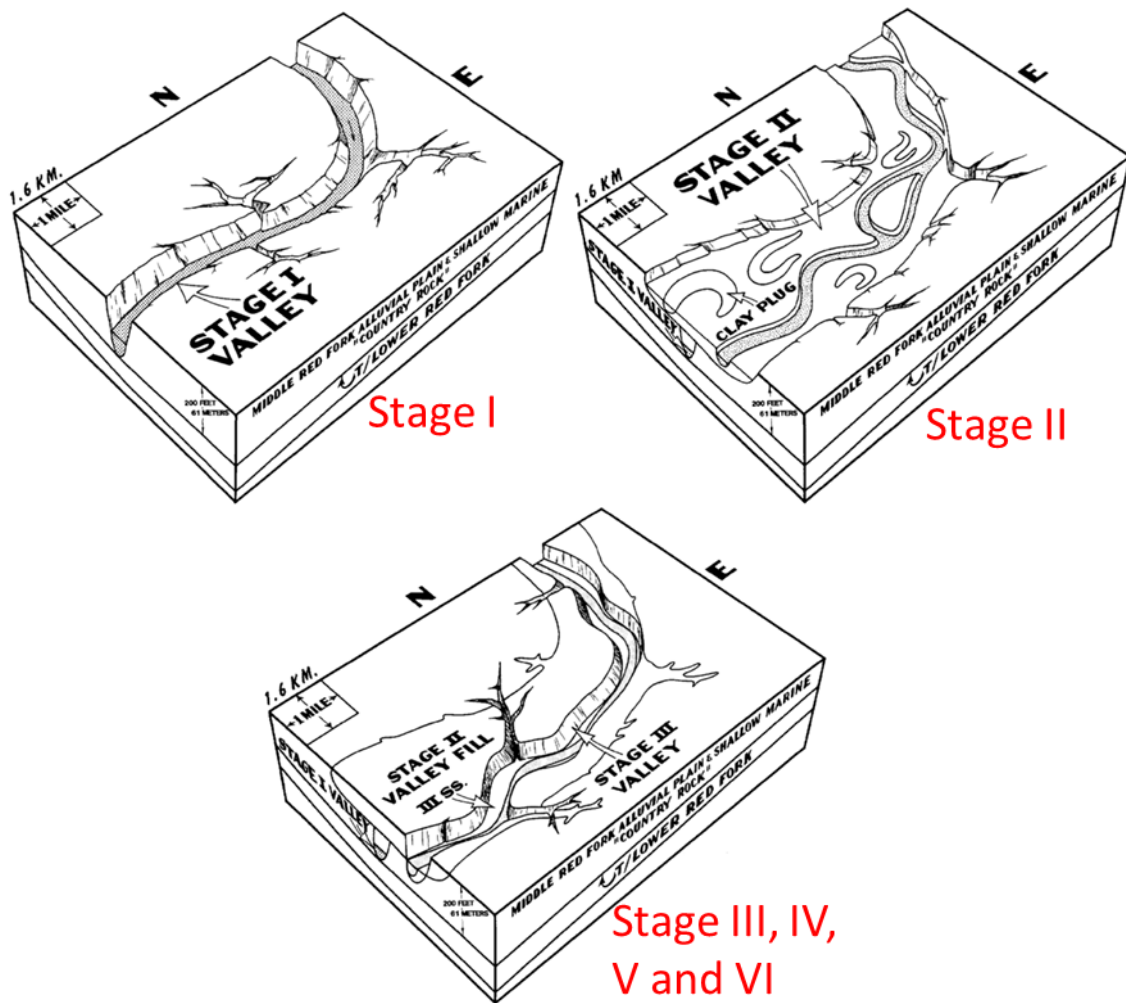


Figure 69. Block diagram illustrating the evolution of the Red Fork valley system by stages. (a) Stage I, (b) Stage II and (c) Stage III (After Clement, 1991). Stages defined in this project are represented in the model by red.

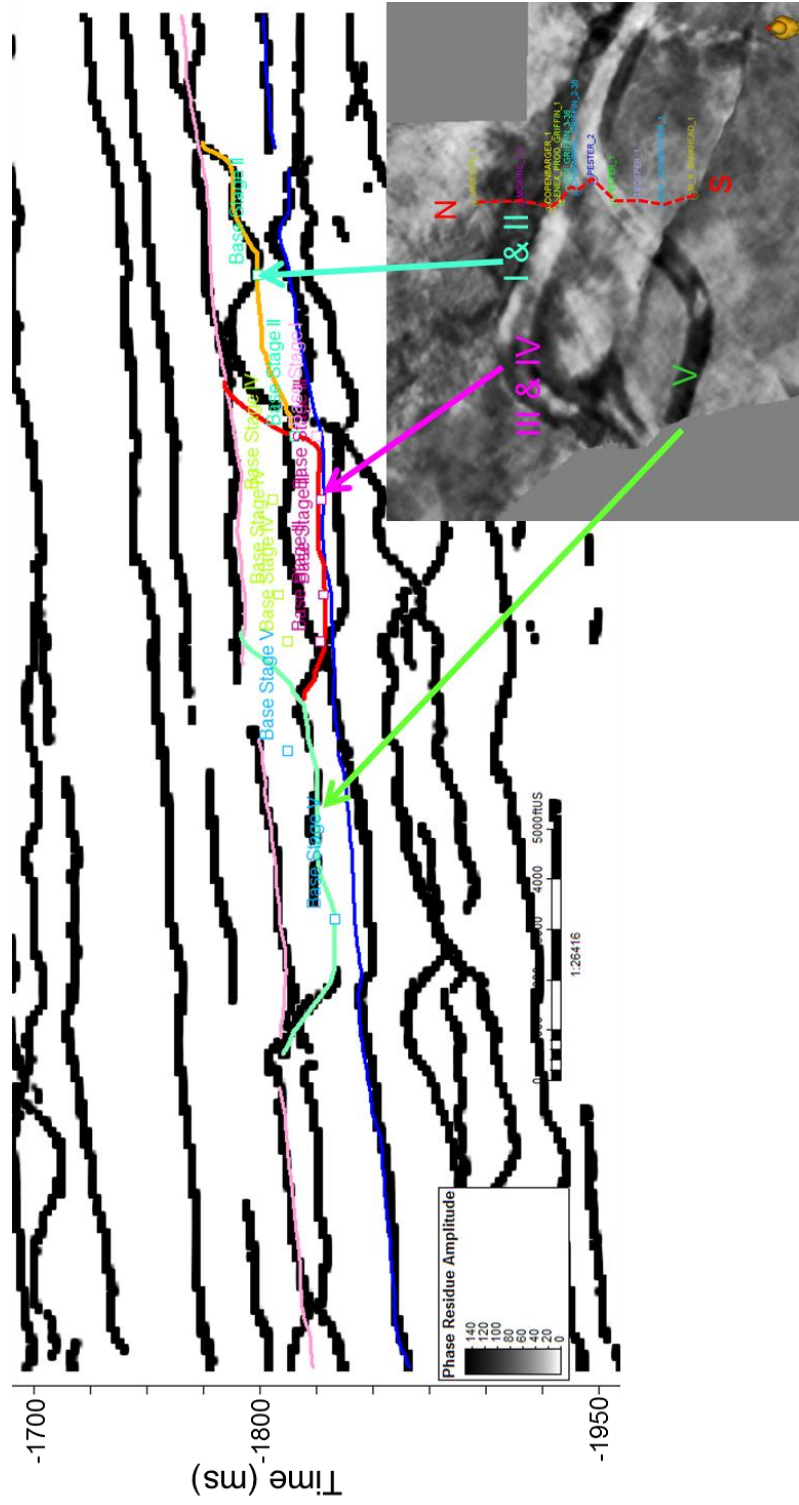


Figure 70. Seismic vertical line illustrating the distribution of the Red Fork main incised valley fill stages. Note that the N-S dash red line in the base map is a cross-section displayed in Figure 70 (Modified from Davogustto et al. 2012).

According to Slatt (2006) and Mayall and Stewart (2000), the degree of sinuosity is inversely proportional to the slope gradient, with high sinuosity associated with fine-grained and lower-energy channel fill, and low sinuosity associated with coarse-grained and higher-energy channel fill. Figure 71 illustrates the vertical variation within one depositional sequence. This sequence varies from more areally widespread erosional basal lag deposits to smaller aggradational channels with near prominent levees. This vertical stacking pattern can be expected in the Red Fork Formation where the NE-SW depositional axis steps landward while changes in sea level alter the energy, grain size and volume of the flows. However, the Red Fork is more structurally complex. Sea level changes were more abrupt and orogenic activity influenced the deposition of this geologic formation as seen in Figure 3.

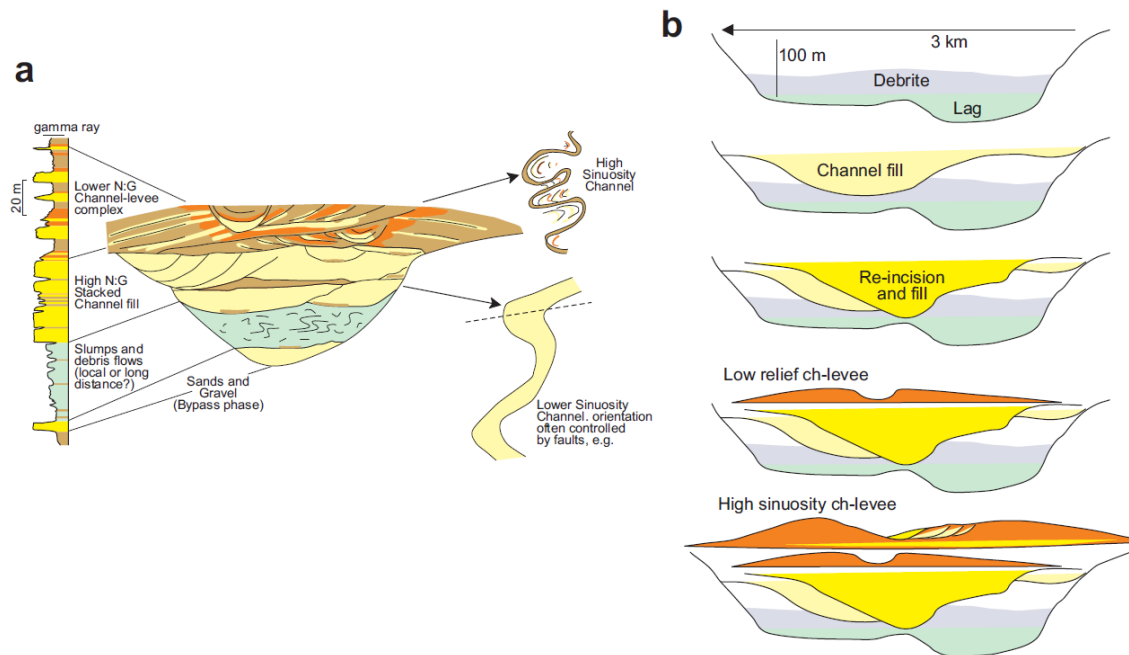


Figure 71. Schematic cross sections illustrating variations in channel fill in an erosionally confined area. (a) Sequential development of channel-fill facies. At the base, a large erosional surface is overlain by thin sand rich lag deposit, which is overlain by shale-rich debrite and then by thick, high net: gross amalgamated channel-fill deposits, which are overlain by low net: gross leveed-channel deposits. Inset figures show (left) an interpreted gamma-ray log through the deposits, and (right) plan view of the shape of the channels (higher sinuosity = channel-levee; lower sinuosity = sand-rich channel fill). (b) Repeated erosion and fill is a common feature in channels. Older channel-fill sediments are preserved as erosional remnants in younger channels (After Mayall and Stewart (2000)).

Based on concepts from Clement (1991), Davogustto et. al. (2012), Mayall and Stewart (2000), and Slatt (2006), I interpret the Upper Red Fork Formation to be divided into six valley fill stages. Stage I eroded part of the Lower and Middle Red Fork; its base cannot be seen on the seismic data. This stage consists mainly of a basal lag deposit of sand and shales. Stage II has high sinuosity channels and was deposited on top of Stage I; its response can be clearly seen on seismic data; Figure 72a shows how seismic attributes delineate small channels features. This stage had some dormant small channels that were reactivated during either late Stage III or early Stage IV. Stage III consists of sand deposits and eroded most of Stage II (Figure 73b). This stage crosses the entire seismic survey from East to West and in its maximum sinusoidal curve, I observed a splay that has a particularly straight shape, which could be a seismic

artifact. This splay is then eroded in some areas by the reactivated Stage II small channels (Figure 73c). Stage IV cannot be seen in seismic and according to Withrow et al. (1968) contains erosions of older sediments and shows possible transgressions in sea level. Stage V contains low impedance sands and shales and deeply erodes all the previous stages. In the southern part of the seismic survey Stage V has high sinuosity (Figure 73d). Next to the southeastern part of Stage V, there is another sinuoidal channel that could either part of a late Stage V or a new Stage VI (Figure 73e).

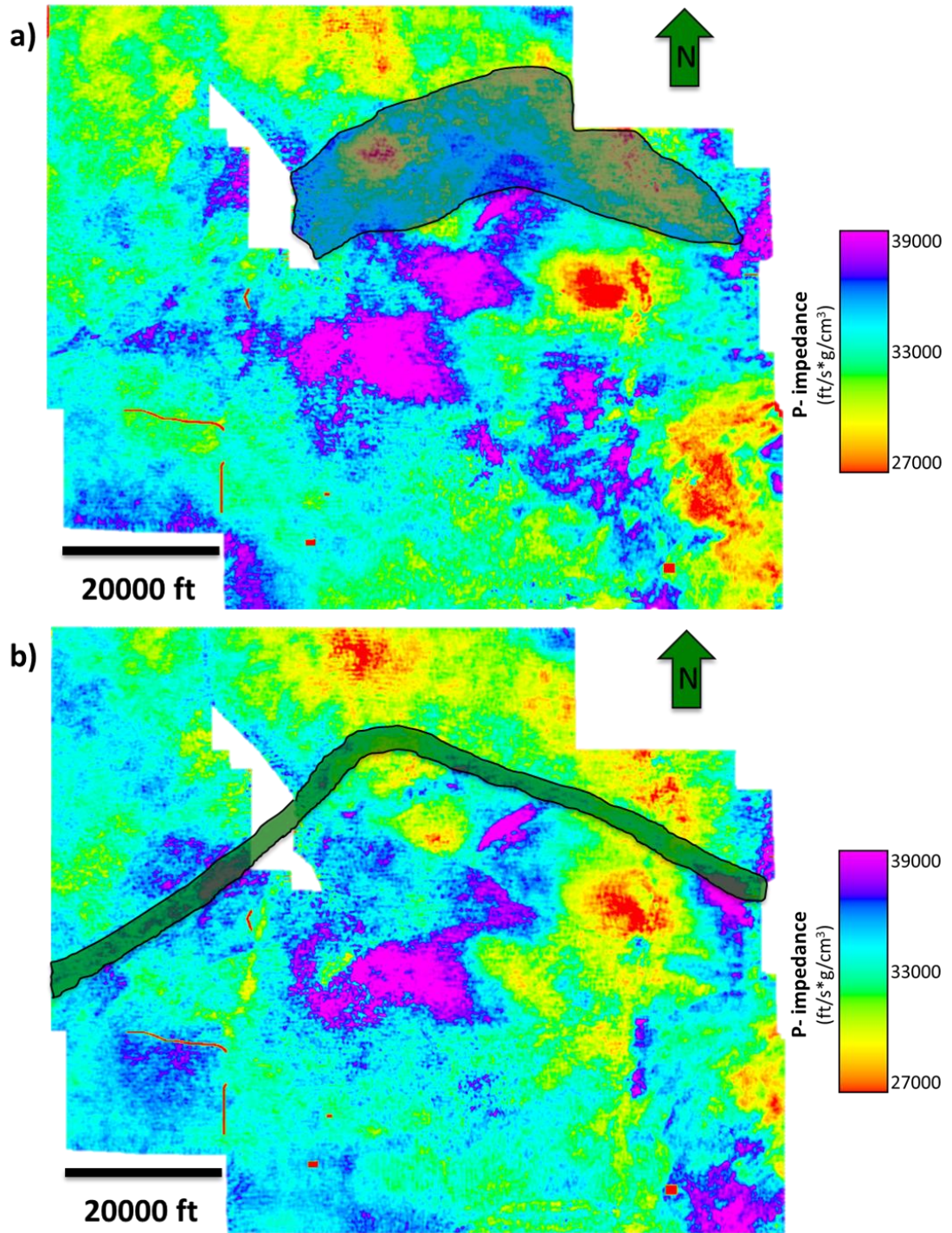


Figure 72. Phantom horizon slice 80ms below Oswego through the P-impedance volume on the mega merged survey (a) Interpretation of distribution of Stage I (not seen on seismic) and Stage II. (b) Deposition of Stage III.

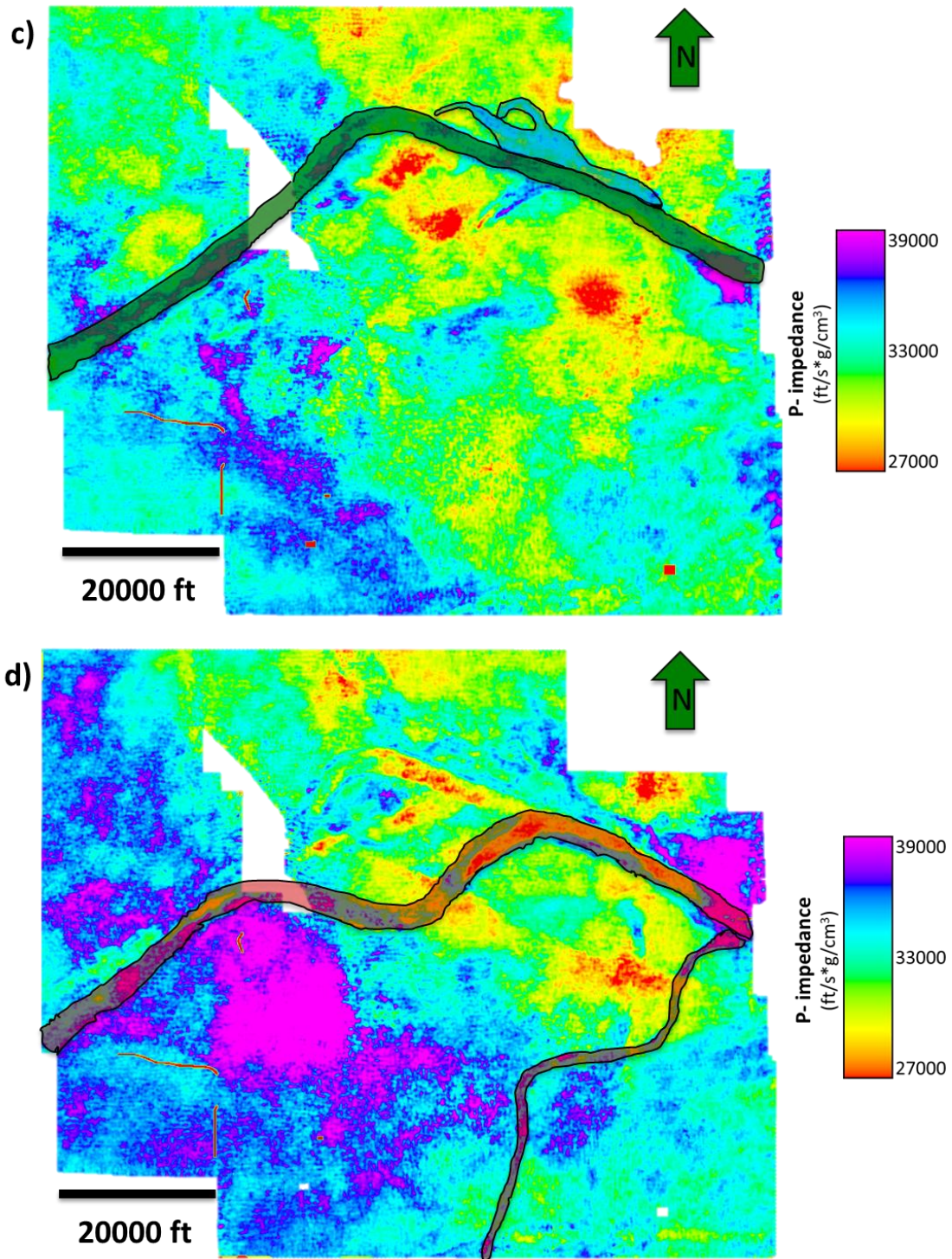


Figure 72. Phantom horizon slice 80ms below Oswego through the P-impedance volume on the mega merged survey (c) Deposition of late Stage III and reactivation of channels on Stage II (d) Deposition of Stage V.

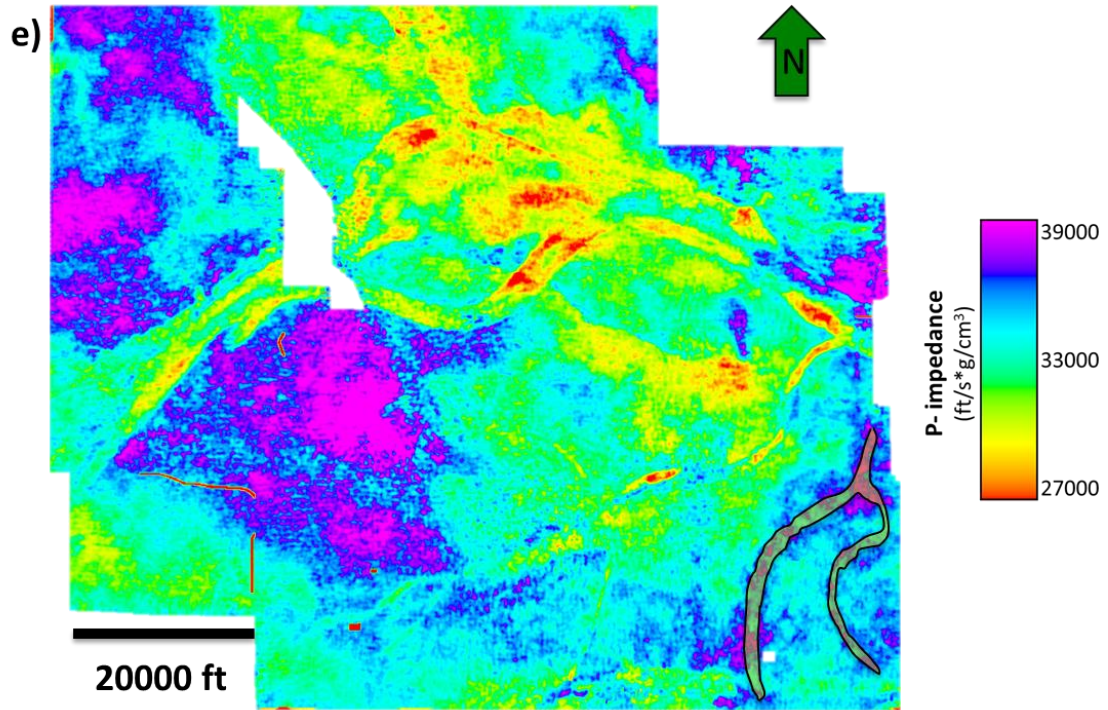


Figure 72. Phantom horizon slice 80ms below Oswego through the P-impedance volume on the mega merged survey (e) Deposition of Stage VI.

These stages can be easily seen in phantom horizons through flattened seismic volumes. In chapter III, it was demonstrated how differential compaction can be detected by using most-positive and most-negative curvature, which is due to the fact that when shales are deposited they contain greater porosity than the surrounding lithologies. With burial, these shales are more easily compacted than the older already partially compacted matrix, giving rise to a deformed surface which can be measured by curvature (Chopra and Marfurt, 2010).

The cartoon in Figure 73 illustrates how the curvature and coherence attributes illuminate channel structures. Most-positive and most-negative principal curvature were used in this study, since they are directly linked to anticlinal and synclinal morphology, and thereby they highlight the effects of differential compaction over a channel feature (Figure 75) (Chopra and Marfurt, 2010).

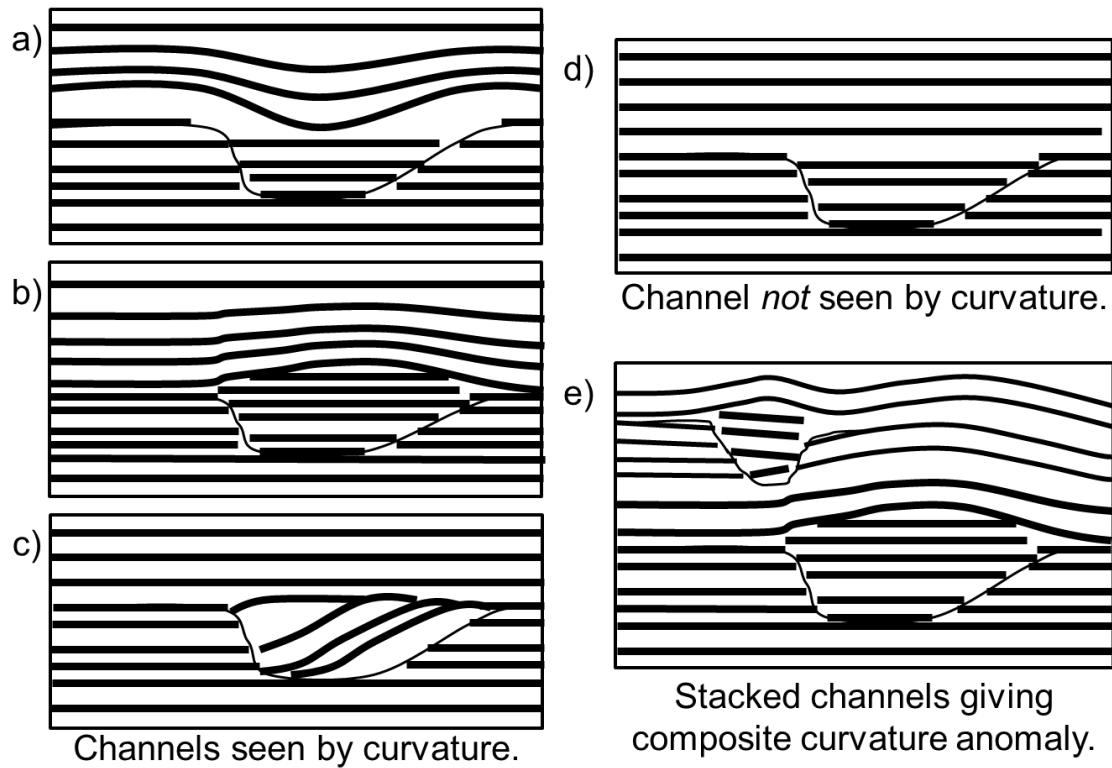


Figure 73. Response of seismic attributes to a channel feature. Channels that have differential compaction (a and b) or aggradational features (c) generally will be seen by curvature. However, because volumetric curvature calculations are performed on time slices rather than on picked horizons, channels that have little differential compaction or internal dip, such as (d), experience no lateral change in dip and thus will not be seen by curvature. Finally, stacking of channel complexes can result in stacking of differential compaction, requiring flattening on a deeper reference horizon before computing curvature (e). (After Chopra and Marfurt, 2010).

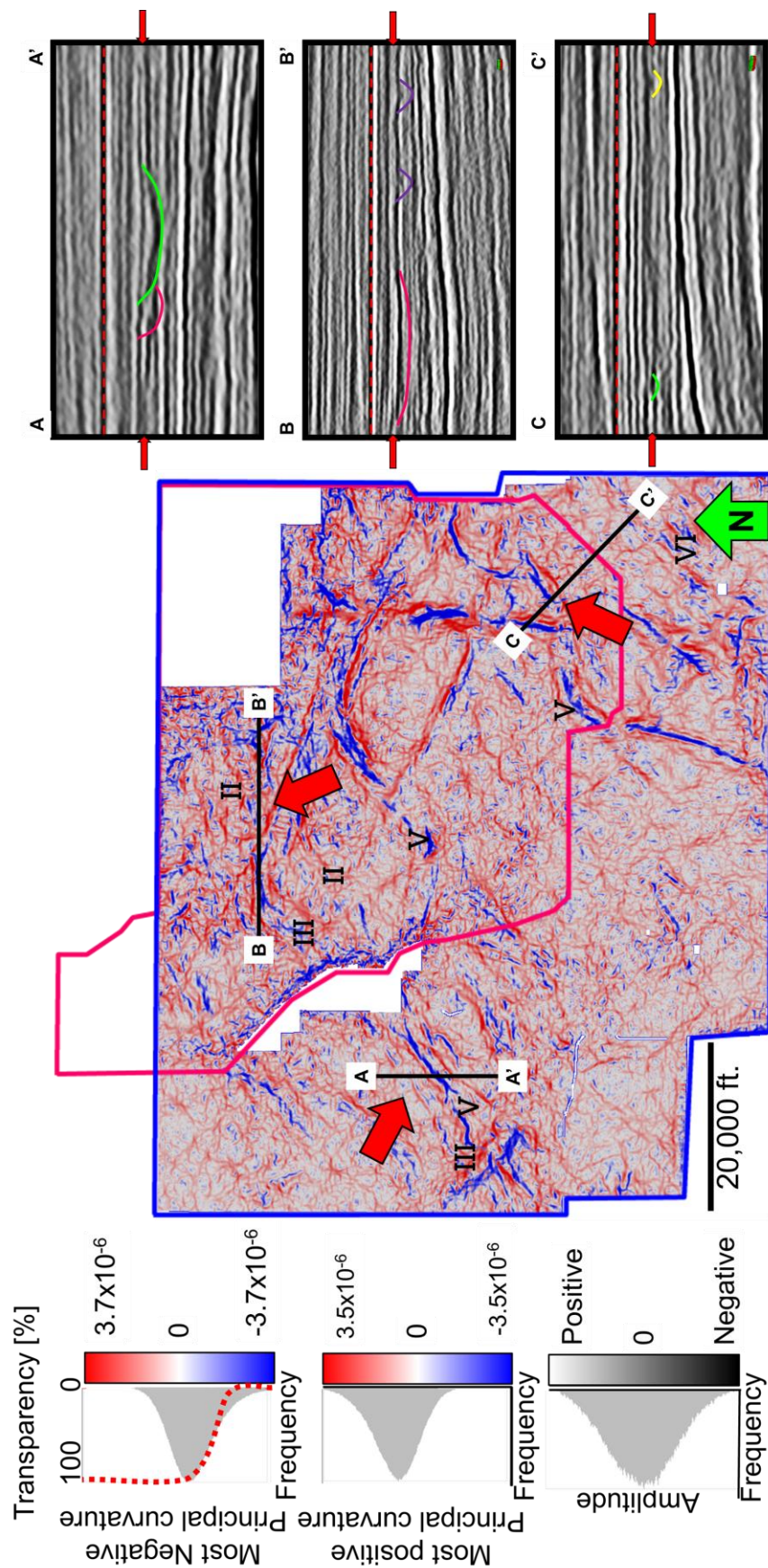


Figure 74. Phantom horizon slice 66 ms below Oswego through the most-positive curvature co-rendered with the most-negative curvature volume on the mega merged survey. A-A' vertical slice shows the western part of Stage V eroding Stage III. B-B' vertical slice shows the reactivated small channels of Stage II. C-C' vertical slice shows southern part of Stage V and Stage VI/V.

CHAPTER VII

CONCLUSIONS

The quality of the seismic attributes is highly correlated to the signal-noise ratio of the data. Seismic attributes can be strongly affected by the acquisition footprint, which masks the appearance of channel features. Careful reprocessing of legacy data can have a huge impact on both lateral and vertical resolution, as well as attribute response.

AVO analysis has proven to be an insufficient technique to discriminate lithologies in the Paleozoic rocks of the Red Fork Fm. Simultaneous prestack seismic inversion is a technique that goes beyond AVO analysis, integrating the well log information to estimate a seismic wavelet and generate a background model. Seismic data need to be properly conditioned and well tops have to be accurate and tied to the seismic in order to have a valid result.

Simultaneous prestack impedance and spectral decomposition help to characterize channel morphology and discriminate lithologies. My work show low impedance values correspond to high porosity sandier intervals while high impedance values correspond to low porosity shale or limestone rich intervals. 3D seismic attributes show good consistency when interpreting incised valley fill channels in the Red Fork Formation.

REFERENCES

- Aki, K., and P.G. Richards, 1980. Quantitative seismology: Theory and methods, Freeman and Co., New York.
- Bailey R., Jr., and F.J. Adler, 1983, Permo-Carboniferous hydrocarbon accumulations, Mid-Continent, U.S.A.: AAPG Bulletin, **67**, 979-1001.
- Barber, R., 2010, Attribute delineation of karst and channels: calibration via acoustic impedance: MS thesis, The University of Oklahoma.
- Blakey, R., 2011, Regional Paleogeography, <http://www2.nau.edu/rcb7/nam.html>, accessed June 15, 2012.
- Burrus, R. C., and J. R. Hatch, 1989, Geochemistry of oils and hydrocarbon source rocks, greater Anadarko basin; evidence for multiple sources of oils and long-distance oil migration: Oklahoma Geological Survey Circular, **90**, 53-64.
- Castagna, J.P., and S.W. Smith, 1994, Comparison of AVO indicators: A modeling study. Geophysics, **59**, 1849-1855.
- Castagna, J. P., H. S. Swan, D. L. Foster, and C. A. Peddy, 1998, Framework for AVO gradient and intercept interpretation: Geophysics, **63**, 948-956.
- Chopra, S., and K. J. Marfurt, 2007, Seismic attributes for prospect identification and reservoir characterization: Society of Exploration Geophysicists.
- Chopra, S., and K. J. Marfurt, 2010, Seismic curvature attributes for mapping faults/fractures, and other stratigraphic features, CSEG Recorder, 39, 37-41.
- Chopra, S., and K. J. Marfurt, 2010, Integration of coherence and volumetric curvatures images: The Leading Edge, **29**, 1092–1107.
- Clement, W., 1991, East Clinton Field-U.S.A. Anadarko Basin, Oklahoma: AAPG Special Volumes, **TR**: Stratigraphic Traps II, 207-267.
- Davogustto, O., C. Cabarcas, M. Falk, A. Warner, and K.J. Marfurt, 2012, Detecting stratigraphic discontinuities using phase residues: The Watonga field example: GSOC continuing education seminar.

- Foster, D.J., R.G. Keys, and D. Lane, 2010, Interpretation of AVO anomalies: *Geophysics*, **75**, 75A3-75A13.
- Goodway, B., T. Chen, and J. Downton, 1997, Improved AVO fluid detection and lithology discrimination using Lamé petrophysical parameters; $\lambda\rho$, $\mu\rho$ and λ/μ fluid stack from P and S inversions: CSEG National Convention Expanded Abstracts, 148-151.
- Hampson, D., B. Russell, and B. Bankhead, 2005, Simultaneous inversion of pre-stack seismic data: 75th Annual International Meeting, SEG, Expanded Abstracts, 1633-1638.
- Henry, M.E., and T.C. Hester, 1995, Anadarko Basin Province: In D. L. Gautier, G.L. Dolton, K.I. Takahashi, and K.L. Varnes, 1995, National assessment of United States oil and gas resources--Results, methodology, and supporting data: U.S. Geological Survey Digital Data Series DDS-30, Release 2, on CD-ROM.
- Johnson, K. S., 1989, Geologic evolution of the Anadarko Basin: Kenneth S. Johnson (ed), Anadarko Basin Symposium: Oklahoma Geological Survey, Norman, **90**, 3-12.
- Laughlin, K., P. Garossino, and G. Partyka, 2003, Spectral Decomposition for Seismic Stratigraphic Patterns, Search and Discovery, <http://www.searchanddiscovery.com/documents/geophysical/2003/laughlin/images/laughlin.pdf>, accessed March 30, 2012.
- Lavine, S.A., 1984, Provenance and diagenesis of the Cherokee sandstones, deep Anadarko basin, western Oklahoma: *Shale Shaker*, **34**, 120-144.
- Mai, H. T., K. J. Marfurt, and S. Chávez-Pérez, 2009, Coherence and volumetric curvatures and their spatial relationship to faults and folds, an example from Chicotepec basin, Mexico: 79th Annual International Meeting, SEG, Expanded Abstracts, 1063-1067.
- Mayall, M. and I. Stewart, 2000, The architecture of turbidite slope channels, in P. Weimer, R. M. Slatt, J. L. Coleman, N. Rosen, C. H. Nelson, A. H. Bouma, M.

- Styzen, and D. T. Lawrence, eds., Global Deep-Water Reservoirs: Gulf Coast Section-SEPM Bob F. Perkins 20th Annual Research Conference, p. 578-586.
- Michlik, D.M., 1984, Petrographic and mapping study of the subsurface "Oswego" Limestone in part of the Putnam Trend, T 15-16 N, R 15-17 W, Dewey and Custer counties, Oklahoma, in Hyne, N.J. (ed.), Limestones of the Mid-Continent: Tulsa Geological Society Special Publication, **2**, 327-346.
- Moore, G.E., 1979, Pennsylvanian paleogeography of the southern Midcontinent: In Hyne, N.J., ed., Pennsylvanian sandstones of the mid-continent: Tulsa Geological Society Special Publication no. 1, 2-12.
- Northcutt, R.A., and J.A. Campbell, 1988, Geologic provinces of Oklahoma: Oklahoma Geological Survey. http://www.faq.s.org/sec-filings/111201/North-Texas-Energy-Inc_S-1/ex99-1.htm#b, accessed March 4, 2012.
- Ostrander, W.J., 1984, "Plane-wave reflection coefficients for gas sands at non-normal incidence", *Geophysics*, **49**, 1637-1648.
- Peyton, L., R. Bottjer, and G. Partyka, 1998, Interpretation of incised valleys using new 3D seismic techniques: A case history using spectral decomposition and coherency: *The Leading Edge*, **17**, 1294-1298.
- Roberts, A., 2001, Curvature attributes and their application to 3D interpreted horizons. *First Break*, **19**, 85-99.
- Rutherford, S. R. and R. H. Williams, 1989, Amplitude versus offset variations in gas sands: *Geophysics*, **54**, 680-688.
- Slatt, R.M., 2006, Stratigraphic reservoir characterization for petroleum geologists, geophysicists, and engineers, **6**, 176-177.
- Schlumberger, 2009, Log Interpretation Charts.
- Schlumberger Oilfield Glossary, 2012, <http://www.glossary.oilfield.slb.com/MainIndex.cfm?ID=1>, accessed March 4, 2012.

- Schmoker, J.W., 1989, Thermal maturity of the Anadarko basin: In Johnson, K.S., ed., Anadarko Basin Symposium, 1988: Oklahoma Geological Survey Circular **90**, 25-31.
- Steeple, D. W., and L. Brosius, 1996, Earthquakes: Kansas Geological Survey http://www.kgs.ku.edu/Publications/pic3/pic3_1.html.
- Suarez, Y., K.J. Marfurt, and M. Falk, 2008, Seismic attribute-assisted interpretation of channel geometries and infill lithology: A case study of Anadarko Basin Red Fork channels, 78th Annual International Meeting, SEG, Expanded Abstracts, 1-4.
- Swisi, A., 2009, Post- and pre-stack attribute analysis and inversion of Blackfoot 3D seismic dataset: University of Saskatchewan Master thesis.
- Tolson, P., 1993, Depositional environments of the Red Fork Sandstones in Custer and Roger Mills Counties, Southwestern Oklahoma: AAPG Search and Discovery Article, **77**, 1577-1578.
- Wallet, B. C., M. Matos, J. T. Kwiatkowski, and Y. Suarez, 2009, Latent space modeling of seismic data: An overview: The Leading Edge, **28**, 1454–1459.
- Whiting, P.H., 1984, Depositional environment of Red Fork sandstones, deep Anadarko basin, western Oklahoma: Shale Shaker Digest **11**, 120-144.
- Withrow, P. C., 1968, Depositional environments of Pennsylvanian Red Fork Sandstone in northeastern Anadarko Basin, Oklahoma: AAPG Bulletin, **52**, 1638-1654.
- Young, R., and LoPiccolo, R., 2005, AVO analysis demystified: E&P, http://www.e-seis.com/white_papers/AVO%20Analysis%20Demystified.pdf, accessed March 30, 2012.

APPENDIX A: AVO SLOPE AND INTERCEPT

Zoeppritz computed the variation of reflected energy at an elastic boundary as a function of the incident angle of the seismic wave (Figure A1), which forms the basis of AVO analysis. Aki and Richards (1980) approximated these equations by assuming small variations of elastic parameters across the boundary between the top and bottom layer to obtain the reflection coefficient, R , as a function of incident angle, θ :

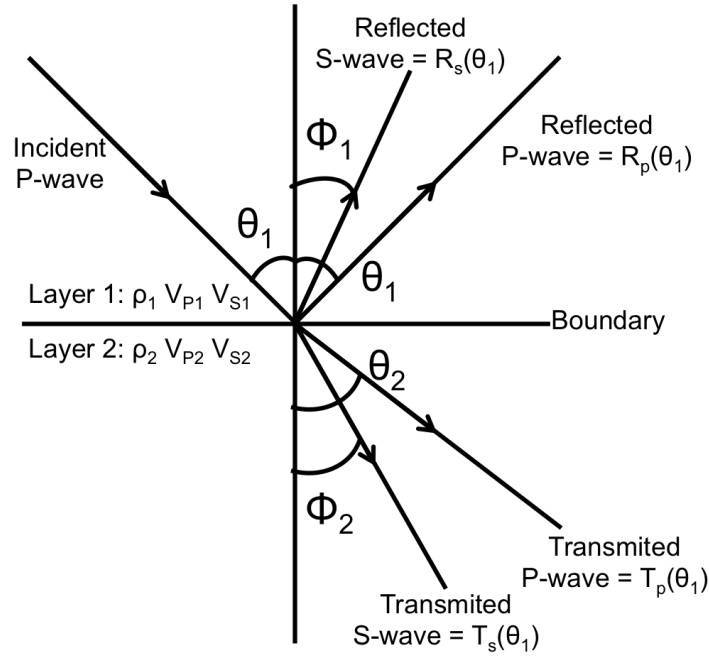


Figure A1. Cartoon of an incident wave that is reflected, refracted and converted into other waves when going through a boundary between two layers with different rock properties (ρ , V_P , V_S).

$$R(\theta) = a \frac{\Delta V_P}{V_P} + b \frac{\Delta V_S}{V_S} + c \frac{\Delta \rho}{\rho}, \quad (\text{A.1})$$

where

$$a = \frac{1}{2 \cos^2 \theta}, \quad (\text{A.1.2})$$

$$b = 0.5 - \left(\frac{V_S}{V_P} \right)^2 \sin^2 \theta, \quad (\text{A.1.3})$$

and

$$c = 4 \left(\frac{V_S}{V_P} \right)^2 \sin^2 \theta. \quad (\text{A.1.4})$$

Authors such as Castagna et al. (1998) and others used these three parameters and associate them in terms of $\tan^2 \theta$ and $\sin^2 \theta$ to obtain a more linearized relationship between the amplitude and the offset:

$$R(\theta) = A + B \sin^2 \theta + C(\tan^2 \theta \sin^2 \theta), \quad (\text{A.2})$$

where

$$A = \frac{1}{2} \left[\frac{\Delta V_P}{V_P} + \frac{\Delta \rho}{\rho} \right], \quad (\text{A.2.1})$$

$$B = \frac{1}{2} \frac{\Delta V_P}{V_P} - 4 \left[\frac{V_S}{V_P} \right]^2 \frac{\Delta V_S}{V_S} - 2 \left[\frac{V_S}{V_S} \right]^2 \frac{\Delta \rho}{\rho}, \quad (\text{A.2.2})$$

$$C = \frac{1}{2} \frac{\Delta V_P}{V_P}, \quad (\text{A.2.3})$$

$$\Delta V_P = V_{P_2} - V_{P_1}, \quad (\text{A.2.4})$$

$$\Delta V_S = V_{S_2} - V_{S_1}, \quad (\text{A.2.5})$$

$$\Delta \rho = \rho_2 - \rho_1, \quad (\text{A.2.6})$$

$$V_P = \frac{V_{P_2} + V_{P_1}}{2}, \quad (\text{A.2.7})$$

$$V_S = \frac{V_{S_2} + V_{S_1}}{2}, \quad (\text{A.2.8})$$

and

$$\rho = \frac{\rho_2 + \rho_1}{2}. \quad (\text{A.2.9})$$

The first two terms of equation A.2 provide an approximately linear relation between the amplitude and the sine squared of the angle of incidence. A is called the intercept and B called the “AVO gradient”. C is called “the curvature factor” that barely affects the amplitude values at angles less than 30° . The slope and intercept terms are routinely used in the analysis of fluid effect in softer Tertiary rocks.

According to Swisi (2009) the intercept A and the gradient B , defined above, can be expressed as a function of time in the CMP gather. Figure A2 shows an example of amplitude increasing with offset.

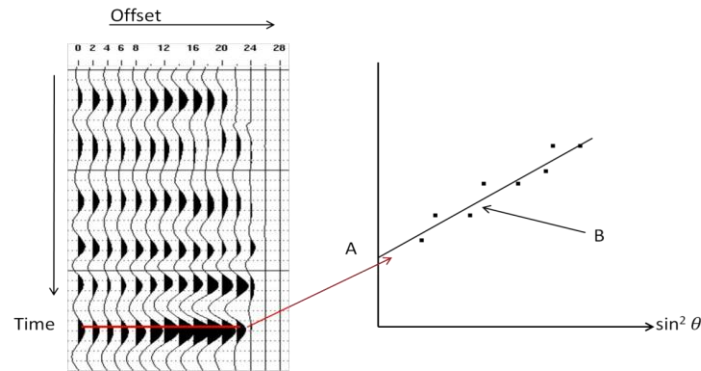


Figure A2. Example of a class III AVO gas sandstone amplitude increasing with offset. A and B are the intercept and slope of the amplitude when $R(\theta)$ is plotted against $\sin^2 \theta$ (After Swisi, 2009).

Rutherford and Williams (1989) cross-plotted the intercept A against gradient B , using a “background” trend or mudrock line with negative slope, they classified AVO into 3 different classes (Figure A3) while Castagna et al. (1998) added a forth:

- Class I: High-impedance contrast with decreasing reflection coefficient relative to increasing offset (A is positive and B is negative).

- Class II: Near-zero impedance with reflection coefficient increasing or decreasing with offset and probably polarity reversal (A is positive or negative and B is only negative);
- Class III: Zero-offset reflectivity that is increasing with offset. (A and B are both negative); and
- Class IV: Zero-offset reflectivity decreasing with offset, it is also considered to be a variation of Class III (A is positive and B is negative).

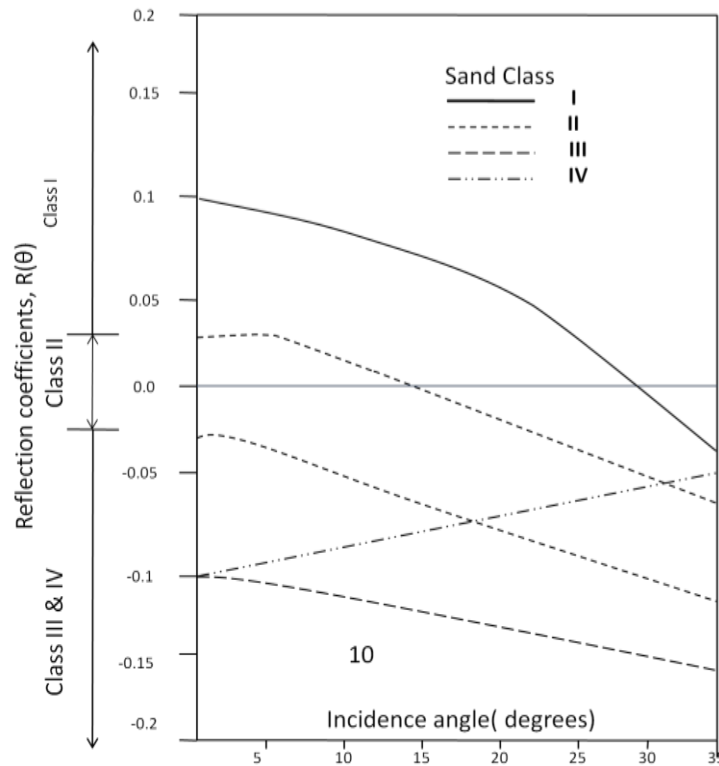


Figure A3. AVO classifications for the top of gas sands (After Castagna et al. 1998).

Goodway et al. (1997) found $\lambda\mu$ and $\mu\rho$ parameterization to be more useful than A and B in the analysis of more indurated Mesozoic and Paleozoic rocks.

Defining P- and S- wave velocities as:

$$V_P = \sqrt{\frac{\lambda+2\mu}{\rho}} \quad (\text{A.3})$$

$$V_S = \sqrt{\frac{2\mu}{\rho}} \quad (\text{A.4})$$

we have

$$\mu\rho = (V_S\rho)^2 = Z_S^2 \quad (\text{A.5})$$

$$(V_P\rho)^2 = (\lambda + 2\mu)\rho = Z_P^2 \quad (\text{A.6})$$

and therefore

$$\lambda\rho = Z_P^2 - 2Z_S^2 \quad (\text{A.7})$$

in which: λ =incompressibility (pore fluid dependant), and μ = rigidity (rock matrix dependant).

Goodway et al. (1997) cross plotted $\lambda\rho$ and $\mu\rho$ and found clean gas sands have low values of $\lambda\rho$ and high values of $\mu\rho$ (Figure A4). This observation will be used to interpret the results in this thesis in which lithology discrimination of the Red Fork Formation is the main objective.

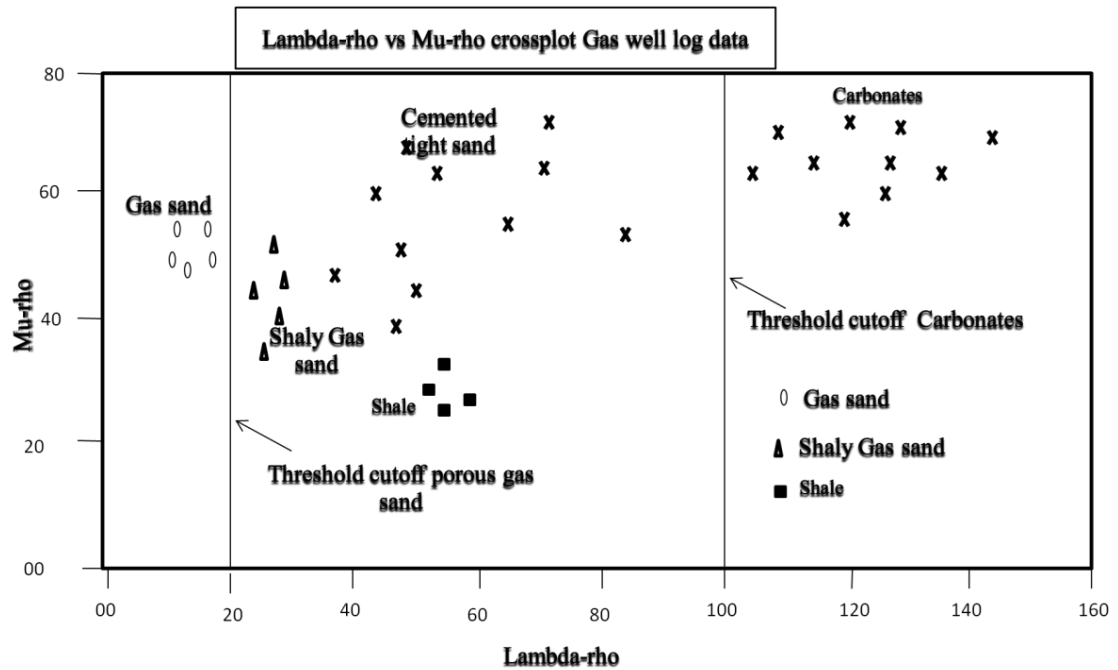


Figure A4. A $\lambda\rho$ and $\mu\rho$ cross plot of gas sand in Canada. Note that gas sands “breakout” as anomalously low values prediction of $\lambda\rho$ (After Goodway et al. 1997).

AVO analysis in the “mega-merged” survey and wells

In this project, AVO response was analyzed on well 9 and the seismic section around it to compare it with the seismic inversion results, obtaining a class IV response for the Pink Lime/ Red Fork shales/sands interface (Figure A6), which corresponds to shaly or sandy intervals with impedance contrast of Stage II of the valley fill system. The Class I response in Figure A5 is obtained in the interface shale/sand in the Red Fork Formation, which corresponds to low impedance contrast sands with high porosity. These results are not similar for well 19 in which a class IV AVO response was obtained for the Pink Lime/Red Fork interface but a class IV AVO response for the interface shale/sand in the Red Fork Formation.

AVO analysis of the mega merged survey to discriminate lithologies benefits from data up to 30°. Examining Figures A5 a-c show an acceptable fit up to 30°. While cross-plots indicate discrimination better between clastic and non-clastics lithologies, discrimination between sands from shales is not possible.

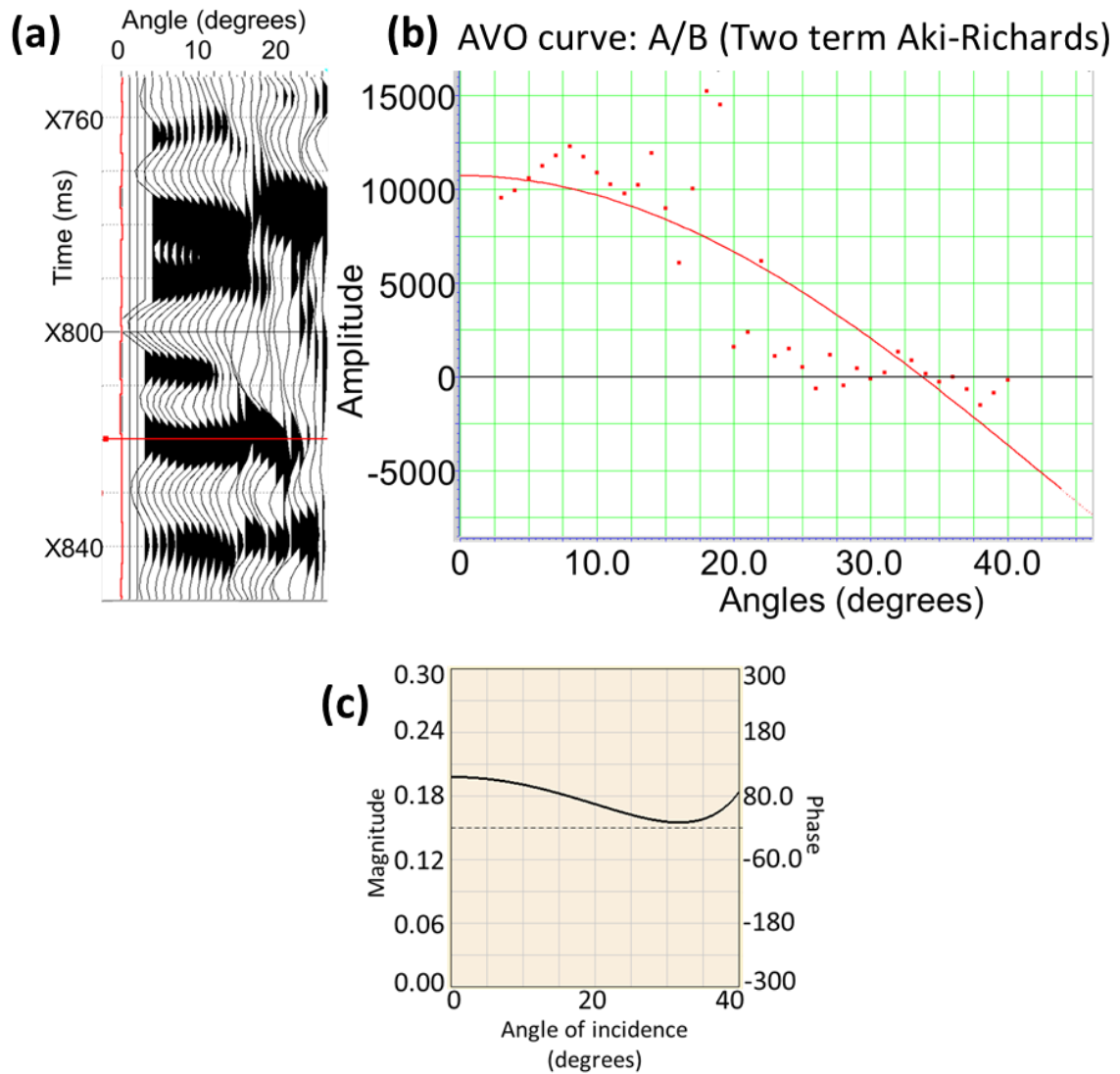


Figure A5. (a) Seismic gather and (b) AVO showing a class I response for the interface between Red Fork shales and sands. Location at the well 9 on base map Figure 46 (top). (c) AVO response computed from the well logs. Note that response differs at angles higher than 30°.

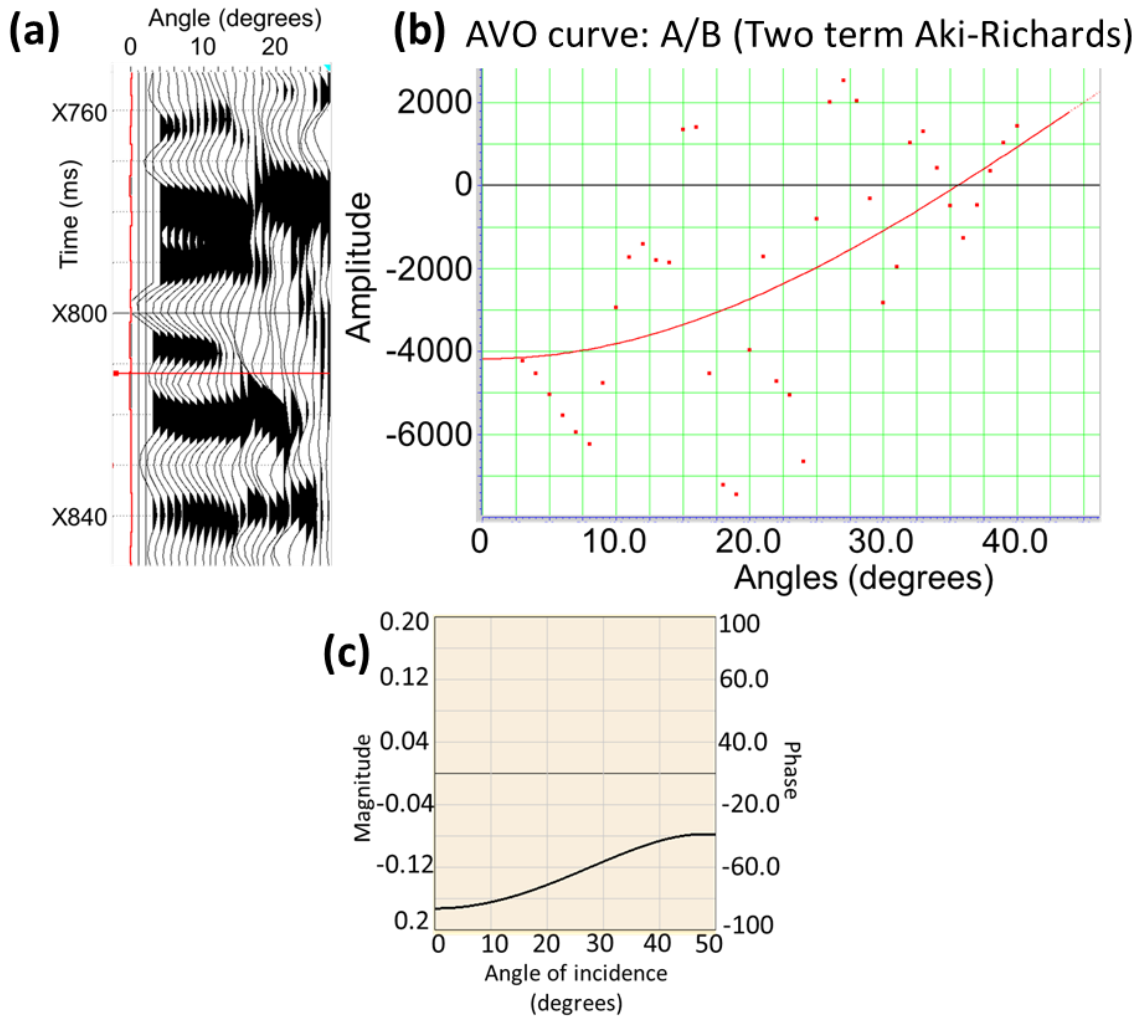


Figure A6. (a) Seismic gather and (b) AVO showing a class II response for the interface between Red Fork shales and sands. Location at the well 9 on base map Figure 46 (top). (c) AVO response computed from the well logs.

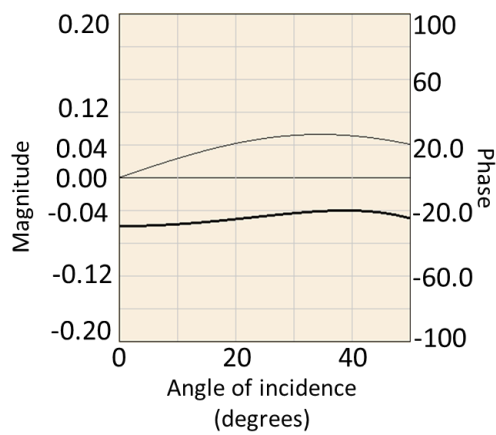


Figure A7. AVO response showing a class IV response for the interface between Red Fork shales and sands. Location at the well 19 on base map Figure 46 (top). Note that for the same interface in well 9 a class I response was obtained.

APPENDIX B: PREVIOUS WORK

Despite the large amount of drilled wells in the Anadarko Basin, subtle petrophysical differences of the productive wells from seismic data is still uncertain due to complex geometry and distribution of the incised valley fill of the Red Fork Formation. Barber (2010) evaluated the Red Fork Formation by comparing the rock properties of a productive and non-productive well to estimate an empirical relationship to differentiate sand from shale-filled channels about 50 miles away from my study area. She attempted to discriminate between high impedance tight sands and shales and lower impedance producing sands. Such separation was not possible on the post-stack data she had to work with.

Barber then modeled the pre-stack response with the objective of justifying the increased cost and expense of careful AVO-friendly processing and pre-stack inversion for future studies. The Red Fork Formation is stiffer (high effective Bulk modulus) and more rigid (high shear modulus) than the adjacent shale layers. By cross-plotting Z_P and Z_S for tight and porous sandstones, the Pink Lime and the Red Fork shales, she showed that partial lithology discrimination could be achieved (Figure B 1).

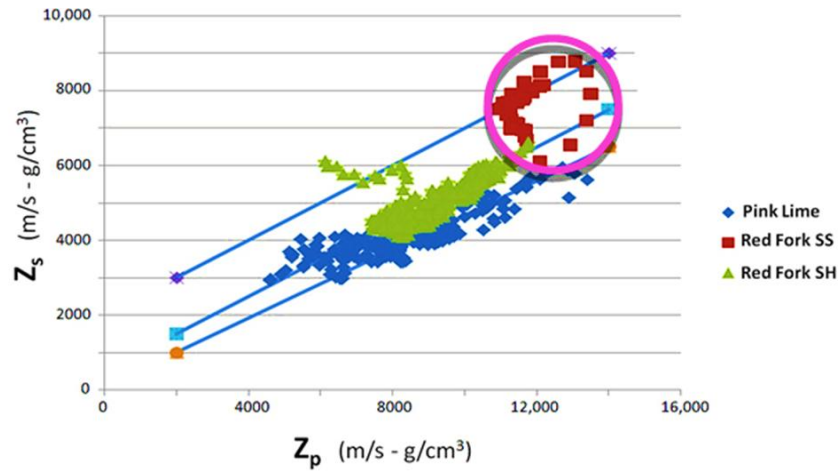


Figure B 1. P- and S-wave impedance for the Red Fork shale directly below the channel and the Pink Lime above it. The channel sands have values of Z_p and Z_s that fall within the magenta circle (After Barber, 2010).

Barber (2010) also found that Greenberg and Castagna (1992) equations better approximated the exact Zoeppritz solution for the Red Fork rocks than the Rutherford and Williams (1989) (Figure B 2).

Barber's (2010) AVO analysis for producing and non-producing Red Fork sands indicated a shallow class III AVO response for the producing sands, with the greatest reflectivity observed at far offsets (30° - 45°) for both Pink Lime and Red Fork shale overburden (Figure B 2)

At near and far offsets in the producing well, the reflectivity doesn't vary significantly and discrimination between the interface Pink Lime/Red Fork sand and Red Fork shale/ Red Fork sand is neglectable. This well exhibits a class III AVO. On the other hand, the non-producing well, which exhibits a class I AVO, has a significant difference between both interfaces at near and far offsets. Therefore it was proposed in her project to analyze near stack volumes due the limited fidelity of land seismic data.

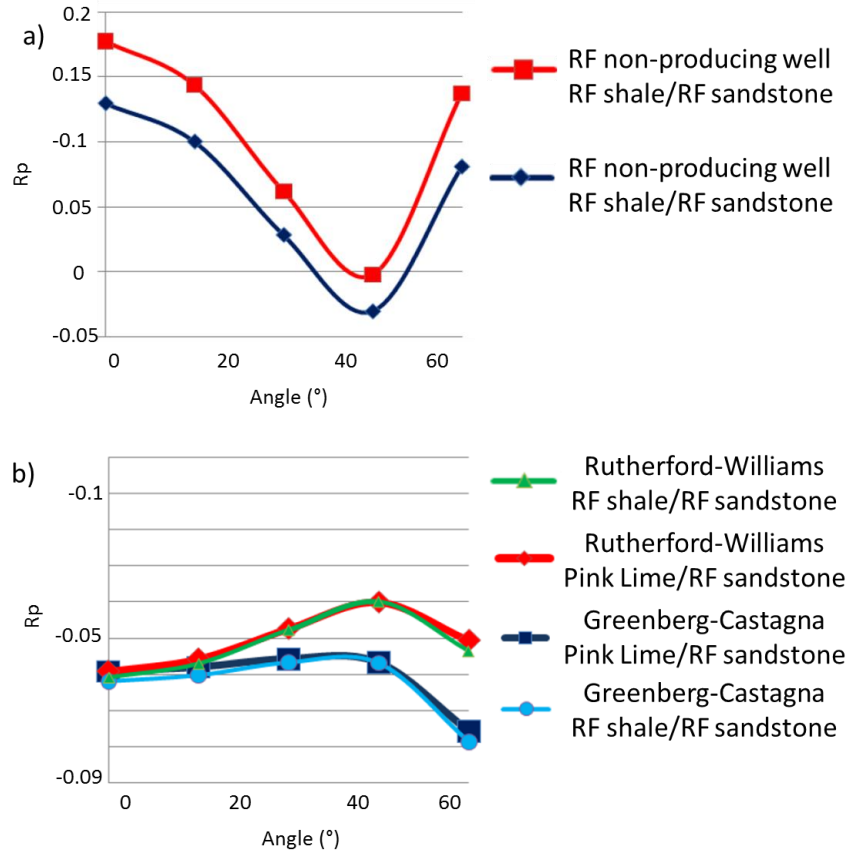


Figure B 2. Reflectivity vs. angle offset cross-plots for a producing and non-producing well. a) Non-producing Red Fork sands exhibit a class I AVO response with the strongest reflection coefficient at near offsets ($\leq 15^\circ$). b) Producing sands display a class III AVO response with highest reflection coefficient at far offsets (30° - 45°) using the Rutherford and Williams (1989) and Greenberg and Castagna (1998) approximations (After Barber 2010)

Foster et al. (2010) also showed the application of AVO for lithology discrimination in reservoirs characterized by hard rocks and low porosity in which the fluid effect is insignificant. Specifically, they examined thick sands in a main channel feeding a turbidite fan with porosities decreasing as the sediments become more distal from the source.

Foster et al. (2010) found class II anomalies associated with lower porosity sands and class III anomalies with higher porosity sands. In Figure B3a the cross-plot of slope vs. intercept for commercial well A, indicates a class III AVO. Figure B3b for non-commercial, lower porosity well B, indicates a class II AVO response.

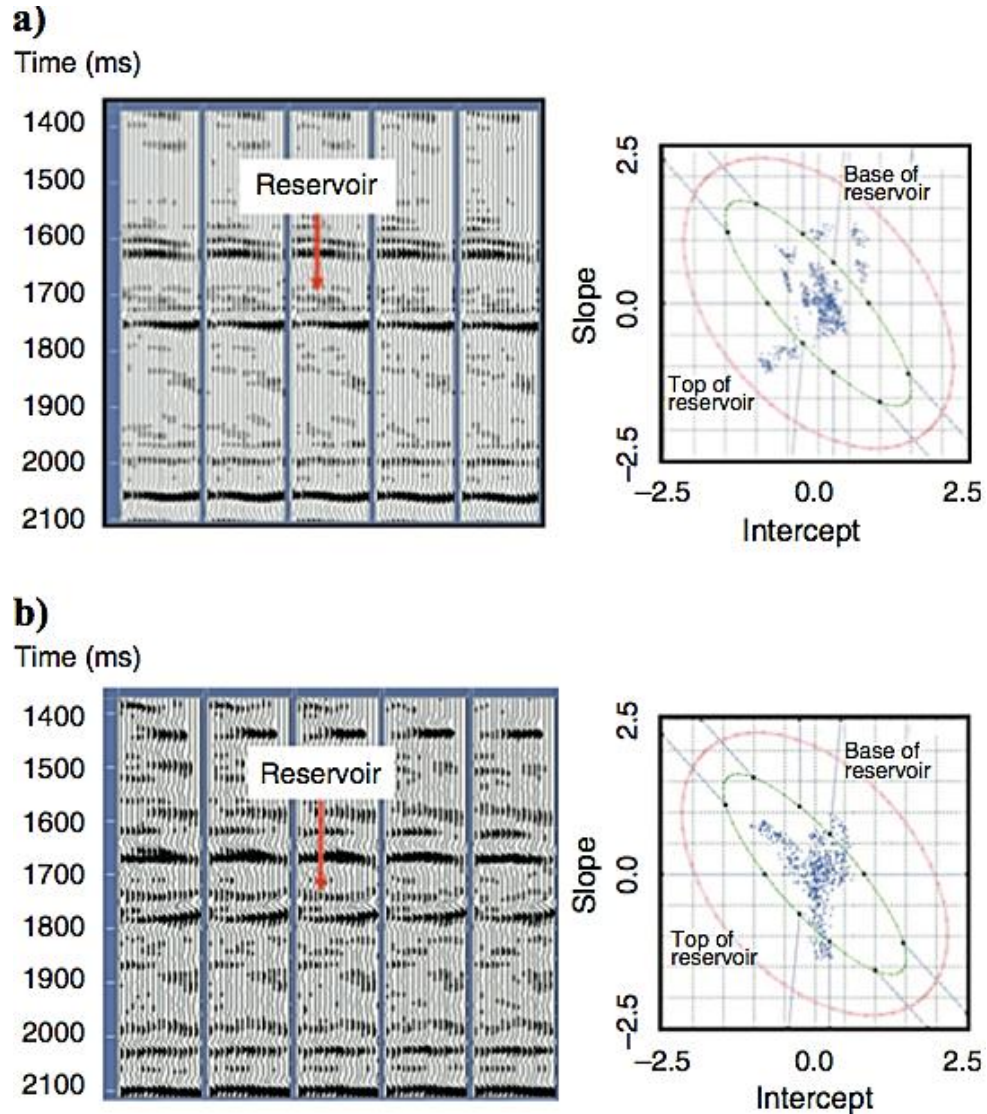


Figure B3. Gathers and resulting cross-plots around (a) Commercial higher porosity well A with class III AVO response and (b) Non-commercial lower porosity well B with class II AVO in the reservoir interval (After Foster et al., 2010).

A map view of the AVO response is shown in Figure B4 in which only the clean sands are mapped from the top of reservoir. Red and yellow colors represent a class III anomaly while blue denote a class II anomaly. Well A had penetrated the reservoir and encounters sands with good porosity ranges, while well B found sands with lower values of porosity. This map shows the preferential trend of distribution for the sands studied in the cross-plots of Figure B3.

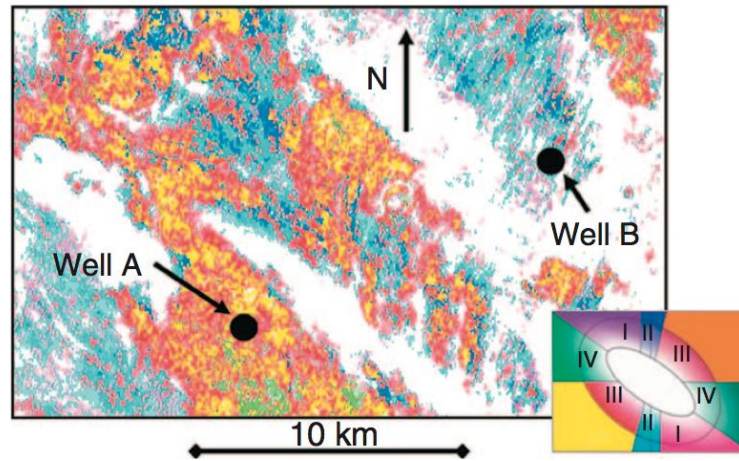


Figure B4. Amplitude extraction along the top reservoir reflection from the AVO classification volume. Higher porosity well A shows a relatively strong class III anomaly, while lower porosity well B shows a class II anomaly. The porosity in well A is higher than the porosity in well B. Note that the plot to the left corner is the color scale used in the map view of the reflection at the top of the reservoir (After Foster et al., 2010).

APPENDIX C: NEURAL NETWORK ANALYSIS

In chapter IV facies discrimination was performed on well logs, but discriminating between clastics and non-clastics is easier than discriminating between different clastics facies. Taking seismic inversion results and other 3D seismic attributes along with petrophysical parameters as input to supervised neural networks and multilinear regressions, it is possible to derive an effective porosity seismic volume that can be used to discriminate porous sandy intervals from non-porous zones shaly or lime intervals.

Effective porosity is defined as the interconnected pores that favor fluid flow. Supervised neural networks method uses as input seismic attributes that are correlated to well logs to come up with a relationship that is used to estimate effective porosity (Schlumberger Oilfield Glossary). The workflow used for porosity estimation with neural networks is shown in Figure C1. I used seven attributes to evaluate the validation error and correlation factor. Table 4 shows the validation training and validation error obtained for each input seismic attribute. Wells that had a very high validation error were excluded from the analysis and training.

Attribute	Train. Error	Valid Error
S-impedance	4.11	4.23
Vp/Vs	3.84	4.03
Spectral_Mag_44Hz	3.76	4.00
Spectral_Mag_24Hz	3.69	4.00
Spectral_Mag_14Hz	3.65	3.97
Coherent Energy	3.60	3.97
P-impedance	3.56	4.0

Table 4. Training and Validation error using a 7-sample convolution operator. Note that the validation error increases with P-impedance, therefore this attribute was not taken into the training of neural networks.

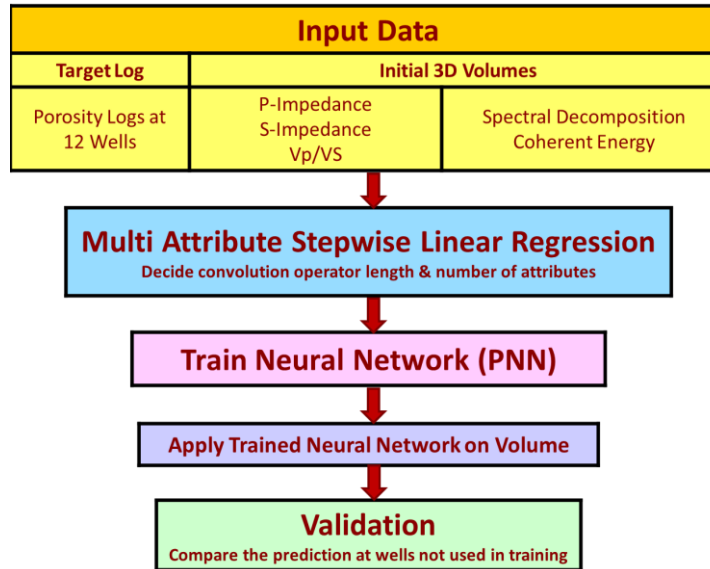


Figure C1. Workflow used to generate effective porosity and V_{sh} using supervised neural network method (After Verma et al., 2012).

The validation correlation during the neural network training was 40%, whereas the average correlation for average porosity prediction was approximately 60%. Figure C2 illustrates the quality validation of the neural training. Note that although the curves follow a similar trend, predicted porosity does not follow the exact details of the actual porosity log.

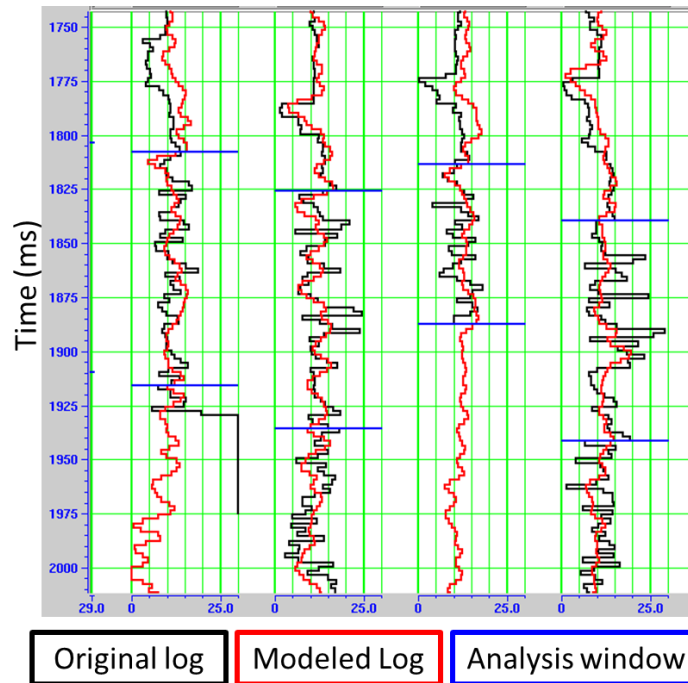


Figure C2. Wells showing the actual and the predicted average porosity.

Figure C3 shows a suboptimun distribution of well log data obtained from cross-plotting the actual and predicted porosity.

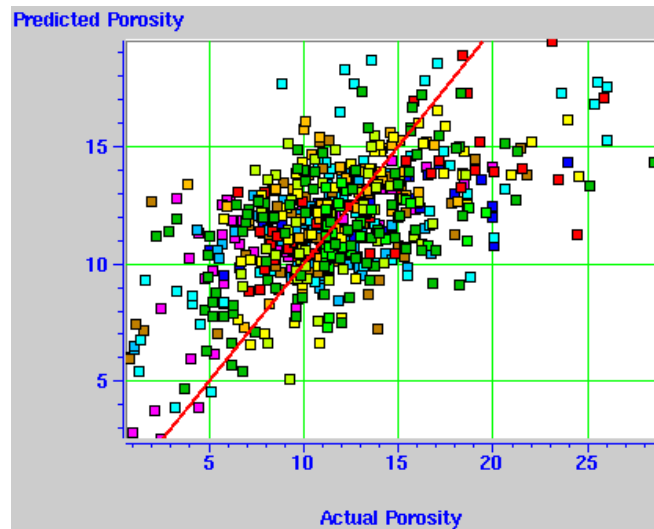


Figure C3. Cross-plot of the predicted and actual porosity. Note that well log data is very disperse. Each color represents a well.

Figure C4 illustrates a seismic cross-section to validate the result of the predicted porosity on two “blind wells” which were not used in the neural network training at any

stage. Note that the low porosity Oswego lime correlates to the predicted porosity using neural networks. In the zone between the Pink Lime and Novi Formation, in which the Red Fork lies on, higher porosity values are obtained. Note in the reference base map that blind well is inside of a channel and the predicted porosity is very high.

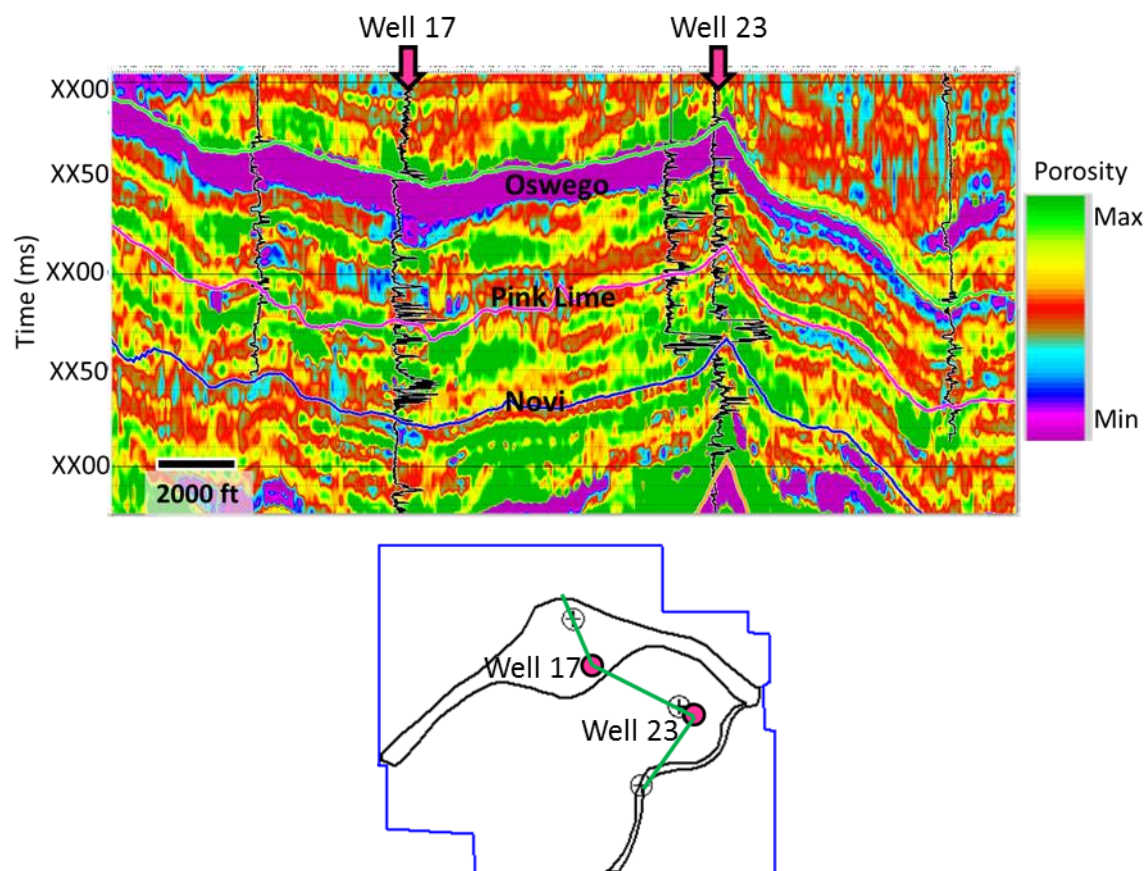


Figure C4. Vertical cross-section on the porosity volume used to validate the results obtained with the neural network.

APPENDIX D: GENERATIVE TOPOGRAPHIC MAPS

Generative topographic maps (GTM) attribute was applied on the megamerged survey in order to compare it with the conventional seismic attributes applied to the same data. GTM is based on the creation of a latent space by adjusting the probabilistic density function to the waveform (Wallet et al., 2009). GTM starts with an initial latent space uniformly populated with clusters which are parametrically defined in a Gaussian distribution.

This method was developed to adress some of the weaknesses of the Self Organizing Maps, and it is based on the Bayesian principles which make it a convergent attribute. Because GTM is a generative model, it can be used for geostatistical analysis in determining facies or structures (Wallet et al., 2009).

GTM applied in this project is plotted in a 2D latent space using a 2D color bar, which is superior than the common 1D latent space GTM solutions.

GTM applied to the megamerged survey does not give any additional information which can help in geological interpretation; rather it delineates similar geological features seen on the conventional attributes. GTM was calibrated for four seismic attributes, which include spectral magnitude, P- and S- impedance and V_p/V_s (Figures D1 and D2).

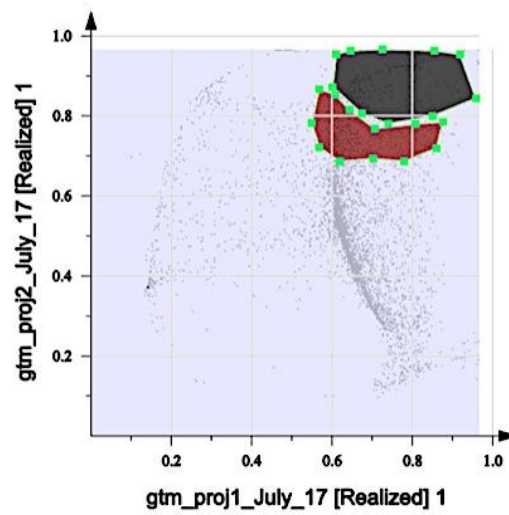
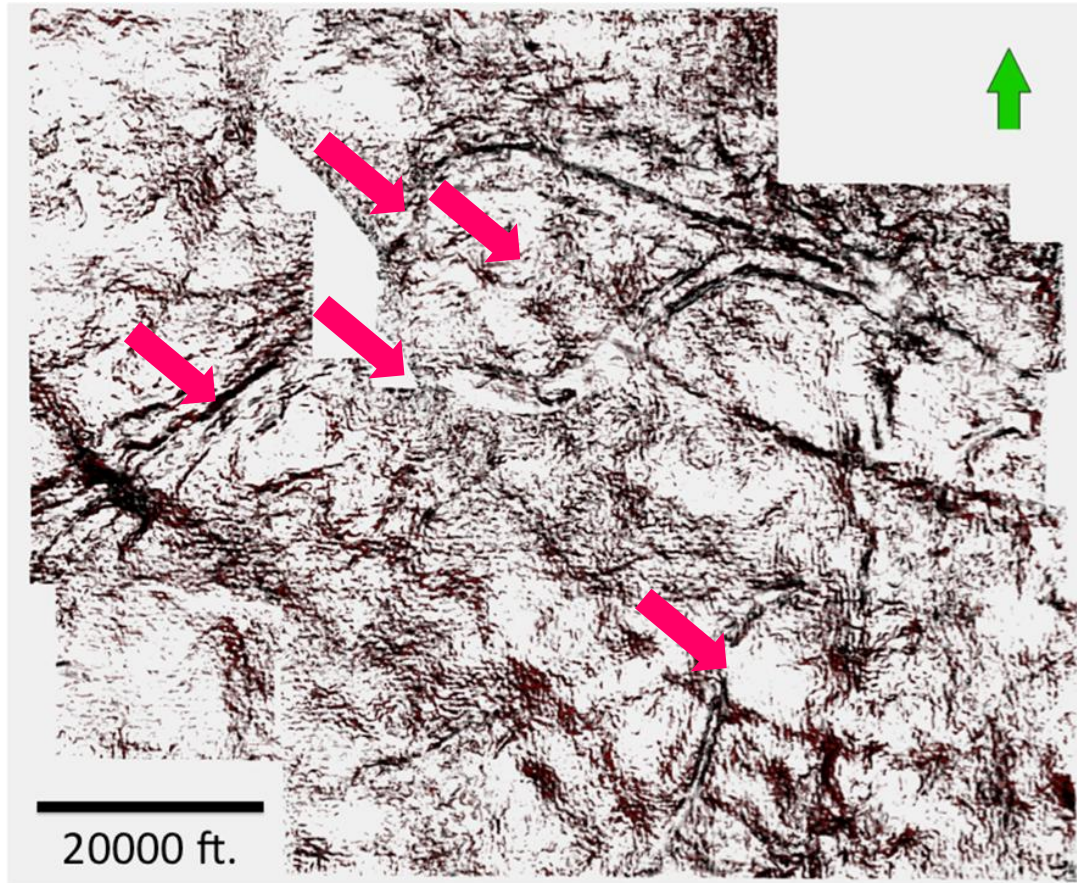


Figure D1. GTM clustering analysis on a 25 ms volume below the Pink Lime surface (top). Density distribution cross-plot on a 2D latent space using just two clusters, which represents structural edges.

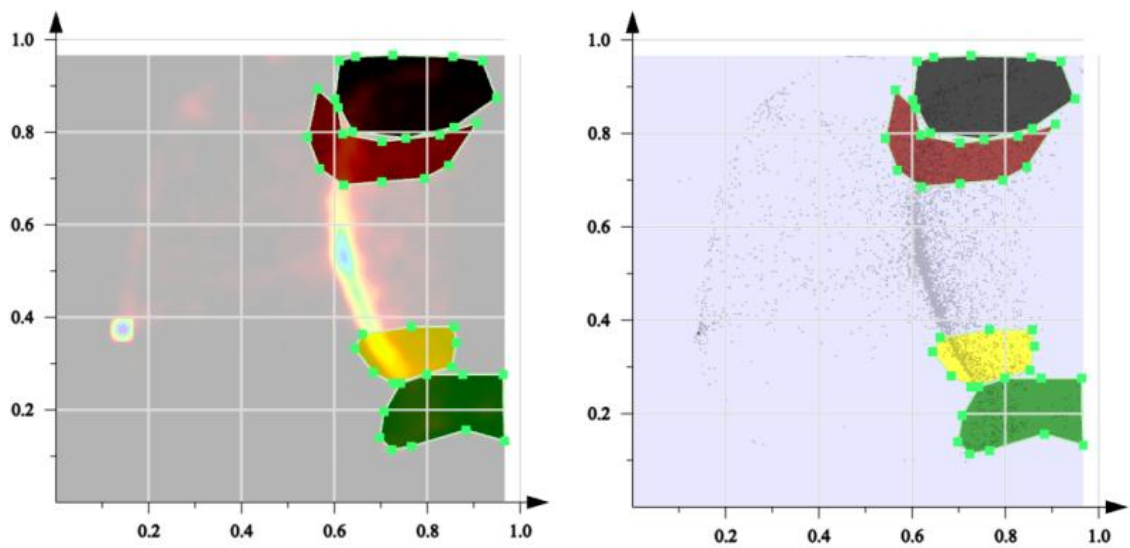
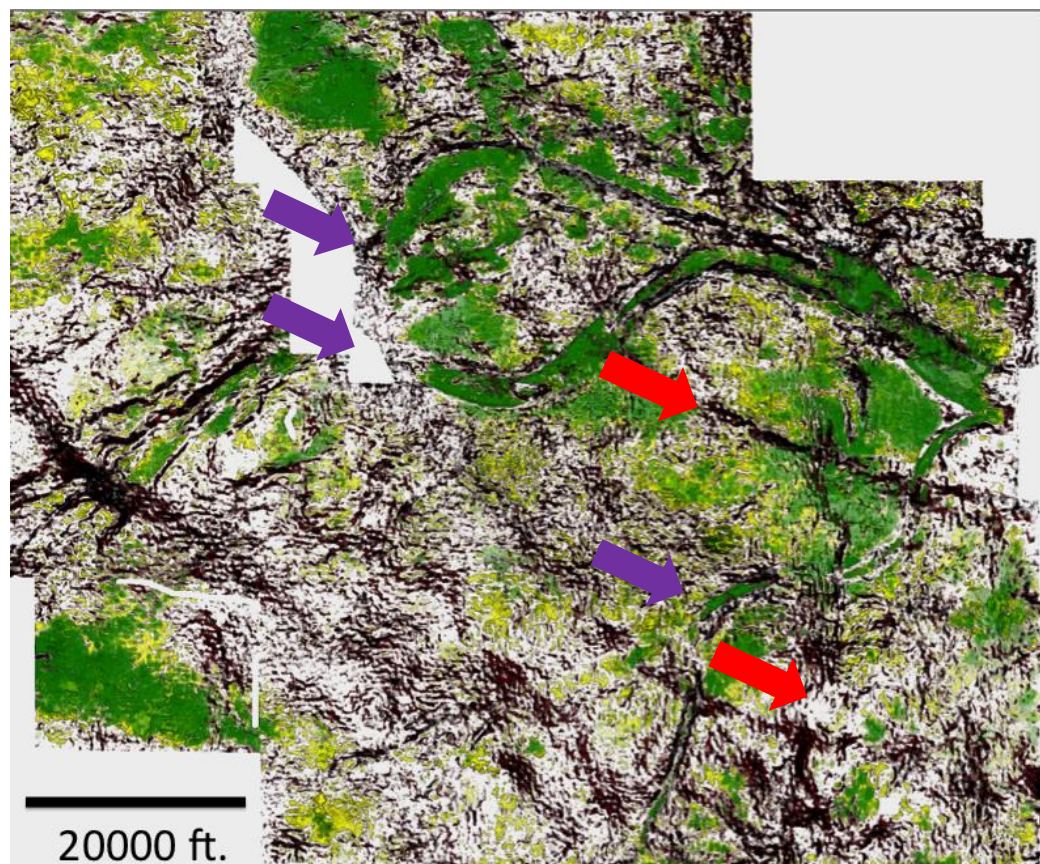


Figure D2. GTM clustering analysis on a 25 ms volume below Pink Lime surface (top). Density distribution cross-plot on a 2D latent space using four clusters, which represents structural features (black and brown) and seismic facies (yellow and green). Purple arrows indicate incised valley fill channels. Red arrows indicate faults.